國立交通大學

機械工程學系

博士論文

非均勻入口流場效應下熔融碳酸鹽燃料電池堆之性能分析

Effects of Inlet Flow Maldistribution in Stack and Transverse Direction on the Performance of a Molten Carbonate Fuel Cell

研究生　：劉旭昉

指導教授：陳俊勳教授

曲新生教授

中華民國九十六年七月

非均勻入口流場效應下熔融碳酸鹽燃料電池堆之性能分析

Effects of Inlet Flow Maldistribution in Stack and Transverse Direction on the Performance of a Molten Carbonate Fuel Cell

研究生： 劉旭昉　　Student: Syu-Fang Liu

指導教授：陳俊勳 曲新生　　Advisor: Chiun-Hsun Chen

Hsin-Sen Chu

國 立 交 通 大 學

機械工程學系

博 士 論 文

A dissertation

Submitted to Department of Mechanical Engineering

College of Engineering

National Chiao Tung University

in Partial Fulfillment of the Requirements

for the Degree of

DOCTOR OF PHILOSOPHY

in

Mechanical Engineering

July 2007

Hsinchu, Taiwan, Republic of China

中華民國九十六年七月

國立交通大學

論文口試委員會審定書

本校 機械工程 學系博士班 劉旭昉 君

所提論文(中文) 不均勻入口流場效應下熔融碳酸鹽燃料電池堆之性能分析

(英文) Effects of Inlet Flow Maldistribution in Stack and Transverse Direction on the Performance of a Molten Carbonate Fuel Cell

合於博士資格水準、業經本委員會評審認可。

口試委員：陳朝光　　洪哲文

顏維謀　　陳俊勳

楊文美　　曲新生

指導教授：陳俊勳　　曲新生

系主任：　　教授

中華民國 九十六 年 七 月 九 日

非均勻入口流場效應下熔融碳酸鹽燃料電池堆之性能分析

研究生：劉旭昉　　指導教授：陳俊勳 曲新生

摘　要

本論文主要在探討，陽極及陰極氣體入口處使用非均勻莫耳流率(mole flow rate)時，對單體熔融碳酸鹽電池(Molten Carbonate Fuel Cell)及電池堆 (Molten Carbonate Fuel Cell Stack)的性能影響。以有限差分法(finite difference method)對質量守恆、能量守恆及化學計量守恆式等偏微分方程式進行解析。並對部份的結果用套裝軟體 FlexPDE 以有限元素法(finite element method)進行驗證。在分析的方法中，本文利用莫耳流率的不均勻性設計成八種不同型式(patterns)的入口流場，然後分析入口流場對單體熔融碳酸鹽電池及電池堆性能的影響。

首先，分析非均勻入口流場對單體熔融碳酸鹽電池性能的影響。在溫度場及電流密度場方面，以有限差分法進行求解，再利用套裝軟體 FlexPDE 加以驗證，兩者之間的數據相當吻合。對於單體的融碳酸鹽電池而言，當氣體入口處的非均勻莫耳流率偏差量為 0.25 時(d=0.25)，在 G 式樣的電池溫度比均勻流(d=0)的高出 12%，而在 D 式樣的電流密度場要比均勻型式樣的高出 37%，根據結果，在入口處之非均勻流會對電池的溫度及電池密度分佈範圍產生明顯的影響。

此外，本研究第二部份探討具交叉流氣體供應方式的熔融碳酸鹽

燃料電池在高氣體使用率與非均勻陽極氣流下的性能表現。數學模式方面採用二維之質量，能量等守恆方程式，而不考慮堆疊方向的性質變化。由數值計算結果顯示陽極氣體使用率隨入口莫耳流率之減少而增加。此外，陽極端入口的非均勻流將導致在陽極出口端及陰極入口端產生不反應區域，進而影響到電池的局部電流密度與性能。

最後，本文第三部份則進一步探討非均勻入口流場對電池堆性能的影響。電池堆使用 10 個單體熔融碳酸鹽電池所組成，在陽極及陰極入口處之流場皆為不均勻流場。本文主要是利用近似三維之數值模擬，來分析一個具有 10 層單體的熔融碳酸塩燃料電池堆之溫度場及電壓分佈。在陽極及陰極入口處，假設莫耳流率分佈曲線沿電池堆方向為漸增式及均勻式設計，並將其組成四組不同的入口流場形式(patterns)。結果顯示在陰極入口處使用非均勻的莫耳流率會明顯的改變熔融碳酸塩燃料電池堆的溫度場，而且電池堆的入口有最少的莫耳流率時，那麼在此時的陰極出口處會產生最高的溫度。此外，在沿著電池堆的陽極入口處，如果具有非均勻的莫耳流率時，會強烈影響電壓的分佈。沿著電池堆的方向來看，各單體電池的平均溫度變化率約為百分之二，而平均的電池電壓變化率約為百分之四十。此結果與作者先前所探討的非均勻流對單體電池的變化率要有比較明顯的不同。

Effects of Inlet Flow Maldistribution in Stack and Transverse Direction on the Performance of a Molten Carbonate Fuel Cell

Student: Syu-Fang Liu **Advisor: Chiun-Hsun Chen**
Hsin-Sen Chu

Abstract

This study investigates the temperature and current density distributions in a molten carbonate fuel cell unit and stack when the inlet flows of the anode gas and the cathode gas are mal-distributed. Furthermore, this study extends the research to the temperature and current density distributions in a molten carbonate fuel cell when there is higher utilization of anode gas. In the analysis of a unit cell, the two-dimensional simultaneous partial differential equations of mass, energy and electrochemistry are solved numerically. The numerical method is reliable through the accuracy comparison between this FORTRAN program and a software package. The results indicate that the maldistribution of anode and cathode gases dominates the current density field and the cell temperature field, respectively. Moreover, the non-uniform inlet flow slightly affects the mean temperature and mean current density, but worsens the distribution of temperature and current density for most maldistribution patterns. According to the results, the variations of the cell temperature in Pattern G and the current density in Pattern D are 12% and 37% greater than those in the uniform pattern when the deviation of the non-uniform profile is 0.25. Consequently, the effect of non-uniform inlet flow in the transverse direction on the temperature and current density distribution on the cell plane is evident, and cannot be neglected. In the analysis of a MCFC stack, this study considers that the MCFC is composed by ten stacks, and the molar flow rate in each

stack is different because of the inlet distributor. This study employs the procedure of calculation in a MCFC unit to calculate the results of each stack, and then averages the temperatures of up separator and down separator, which connect together between stacks. The FORTRAN program iterates the whole procedure to get the quasi three-dimensional temperature and current density distributions until the relative errors of average temperature of separators satisfy the converge criterion. The primary results show that the effect of non-uniform in the stacking direction is more apparent than that of non-uniform in the transverse direction on the thermal and electrical performance of a MCFC.

Then, the second part of this dissertation, the electric performance of a planar MCFC unit with cross-flow configuration when there is higher gas utilization in anode and cathode is investigated in the final part of this dissertation. A two-dimensional model, considering the conservation equations of mass, energy and electro-chemistry is applied. The results show that the anode gas utilization increases with a decrease in the molar flow rate, and the average current density decreases when the molar flow rate drops. In addition, non-uniform inlet profile of the anode gas will induce a happening of non-reaction area in the corner of the anode gas exit and the cathode gas inlet. This non-reaction area deteriorates the average current density and then reduces the electrical performance up to 4% when the anode gas molar flow rate is 0.01242 mol/s and anode gas utilization is 73%.

Finally, in the third part of this dissertation, the effects of the non-uniform inlet flow on the MCFC stack are investigated. We develop a quasi-three dimensional numerical method for analyzing three-dimensional temperature and cell voltage distribution in a ten-layer molten carbonate fuel cell. The authors consider the non-uniform profile as progressively increasing along the stacking direction, and

assign it to the anode gas inlet or cathode gas inlet to form four kinds of patterns. Results indicate that the non-uniform molar flow rate of cathode gas obviously changes the temperature field of a molten carbonate fuel cell stack, and highest cell temperature occurs at the cathode gas exit in the layer with the lowest molar flow rate. Moreover, non-uniform anode gas in the stacking direction strongly affects cell voltage distribution in the molten carbonate fuel cell stack. The variation of average cell temperature and cell voltage among different layers along the stacking direction are 2% and 40%, apparently larger than the variation rate due to non-uniformity in the transverse direction in previous chapter.

誌　謝

首先誠摯的感謝指導教授曲新生博士，老師悉心的教導使我得以一窺融熔碳酸鹽燃料電池領域的深奧，不時的討論並指點我正確的方向，使我在這些年中獲益匪淺。老師對學問的嚴謹更是我輩學習的典範。同時亦得感謝成功大學機械系的陳朝光教授、清華大學動機系洪哲文教授、華梵大學機電系顏維謀教授，以及本校盧定昶教授、陳俊勳教授和楊文美教授對我研究上的建議與指正，使得本論文能夠更完整而嚴謹。

特別感謝同僚袁平博士及王士賓博士在這段期間，於學理上的協助和討論及工作上的支援，在此致上最誠摯的謝意。

在漫長的學習過程中，實驗室裡共同的生活點滴，學術上的討論、言不及義的閒扯、讓人又愛又怕的宵夜、趕作業的革命情感，感謝學長、同學、學弟妹的共同砥礪，你們的陪伴讓研究生活變得絢麗多彩。感謝實驗室的森溥學長，同窗致廣，學弟志文、世國、木勝、時明、家輝、章裕、謙成、銘恩、清益、榮祥、式堯及祥哲、學妹淑惠，你們的幫忙讓我銘感在心。

感謝父、母親的養育之恩與妹妹及兩個弟弟的關心及鼓勵，使我無後顧之憂地順利完成學業。

妻子明妃在背後的默默支持更是我前進的動力，沒有明妃的體諒、包容，相信是無法順利完成這篇論文。

最後，謹以此文獻給我摯愛的雙親及愛妻明妃。

Table of Contents

List of Tables

List of Figures

Nomenclature

a	area of heat transfer area per base area ($m^2 \cdot m^{-2}$)
c_p	specific heat capacity ($J \cdot mol^{-1} \cdot K^{-1}$)
d	deviation of inlet flow profile, as shown in Fig. 2
E	Nernst voltage (V)
E_0	reversible open circuit voltage (V)
F	Faraday's constant (96485 As mol^{-1})
h	heat transfer coefficient ($W \cdot m^{-2} \cdot K^{-1}$)
i	current density ($A \cdot m^{-2}$)
i_0	exchange current density ($A \cdot m^{-2}$)
$\bar{i}$	average current density in the x-y plane ($A \cdot m^{-2}$)
Δi	current density variation in the x-y plane ($A \cdot m^{-2}$)
k	conductivity ($W \cdot m^{-1} \cdot K^{-1}$)
L	length in the x or y direction, indicated by subscript x or y (m)
n	molar flow rate of anode gas or cathode gas per unit width, indicated by subscript ag or cg ($mol \cdot m^{-1} \cdot s^{-1}$)
N	molar flow rate of anode gas or cathode gas, indicated by a subscript ag or cg ($mol \cdot s^{-1}$)
n_e	number of electrons transferred in reactions of anode and cathode
P	pressure (Pa)
q	heat generation due to chemical reaction ($W \cdot m^2$)
R	universal gas constant (8.314 $J \cdot mol^{-1} \cdot K^{-1}$)
R_{tot}	total cell resistance ($\Omega \cdot m^2$)

T	temperature (K)
$\overline{T}$	average temperature in the x-y plane (K)
ΔT	temperature variation in the x-y plane (K)
V	cell voltage (V)
x	x direction
X	molar fraction indicated by subscript k
y	y direction

Greek symbols

δ	thickness (m)
ν	stoichiometric coefficient of k-component indicated by subscript k

Subscripts

ag	anode gas
ag-c	interface between anode gas and cell
ag-s	interface between anode gas and separator
c	cell
c-s	interface between cell and separator
cg	cathode gas
cg-c	interface between cathode gas and cell
cg-s	interface between cathode gas and separator
k	components in anode gas or cathode gas
s	separator
x	x direction
y	y direction

1. Introduction

1.1. Background & Motivation

A fuel cell is an electrochemical device for transforming chemical energy into electricity directly. Fuel cells are different from traditional thermal engines which transform chemical energy to mechanical energy via combustion, and then to electricity by power generators. As a result, fuel cells have higher transfer efficiency than thermal engines because they are not restricted by Carnot cycle efficiency. The maximal theoretical thermodynamic efficiency, ε_{th}, of a fuel cell is the ratio of Gibb's free energy to the standard enthalpy of formation:

$$\varepsilon_{th} = \frac{\Delta G}{\Delta H} \tag{1.1}$$

The theoretical efficiency of fuel cells is about 80%, but in practice, it is determined by the cell voltage, V_{cell}:

$$\varepsilon_{real} = \frac{-zFV_{cell}}{\Delta H} \tag{1.2}$$

The practical electrical efficiencies of fuel cells are about 40-60%, depending on the type of fuel cell. Losses that limit cell voltage include ohmic losses, kinetic loss, and mass transfer limitations in the system. Increasing energy demands and global environment preservation concerns have increased the necessity of developing energy systems with high energy conversion efficiency and very low environmental pollution.

1.2. Types of Fuel Cells

Researchers have focused their attention on four kinds of fuel cells that have potential application in various industries. These fuel cells include the proton exchange membrane fuel cell (PEMFC), phosphoric acid fuel cell (PAFC), molten carbonate fuel cell (MCFC), and solid oxide fuel cell (SOFC), which are classified by electrolytes, operation temperature, etc. Table 1-1 lists these fuel cells.

1.3. Brief Overview of MCFC

In the 1930s, Emil Baur and H. Preis experimented with high-temperature, solid oxide electrolytes in Switzerland. They encountered problems with electrical conductivity and unwanted chemical reactions between the electrolytes and various gases (including carbon monoxide). The following decade, O. K. Davtyan of Russia explored this area further, but met with little success. By the late 1950s, Dutch scientists G. H. J. Broers and J. A. A. Ketelaar began building on this previous work. They determined that limitations on solid oxides at that time made short-term progress unlikely. Instead, they focused on electrolytes of fused (molten) carbonate salts. By 1960, they reported making a fuel cell that ran for six months using an electrolyte "mixture of lithium-, sodium- and/or potassium carbonate, impregnated in a porous sintered disk of magnesium oxide." However, they found that the molten electrolyte was slowly lost, partly through reactions with gasket materials. At approximately the same time, Francis T. Bacon was developing a molten cell using two-layer electrodes

on either side of a "free molten" electrolyte. At least two groups were working with semisolid or "paste" electrolytes and most MCFC research groups were investigating "diffusion" electrodes rather than solid electrodes. In the mid-1960s, the U.S. Army's Mobility Equipment Research and Development Center (MERDC) at Fort Belvoir tested several molten carbonate cells made by Texas Instruments. These cells ranged in size from 100 watts to 1,000 watts output and were designed to run on "combat gasoline" using an external reformer to extract hydrogen. In particular, the Army wanted to use fuels already available rather than a special fuel that might be difficult to supply to field units.

Molten Carbonate fuel cells (MCFCs) contain a liquid solution of lithium, sodium and/or potassium carbonates, soaked in a matrix for an electrolyte. They promise high fuel-to-electricity efficiencies, about 60% normally or 85% with cogeneration, and operate at approximately 1,200 ℉（650 ℃). This high operating temperature is necessary to achieve sufficient electrolyte conductivity. Because of this high temperature, noble metal catalysts are not required for the fuel cell's electrochemical oxidation and reduction processes. To date, MCFCs have been operated with hydrogen, carbon monoxide, natural gas, propane, landfill gas, marine diesel, and simulated coal gasification products. MCFCs from 10 kW to 2 MW have been tested on a variety of fuels, and are primarily targeted toward electric utility applications. Carbonate fuel cells for stationary applications have been successfully

demonstrated in Japan and Italy. Their high operating temperatures create a big advantage because this allows higher efficiency and the flexibility to use more types of fuels and inexpensive catalysts. This is because reactions involving the breaking of carbon bonds in larger hydrocarbon fuels occur much faster at higher temperatures. A disadvantage to these phenomena, however, is that high temperatures enhance the corrosion and breakdown of cell components. The higher working temperature of these fuel cells, between 650~1000℃, and the heat transfer caused by conduction and convection, generates radiation heat transfer. The mechanism in this case is electromagnetic radiation propagated because of temperature difference, called thermal radiation.[1]

Davtyan was the first to realize the necessity of “support” for the electrolyte, i.e. a matrix which holds the electrolyte in place and prevents direct combination of reacting gases. In 1964, Broers reported on $LiAlO_2$, which was chemically stable and gave much performance. Broers was also the first to introduce porous nickel as the anode material. Clauss and Genin showed that porous nickel oxide, oxidized *in situ*, provides stable performance for the cathode. An MCFC uses a salt mixture of alkali carbonates as the electrolyte. This mixture provides mass and charge transfer from the cathode to the anode via carbonate ions. The electrolyte in modern applications is a mixture of lithium carbonate and potassium carbonate. Mixtures of lithium carbonate and sodium carbonate and carbonates of alkaline-earth metals are also in use. The typical operating temperature of a MCFC is about 650°C. At that high operating

temperature, the carbonate mixture is in a molten state and becomes a good ionic conductor. The molten electrolyte is contained in a porous electrolyte matrix of $LiAlO_2$, which is an electrically insulating and chemically inert ceramic. Thus, royal metals are not required to act as catalysts, reducing the material cost of the MCFC. A molten carbonate fuel cell has many features as follows.

1. The electrolyte material is a eutectic mixture of lithium carbonate and potassium carbonate. It is in liquid phase at temperatures higher than 500° C.

2. An MCFC exhibits an internal reforming ability because of its high operating temperature. Therefore, it does not require pure hydrogen as fuel, but can use hydrocarbons such as natural gas and coal gas etc., Moreover, a MCFC produces 40% lower carbon dioxide emission than a thermal power plant.

3. The waste heat of reacting gases emitted by the MCFC can be utilized to generate electric power through gas turbines.

4. An MCFC can be used as a device for separating and concentrating carbon dioxide because the anode gas has the ability to concentrate carbon dioxide[2]

There are several important issues for molten carbonate fuel cell are:[3]

(1). Cell Sealing

In addition to the cathode, anode, and electrolyte, each cell structure also contains an electrolyte matrix that holds the liquid electrolyte in place. This matrix structure is composed of a mixture of ceramic powder (usually lithium aluminates, $LiAlO_2$) and carbonate electrolyte. The mixture is semisolid (paste-like) and the molten carbonate electrolyte is immobilized by the capillary force. The resulting matrix structure is stiff and impermeable to the reactant gases, but also deformable. The plasticity of the matrix provides a gastight seal around the periphery of the cell. Gas sealing is a major challenge in high-temperature fuel cells. This edge sealing technique is often called a wet seal. The wet seal concept is very similar to the sealing technique used in PEM fuel cells in that both techniques use the electrolyte itself as the sealing material to provide gas-tight sealing. This works because the electrolyte itself is gas impermeable, and is compatible with the rest of the cell components. In the molten carbonate fuel cell, however, wet sealing the cell is the only feasible sealing technique when the cell housing is made of metals. This is because the carbonate electrolyte is very corrosive and very few materials can remain stable under MCFC operating conditions. Although high-density alumina and other dense ceramics are suitable sealing materials, they cannot withstand thermal cycling.

(2). Current Collectors

Current collectors enhance the rate of electric current collection and reduce ohmic losses. They are usually made of stainless steel or nickel metal screens and are located between the electrodes and the cell housing for good electrical contact between both components. The cell housing is made of metal shells with flow distribution channels built on its inside surface for proper distribution of the gas supply to the respective electrode.

(3). Electrolyte Management

Another unique feature of the molten carbonate fuel cell structure is its unique method of electrolyte management. PAFC and PEMFC electrolyte management uses hydrophobic materials such as PTFE. The dispersed PTFE in the porous electrodes acts as a binder for the integrity of the electrode structure and as a wet-proofing agent for the establishment of a stable gas-liquid interface. However, this method cannot be used for MCFCs because similar de-wetting materials do not exist in molten carbonate under oxidizing conditions. Hence, capillary equilibrium is used to control electrolyte distribution in the porous electrodes, and stable electrolyte/gas interfaces in MCFC porous electrodes (the so-called three-phase zone).

An MCFC power plant is one of the most attractive new types of power plants

available, and has the potential to replace conventional thermal power plants. The principal reason for this is that MCFC power plants have a higher energy conversion efficiency and are able to use both LNG and coal gas as fuel. Furthermore, an MCFC power plant can be applied in the electric power industry as a dispersed power source or a central power source fueled by LNG or coal. Many manufacturers and organizations have developed conceptual designs of MCFC power plants. The efficiency in most of these designs is 45%~70% (LHV, low heat value). MCFC power plants therefore carry great promise as primary power plants in the future, especially for a decentralized power supply.

Research and development on MCFCs is conducted primarily in the USA, Japan, and Europe. The USA led MCFC technology initially, but Japan and several European countries, which started their own R&D programs in the 1980s, have greatly increased their activities. The goal of the development programs in all of these countries is to develop and commercialize simple, low-cost power plants that can compete favorably with conventional thermal power plants. Many R&D programs have now reached the commercial stage, where prototype stacks and plants are being constructed and tested.

The principle of an MCFC is that, at high operating temperatures, carbonate ions migrates in a molten electrolyte. This carbonate ion produced from carbon dioxide and oxygen in the cathode passes through the electrolyte, and reacts with the hydrogen in anode. At the same time, this reaction in the anode produces carbon

dioxide, vapor, and electrons. The electrons are conducted to the external load circuit through the anode electrode, and back to the cathode through the cathode electrode. Figure 1.1 shows the principle of electric power generation in an MCFC, and Fig. 1.2 shows the basic components of a fuel cell. The key materials in an MCFC are anode electrode, cathode electrode, electrolyte, and bipolar plate. The chemical reaction equations in the anode and cathode of an MCFC are as follows.

In the cathode,

$$\frac{1}{2}O_2 + CO_2 + 2e^- \rightarrow CO_3^{-2} \tag{1.3}$$

In the anode,

$$H_2 + CO_3^{-2} \rightarrow CO_2 + H_2O + 2e^- \tag{1.4}$$

The total reaction is

$$\frac{1}{2}O_2 + H_2 + CO_2 \rightarrow CO_2 + H_2O \tag{1.5}$$

In equation (1.1) and (1.2), the carbon dioxide is the product and reactant in both the anode and the cathode. The overall reaction in MCFCs is similar to other fuel cells, but CO_2 is produced at the anode and consumed at the cathode. This implies that a CO_2 recycling system is needed to supply CO_2 from the anode chamber to the cathode chamber in a power plant. When carbon dioxide produced in the anode is transferred to the cathode as the reactant, it creates a closed cycle and reduces overall carbon dioxide emissions.

Because of their many advantages such as low pollution, low noise, high efficiency, wide application, etc., MCFCs can assist or even replace thermal electric generators in the future. Therefore, this study investigates the thermal and electrical performance of a MCFC based on its potential development in electric power generation [4, 5].

1.4. Literature Survey

The technology of the molten carbonate fuel cell (MCFC) has received much attention in the last two decades, and is now at the stage of being scaled-up for commercialization. Since the MCFC operates at a high temperature of around 650℃, the prediction of the temperature distribution is important to avoid hot spots in cells. Hot spots of extra high temperature cause electrolytic loss by corrosion and reduce the lifetime of the fuel cells. Moreover, the variation of the temperature influences the local current density, and changes the electrical performance of the MCFC. Therefore, many researchers have investigated the thermal and electrical performance of molten carbonated fuel cells.

In the analysis of an MCFC, the major researches focus on the temperature and current density field in a unit, a stack, or transient state. For a MCFC unit analysis, Wilemski and Wolf [6] used a numerical method to analyze a two-dimensional heat and mass transfer in a large MCFC unit with considering different cell operating conditions and design parameters. Kobayashi et al. [7] used a numerical method to

solve the steady-state temperature distribution of fuel cells with reaction areas of $900\,cm^2$ and 3600 cm^2. They compared experimental data with numerical results, and reasonable agreement between them was reached. Lee et al. [8] calculated the temperature distribution, hydrogen conversion, and current density distribution of a unit molten carbonate fuel cell using constant voltage and constant current density methods. The results indicated that cell performance calculated by the constant voltage method fits better the experimental data than that calculated by the constant current density method.

The analysis on the thermal and electrical performance of a MCFC stack recently grows up, because a MCFC stack had applied in industry. Yoshiba et al. [9] developed a three-dimensional numerical model to analysis the cell voltage, temperature, and current profile in molten carbonate fuel cell stacks. They compared the effects of flow patterns such as co-flow, counter-flow, and cross-flow, and found that the net output power was highest in co-flow geometry. Later, Yoshiba et al. [10] investigated the temperature and performance of molten carbonate fuel cell stacks with co-flow configuration by applying a numerical model. Their results indicated that the increase in the partial internal resistance and an insufficiency of supplied fuel gas to the cell could induce differences in cell voltage. He and Chen [11] investigated the three-dimensional temperature distribution, the pressure, the gas concentration, and the current density of a molten carbonate fuel cell of five stacks with three manifolds, using CFD software. The results showed that the maximum temperature

locates at different positions under co-flow, counter-flow, and cross-flow configurations. The maximum temperature difference among the flow configurations is 10-20℃. Recently, Ma et al. [12] developed a practical computational model for a MCFC stack. This model included three dimensional fluid flow, heat and mass transfer, gas-phase and surface chemistry, electrochemistry and structural mechanics, and this model was validated by comparing experimental data. Moreover, the materials and design of an MCFC stack are reviewed by Mugikura et al [13].

In the transient analysis of a MCFC, Lukas et al [14] developed a nonlinear mathematical model of an internal reforming MCFC stack for control system applications. This model can be used to provide realistic evaluations of the responses to varying load demands on the fuel cell stack and to define transient limitations and control requirements. Koh et al. [15] used a software package to predict the dynamic pressure and temperature distribution of gas in a co-flow molten carbonate fuel cell stack based on an assumption of uniform current density. The results indicated that the predicted axial velocity profile precisely reflects the mass change in MCFC, by showing a drop in the volumetric flow in the cathode and an increase in the anode. Later, Koh et al. [16] used computational fluid dynamics code to predict the temperature distribution of a co-flow MCFC stack considering the effects of radiation and variable gas properties. The results showed that the thermal radiation only weakly affects the calculation of the temperature field using the model,

and most of the gas properties can be treated constant, except for the specific heat capacity of the anode gas. He and Chen [17] extended their simulation to investigate the transient behavior of an MCFC stack with the cross-flow configuration; the results showed that the current density profile changes rapidly in the beginning and slowly in the following stage, and the temperature response is slow when the MCFC was under a step voltage change. Xu et al [18] developed a voltage drop and recovery analysis method to estimate the different contributions to the transient behavior of a MCFC. Their results showed that the model predictions were in reasonable agreement with the experiment data, and it is an efficient tool to analyze the transient characteristics of a MCFC. Heidebrecht and Sundmacher [19] used a general notation in dimensionless form to analyze the transient state of a single counter-flow MCFC with considering the concentration, temperature, and potential field of the gas and the solid phases. This general notation of calculation can easily be extended to describe cross-flow 2D unit and 3D stacks. Lee et al. [20] used a numerical method to analyze the beginning of the operation of a MCFC unit, and investigated the effects of the molar flow rates of gases and the utilization of fuel gas. Their results showed that the time required to approach a steady-state decreases with an increase in the inlet gas-flow rates or the hydrogen utilization.

The electrodes and electrolyte phenomena are important to the overall performance in a MCFC unit or stack, so there are many literatures investigating the analysis on the anode, cathode, and electrolyte. Vallet and Braunstein [21] modified

steady-state equations for composition gradients in battery analogs with binary mixtures of molten salts as electrolytes to apply to a MCFC, and used a numerical method to solve the diffusion-migration equation to predict the development with time of the concentration gradient. Wilemski [22] used individual porous electrode models for calculating the local cell overpotential and current density in a MCFC, and their results had compared with experiment data. Kunz et al [23] developed a cathode model of a MCFC, which was a function of cathode electrolyte content including the effective agglomerate diameter, porosity, tortuosity, and number based on knowledge of the electrode's pore spectrum. Lee et al. [24] presented the experimental characterization of a MCFC unit with transient response analysis methods such as electrochemical impedance spectroscopy and current interrupt method. They found that the cathode over-potential was controlled by mixed diffusion of oxygen and carbon dioxide. Prins-Jansen et al [25, 26] considered the cathode was constructed by an easiest-to-handle shape of semi-infinite slabs, and used the agglomerate model for porous electrodes in MCFC. Using analytical mathematical tools, this model can give the optimal electrode thickness and agglomerate size based on general problem properties and analytic solutions for special cases. Fehribach et al [27] derived an electrochemical-potential model for the peroxide mechanism describing the electrochemistry of a MCFC cathode. This model made clear the connection to the underlying reaction stoichiometry, and requiring the fewest equations consistent with that stoichiometry. Their results

showed that the mean current density associated with a small portion of electrode may be increased by as much as a factor of five, and on this scale the current density is most sensitive to the electrolyte diffusivity. Bergman et al [4] investigated two cathode materials to elucidate the impact of the cathode material on the formed corrosion layer by polarization measurements and electrochemical impedance spectroscopy. The results indicated that the contact resistance between the cathode and the current collector contributed with a large value to the total cathode polarization. Morita et al [28] estimated the potential of Li/Na carbonate as the MCFC electrolyte by investigating the dependence of the cell performance on the operating conditions and the behavior during long-term performance in several bench-scale cell operations. Arato et al. [29] investigated the limitation on the performance of molten carbonate fuel cells due to gas diffusion phenomena in the porous electrodes when high reactant utilization factors were used. The expression of voltage decay depends on concentration polarization due to hydrogen and carbon dioxide, while oxygen diffusion effects have been considered to be negligible. Furthermore, the limiting diffusion conditions must also be correctly evaluated for the local temperature and pressure drops. For over-potential from the anode gas to the cathode gas, Bosio et al. [30] presented a model and experimental investigation of electrochemical reactors in the molten carbonate fuel cell. Additionally, they used their formula for total cell resistance, tested with experimental data, to analyze the temperature distribution and current density distribution for a single cell and stacks,

using FORTRAN program. Their numerical results agree with the experimental results, and showed that the thermodynamics fails to predict the open circuit voltage because of the effects of gas crossover phenomena at the cell level. Although thermodynamic equilibrium should be established under open circuit conditions in principle, short circuit electrical currents circulate within the cell, and the consequent voltage loss is responsible for irreversibility.

For a power plant, there are also many researches analyze its overall efficient by using a simple or rapid calculation for a MCFC. Mangold and Sheng [31] applied a reduced nonlinear model to solve a planar molten carbonate fuel cell with cross-flow. Since the reduced model was of the lower order than the original model, it markedly reduced the computational time. Therefore, this model was suitable for application in predicting the behavior of a control system in a power plant. He [32] presented a simulation model for investigating the dynamic performance of MCFC power-generation systems. This simulation model consists of nine types of component models, which are fuel cell, external reformer, steam generator, water separator, rotation equipment, heat exchanger, DC/AC invertor, pipeline and control valve. Later, He [33] extended his analysis to a MCFC power generation system including twelve types of component models. De Simon et al [34] simulated a global MCFC power plant in steady state. This simulation can conduct a sensitivity analysis with the preliminary input specification, and find the process parameters whose change improves the global efficiency. Yoshiba et al [35] calculated the

materials and heat balance of integrated coal gasification and MCFC combined system with considering the electricity generating performance of the practical cell. The results showed that the net thermal efficiency of the anode gas recycling system has a peak for carbon dioxide partial pressure where the net thermal efficiency of the anode heat exchange system increases as the carbon dioxide partial pressure of the cathode gas decreases. Recently, Baranak et al [36] developed a MCFC model for a unit analysis with considering several performance model equations separately for anode and cathode, and then they applied this model into a process simulation software to simulate a power system.

In a MCFC, there are simultaneous reactions in anode side, which are chemical reaction in anode, reforming reaction, and water-gas shift reaction. Most MCFC use internal reformer because of its simplicity in structure. Park et al [37] investigated the effects of the reformer in an internal-reforming MCFC on the temperature distributions, conversion of methane, and compositions of gases by a numerical method. Their results indicated that the methane-reforming reaction and the water-gas shift reaction occur simultaneously and the conversion of methane to hydrogen reached 99%, and the endothermic-reforming reaction contributes to a uniform temperature distribution. Seo et al [38] analyzed the performance and operation results of an external-reformer that supplied synthesis gases to a 100kW class MCFC. In order to maintain the outlet temperature of the reforming reactor over $580\,^{\circ}C$, it is necessary to heat the reformed gases at the convection zone of

combustion gases. Kim et al [39] discussed the effects of water-gas shift reaction on the temperature distribution, voltage distribution, conversion, and performance in a MCFC unit. Their results indicated that the voltage calculated without the shift reaction would be higher than the real value, and the effect of the shift reaction on the voltage distribution and cell performance is quite small.

Bosio et al [40] reported the development of molten carbonate fuel cell technology at Ansaldo Ricerche, from small-scale single cell up to stacks of several KW capacities, for industrial applications. Although the report showed that MCFC technology had been successfully tested on stacks in the kW power class, the control of the start-up phase, electrolyte migration through the manifolds and gas feed distribution have not yet been to be solved. Notably, the gas feed distribution in [40] identified the variation of mole flow rate in different stacks. Hence, the stack nearest the anode gas inlet duct has largest flow rate and the farthest one has the lowest. The cross-sectional geometry of a fuel cell is similar to that of a heat exchanger, whose inlet distributor is responsible for a non-uniform flow distribution in the frontal area. Therefore, the maldistribution of the inlet flow rate on the frontal area is realistic and it must affect the performance of fuel cells. In the research of a heat exchanger, Chiou [41] first investigated the thermal performance deterioration in a cross-flow heat exchanger due to the flow non-uniformity. Later, Yuan [42, 43] analyzed the thermal performance and exergy of a three-fluid cross-flow heat exchanger with considering a non-uniform inlet flow. The results showed that most non-uniform

will drop the performance of a heat exchanger, but some of the non-uniform profiles in a three-fluid cross-flow heat exchanger may promote the performance.

Hirata and Hori [44] adopted a numerical method to examine the relationships among the gas flow uniformities in the planar direction, the gas flow uniformity in the stacking direction, and the cell performance in a co-flow MCFC. Their results showed that the gas flow uniformity in the stacking direction is about two to ten times that in the planar direction. Later, Hirata et al [45] investigated the relationship between the gas channel height, the gas flow characteristics, and the gas diffusion characteristics in a plate heat-exchanger type MCFC stack. They used numerical method to evaluate the effect of the gas channel height on the uniformity and pressure loss of the gas flow. Recently, Okada et al [46] presented an investigation of the gas distribution in a large-scale stack with internal reforming MCFC stack. They proposed a large-scale stack divided into four blocks from the point of view of the gas flow scheme in order to achieve more uniform supply gas to each cell. The results showed that the flow variation among the four blocks is less than 1.5%, and it can improve the prospects for a MCFC stack.

1.5. Objectives of Present Studies

The above literature review shows that there is still much necessity to research the complex temperature and current density distributions in the MCFCs due to the mal-distributed inlet flow rate. Moreover, the relationships between the mole

fraction of each species, concentrations, over-potential, temperature, and current density can be more clearly by our investigation when the MCFC is under cross-flow configuration. In this study, the model of an MCFC with inlet flow mal-distribution is developed and numerically solved to enhance the understanding of the underlying characteristics of non-uniform effects, as well as various factors that dominate the temperature and current density distribution of the MCFCs.

The scopes of this investigation mainly focus on three parts. First, we study the effect of non-uniform inlet flow in the transverse direction on the temperature and current density of an MCFC unit. In this study, the distribution of inlet flow rate in the transverse direction includes the uniform, increasing, and decreasing profiles, and these profiles in anode and cathode assemble to eight patterns. Furthermore, this study examines the temperature and current density distributions in the eight patterns, and compares them to the results in uniform inlet flow. The second part investigates the effects of inlet flow mal-distribution in the stack direction on the thermal and electrical performance of a ten-stack MCFC. This study uses the numerical procedure for a MCFC unit to calculate the quasi-three dimensional temperature and current density fields in the MCFC stack by averaging the temperatures of top and down separators, which connect together between stacks. Scenarios of non-uniform inlet flow of either anode side or cathode side have been calculated and discussed in this study. The electric performance of a planar MCFC unit with cross-flow configuration when there is higher gas utilization in anode and cathode investigate in

the final part of this dissertation. A phenomenon of the existence of non-reaction zone arising from the non-uniform inlet pattern is demonstrated and its influence on cell performance is explored.

Table 1.1 The types of fuel cells

Name	Electrolyte	Operating Temperature (℃)	Charge carrier	Catalyst	Prime cell components
Alkaline Fuel Cell	Liquid KOH	65-220	OH^-	Pt	Carbon based
Phosphoric Acid Fuel Cell	Liquid H_3PO_4	200	H^+	Pt	Carbon based
Polymer Electrolyte Fuel Cell	Ion Exchange membranes	80	H^+	Pt	Graphite based
Molten Carbonate Fuel Cell	CO_3 melt	650	CO_3^{2-}	Ni	Stainless steel based
Solid Oxide Fuel Cell	Ceramic	600-1000	O^{2-}	$CaTiO_3$	Ceramic

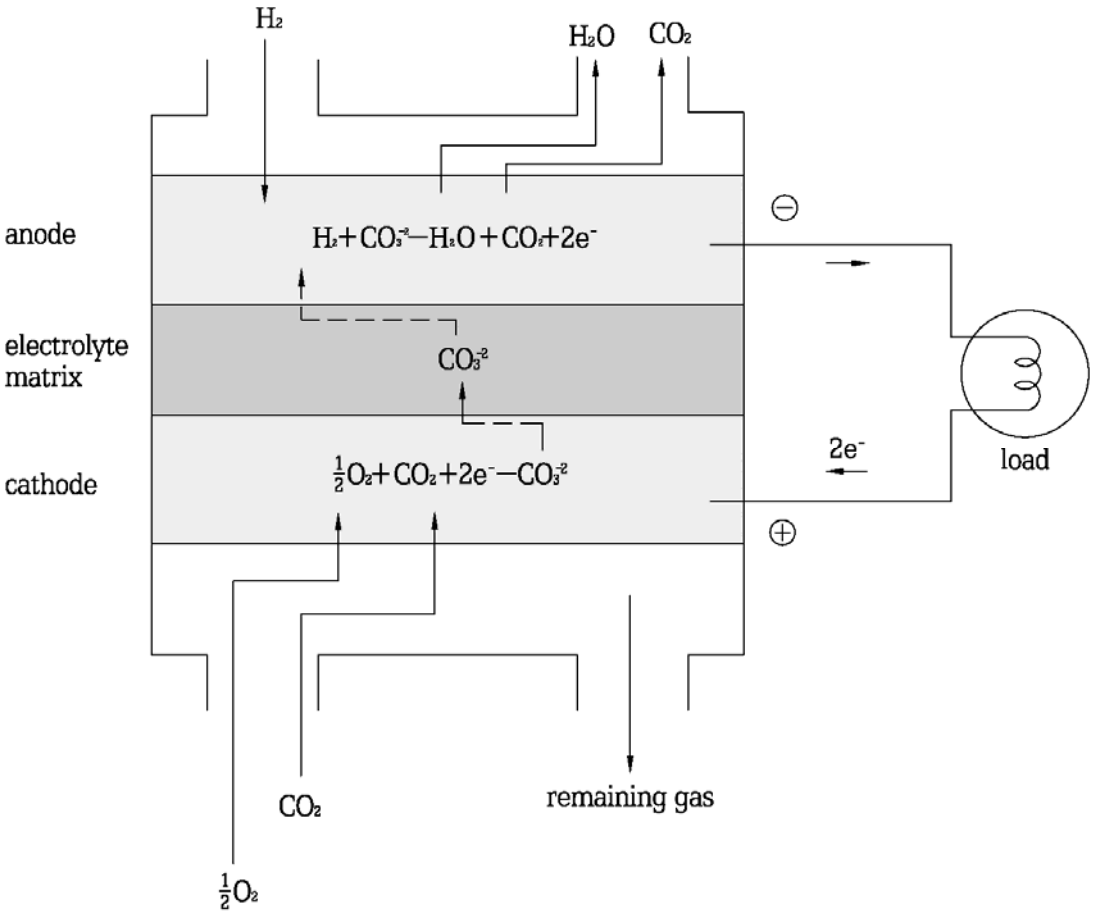

Fig 1.1. Operating principle of a MCFC

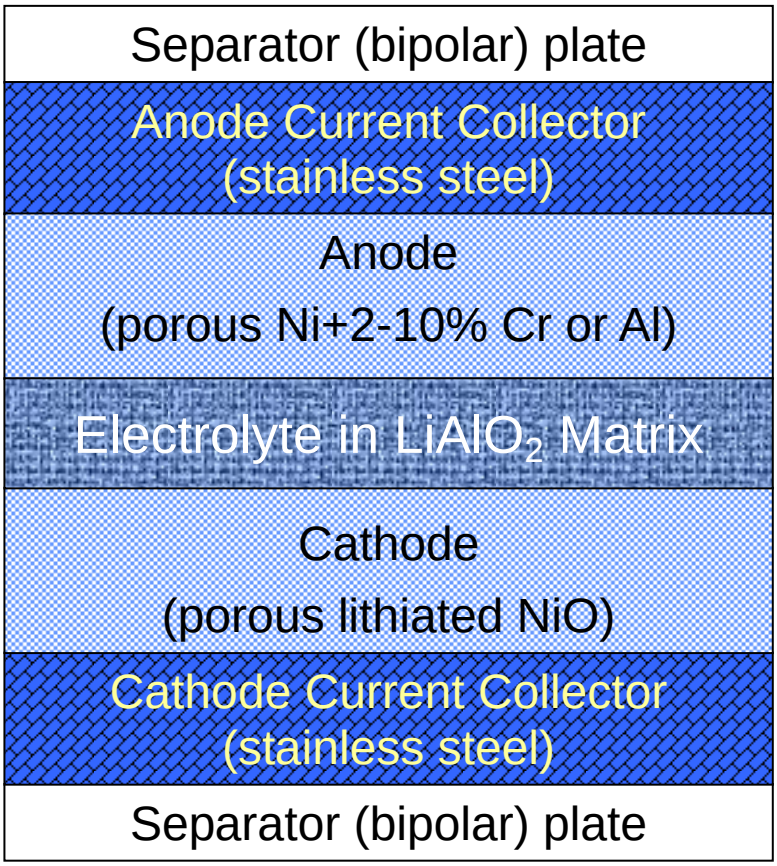

Fig 1.2. Component diagram of a unit cell

2. Effect of Inlet Flow Maldistribution on the Thermal and Electrical Performance of an MCFC Unit

2.1. Physical Model Description

This study investigates a unit of a molten carbonate fuel cell with an area of 0.6m ×0.6m when the anode gas and the cathode gas flow in the cross-flow configuration, in which the anode gas flows in the x direction, and the cathode gas flows in the y direction, as shown in Figure 2.1. The ribs of separator cause the anode gas and the cathode gas to flow without mixing, therefore each flow is considered to composed of many flow tubes that are parallel to each other. As mentioned in Chapter 1, the position of the manifold may induce different mal-distributions of the flow rate in the inlet ports. This study considers eight patterns of inlet flow scenarios from three kinds of profiles: uniform, progressively decreasing, and progressively increasing, as shown in Figure 2.2. The term d represents the unilateral deviation of the non-uniform profile, which is the ratio of the variation of flow rate in one side to the mean flow rate.

2.2. Basic Assumption

The formulations of the governing equations are based on the following assumptions.

5. Steady state.

6. The gas flow in the anode channel and the cathode channel are treated as a plug-flow.

7. The inlet temperature and molar fractions of species in the anode gas and the cathode gas are constant and uniform.

8. The thermal properties of the anode gas, the cathode gas, the cell and the separator are constant, except for the specific heat capacities of the anode gas and the cathode gas.

9. The boundaries of the cell and separator are adiabatic.

10. The properties variations in the z direction are negligible.

11. The cross-sectional geometry of separator is unchanged throughout the x-y plane.

12. The water-shift reaction in the anode gas is negligible.

13. The cell voltage is uniform over the cell plane.

2.3. Governing Equations

2.3.1. Reaction Equations

This study considers a molten carbonate fuel cell unit with external reforming and the reforming reaction in the anode gas is neglected. The cathode gas is the air obtained from the atmosphere, and the electricity is generated in the cell through the

electrochemical reaction in the anode and the cathode. Meanwhile, the electrolyte is a porous matrix that contains migrating ions of molten carbonate. The reactions in the anode and the cathode are as follows.

$$H_2 + CO_3^{2-} \rightarrow H_2O + CO_2 + 2e^- \tag{2.1}$$

$$O_2 + 2CO_2 + 4e^- \rightarrow 2CO_3^{2-} \tag{2.2}$$

2.3.2. Mass Conservation Equations

The relationship between the current density and gas molar flux for species at the electrodes surface is described from Faraday's law. Therefore, the mass balances of the anode and the cathode gases are as follows.

$$\frac{1}{L_y}\frac{dn_{ag,k}}{dx} = \pm\frac{i}{n_e F} \tag{2.3}$$

$$\frac{1}{L_x}\frac{dn_{cg,k}}{dy} = \pm\frac{i}{n_e F} \tag{2.4}$$

where n is the mole flow rate of the k-component, and n_e is the number of electrons transferred in the reactions of the anode and the cathode. The plus/minus symbol represents an increase/decrease in each species' mole flow rate caused by the electrochemical reaction in the anode and the cathode. It is positive for reactants, and negative for products in the anode and the cathode.

2.3.3. Energy Conservation Equations

This work applies the conservation of energy for anode gas, cathode gas, the cell

and the separator. For the gas in the anode flow channel,

$$\frac{d}{dx}\left(\sum n_{ag,k} c_{p,k} T_{ag}\right) = \dot{q}_{conv,s-ag} + \dot{q}_{conv,c-ag} + \dot{q}_{mass,c-ag} \tag{2.5}$$

$$T_{ag}(0, y) = 858K \tag{2.6}$$

For the gas in the cathode flow channel,

$$\frac{d}{dy}\left(\sum n_{cg,k} c_{p,k} T_{cg}\right) = \dot{q}_{conv,s-cg} + \dot{q}_{conv,c-cg} - \dot{q}_{mass,cg-c} \tag{2.7}$$

$$T_{cg}(x, 0) = 867K \tag{2.8}$$

For the cell,

$$\begin{aligned} &(k\delta)_c \frac{\partial^2 T_c}{\partial x^2} + (k\delta)_c \frac{\partial^2 T_c}{\partial y^2} - \dot{q}_{cont} - \dot{q}_{conv,c-ag} \\ &-\dot{q}_{conv,c-cg} + \dot{q}_{mass,cg-c} - \dot{q}_{mass,c-ag} + \dot{q}_{reac} = 0 \end{aligned} \tag{2.9}$$

$$\left.\frac{\partial T_c}{\partial x}\right|_{x=0} = \left.\frac{\partial T_c}{\partial x}\right|_{x=L_x} = \left.\frac{\partial T_c}{\partial y}\right|_{y=0} = \left.\frac{\partial T_c}{\partial y}\right|_{y=L_y} = 0 \tag{2.10}$$

For the separator,

$$(k\delta)_s \frac{\partial^2 T_s}{\partial x^2} + (k\delta)_s \frac{\partial^2 T_s}{\partial y^2} + \dot{q}_{cont} - \dot{q}_{conv,s-ag} - \dot{q}_{conv,s-cg} = 0 \tag{2.11}$$

$$\left.\frac{\partial T_s}{\partial x}\right|_{x=0} = \left.\frac{\partial T_s}{\partial x}\right|_{x=L_x} = \left.\frac{\partial T_s}{\partial y}\right|_{y=0} = \left.\frac{\partial T_s}{\partial y}\right|_{y=L_y} = 0 \tag{2.12}$$

where the heat transfer rate terms are described in Table 2.1. In Eqs (2.3) to (2.7), this study considers the molar flow rate of the anode gas and cathode gas are a progressively decreasing profile, a progressively increasing profile, or a uniform

profile in the inlet. The inlet conditions are described as following.

$$n_{ag}(0,y)=\frac{N_{ag}}{L_y}\left(\frac{2d}{L_y}y+1-d\right) \tag{2.13}$$

$$n_{cg}(x,0)=\frac{N_{cg}}{L_x}\left(\frac{2d}{L_x}x+1-d\right) \tag{2.14}$$

where N_{ag} and N_{cg} are the total molar flow rate of the anode gas and the cathode gas from inlet ducts, and the deviation of d may be negative, zero, and positive, representing the progressively decreasing profile, uniform profile, and progressively increasing profile, respectively. In Table 2.1, k_{c-s} is the thermal conductivity due to the contact resistance between the cell and the separator in the z direction. The thermal conductivity, k_{c-s}, is set to 1.0 $W\cdot m^{-1}K^{-1}$.

2.3.4. Nernst Voltage and Polarizations

The Nernst voltage is calculated using the Nernst equation, as follows.

$$E=E_0+\frac{RT}{2F}\ln\left(\frac{P_{H_2}P_{O_2}^{0.5}P_{CO_2,cg}}{P_{H_2O}P_{CO_2,ag}}\right) \tag{2.15}$$

$$E_0=1.2723-2.7654\times10^{-4}T \tag{2.16}$$

Meanwhile, E_0 is the reversible voltage under standard conditions. According to the results in, this study uses the total cell resistance, including that due to cathode polarization, the electrolyte tile contribution, and the Ohmic resistance of the contacts. Note that this total cell resistance did not include the concentration polarization,

Because we assumed the diffusion is non-limiting in the electrode. The cell voltage is the Nernst voltage minus the over-potentials, as follows.

$$V = E - iR_{tot} \tag{2.17}$$

$$R_{tot} = \frac{Ae^{B/T}}{\prod_i p_i^{\beta_i}} + c_{ir} + D \cdot e^{F/T} \tag{2.18}$$

where the parameters are $\beta^{O_2} = 0.67$, $A = 1.38 \times 10^{-7} \Omega m^2 Pa^{0.67}$, B=11400K, $c_{ir} = 0.348 \times 10^{-4} \Omega m^2$, $D = 4.8 \times 10^{-8} \Omega m^2$ and F=6596K .

The above simultaneous equations of the MCFC contain seven unknown variables, which are mole flow rate of each species ($n_{ag,k}$ and $n_{cg,k}$), anode gas temperature (T_{ag}), cathode gas temperature (T_{cg}), cell temperature (T_c), separator temperature (T_s), current density (i), and cell voltage (V). The mass equations are used to determine mole flow rate of each species, and energy equations are used to determine the temperatures. Nevertheless, in Eq. (2.17), both current density and cell voltage variables must be evaluated. Therefore, this study assumes that the cell voltage is uniform over the reaction area of the cell and then calculates the current density using Eq. (2.17).

2.4. Method of Solution

This study divides the calculation domain of the x-y plane into $N \times N$ subdivisions as shown in Figure 2-3, and assigns the calculation nodes of $n_{ag,k}$ and

T_{ag} at the inlet and outlet of each subdivision in the x direction of the anode gas flowing. Similarly, the calculating nodes of $n_{cg,k}$ and T_{cg} are assigned to the inlet and outlet of each subdivision in the y direction of the cathode gas flowing. Furthermore, the calculation nodes of i, T_c, and Ts are assigned to the center of the subdivision. Grid generation and the implicit scheme are adopted to discretize Eqs. (2.3) to (2.11) to finite difference equations, and then employs TDMA (Tri-Diagonal Matrix Algorithm) to solve simultaneous algebraic equations. This node arrangement avoids the need to apply the upwind method to treat the first-order differential terms, and has been used to calculate the temperature fields of a three-gas cross-flow heat exchanger. [42]

The Eq. (2.3) and (2.4) can be discretized to the following based on different species in anode and cathode side, respectively.

For the gas in the anode flow channel,

$$n_{H_{2(i+1,j)}} = n_{H_{2(i,j)}} - \frac{i_{(i,j)} \cdot \Delta x}{2F}, \tag{2.19}$$

$$n_{H_2O_{(i+1,j)}} = n_{H_2O_{(i,j)}} + \frac{i_{(i,j)} \cdot \Delta x}{2F}, \tag{2.20}$$

$$n_{CO_{2(i+1,j)}} = n_{CO_{2(i,j)}} + \frac{i_{(i,j)} \cdot \Delta x}{2F} \tag{2.21}$$

For the gas in the cathode flow channel,

$$n_{CO_{2(i,j+1)}} = n_{CO_{2(i,j)}} - \frac{i_{(i,j)} \cdot \Delta y}{2F} \tag{2.22}$$

$$n_{O_{2(i+1,j)}} = n_{O_{2(i,j)}} - \frac{i_{(i,j)} \cdot \Delta y}{4F} \tag{2.23}$$

The Eqn. (2.5) to (2.11) for energy conservation equations of the gas in the anode flow channel, cathode flow channel, cell, and separator can be discretized to the following finite difference equations

For the gas in the anode flow channel,

$$\left(\left(\frac{\sum\left(n\cdot c_p\right)_f}{\Delta x}\right)_{(i+1,j)}+\frac{h_f a_{cf}}{2}+\frac{h_f a_{sf}}{2}\right)T_{f_{(i+1,j)}}=$$
$$\left(\left(\frac{\sum\left(n\cdot c_p\right)_f}{\Delta x}\right)_{(i,j)}-\frac{h_f a_{cf}}{2}-\frac{h_f a_{sf}}{2}\right)T_{f_{(i,j)}} \qquad (2.24)$$
$$+\frac{i_{(i,j)}}{2F}\left(-c_{p_{H_2}(i,j)}+c_{p_{CO_2}(i,j)}+c_{p_{H_2O}(i,j)}\right)\cdot T_{c_{(i,j)}}+h_f a_{cf}T_{c_{(i,j)}}+h_f a_{sf}T_{s_{(i,j)}}$$

For the gas in the cathode flow channel,

$$\left(\left(\frac{\sum\left(n\cdot c_p\right)_o}{\Delta y}\right)_{(i,j+1)}+\frac{h_o a_{co}}{2}+\frac{h_o a_{so}}{2}\right)T_{o_{(i,j+1)}}=$$
$$\left(\left(\frac{\sum\left(n\cdot c_p\right)_o}{\Delta y}\right)_{(i,j)}-\frac{h_o a_{co}}{2}-\frac{h_o a_{so}}{2}\right)T_{o_{(i,j)}}-\frac{i_{(i,j)}}{4F}\left(c_{p_{O_2}(i,j)}+2c_{p_{CO_2}(i,j)}\right)\cdot T_{c_{(i,j)}} \qquad (2.25)$$
$$+h_o a_{co}T_{c_{(i,j)}}+h_o a_{so}T_{s_{(i,j)}}$$

For cell,

$$\left(\frac{2\left(k\delta\right)_c}{\Delta x^2}+\frac{2\left(k\delta\right)_c}{\Delta y^2}+h_f a_{cf}+h_o a_{co}\right)T_{c_{(i,j)}}=\left(\frac{\left(k\delta\right)_c}{\Delta y^2}\right)T_{c_{(i,j+1)}}+\left(\frac{\left(k\delta\right)_c}{\Delta y^2}\right)T_{c_{(i,j-1)}}$$
$$+\left(\frac{\left(k\delta\right)_c}{\Delta x^2}\right)T_{c_{(i+1,j)}}+\left(\frac{\left(k\delta\right)_c}{\Delta x^2}\right)T_{c_{(i-1,j)}}+\left(\frac{h_f a_{cf}}{2}\left(T_{f_{(i+1,j)}}+T_{f_{(i,j)}}\right)\right) \qquad (2.26)$$
$$+\left(\frac{h_o a_{co}}{2}\left(T_{o_{(i,j+1)}}+T_{o_{(i,j)}}\right)\right)-q$$

For separator,

$$\left(\frac{2(k\delta)_s}{\Delta x^2}+\frac{2(k\delta)_s}{\Delta y^2}+h_f a_{sf}+h_o a_{so}\right)T_{s_{(i,j)}}=\left(\frac{(k\delta)_s}{\Delta y^2}\right)T_{s_{(i,j+1)}}$$
$$+\left(\frac{(k\delta)_s}{\Delta y^2}\right)T_{s_{(i,j-1)}}+\left(\frac{(k\delta)_s}{\Delta x^2}\right)T_{s_{(i+1,j)}}+\left(\frac{(k\delta)_s}{\Delta x^2}\right)T_{s_{(i-1,j)}} \quad (2.27)$$
$$+\left(\frac{h_f a_{sf}}{2}\left(T_{f_{(i+1,j)}}+T_{f_{(i.j)}}\right)\right)+\left(\frac{h_o a_{so}}{2}\left(T_{o_{(i,j+1)}}+T_{o_{(i.j)}}\right)\right)$$

The calculation proceeds as follows

14. The program guesses a uniform current density distribution and solves the mole flow rate of each species in the anode flow channel and the cathode flow channel using Eqs. (2.19) to (2.23)

15. The program solves the temperature fields of the gas in the anode channel, the gas in the cathode channel, the cell, and the separator using Eqs. (2.24) to (2.27), respectively.

16. The Nernst voltage and internal total resistance are calculated using Eqs. (2.15) and (2.18), and then the current density is obtained from the Eq. (2.17)by setting the cell voltage to a constant value.

17. The current density is updated to Step 1, and the loop iterated from Step 1 to Step 4 until all relative errors of the mole flow rates, the temperature and the current density satisfy the converge criterion.

Figure 2-4 to Figure 2-7 depict the temperature of the anode gas, cathode gas,

cell, and separator at the central point of calculating domain, respectively. In these figures, the number of grid points increases from 100×100 to 1000×1000 for FORTRAN program calculations, and the variations of anode gas temperature, cathode gas temperature, cell temperature, and separator temperature in the central position are stable between 100×100 and 400×400. However, the variation of temperature becomes unstable when the number of grid points are higher than 500×500. It downs first and then rise again when the number of grid points are higher than 700×700. The variations of current density and temperature are similar, as shown in Figure 2-8. Therefore, this study selects the grid number of 400×400 as the dimension size in the FORTRAN program for calculating the results.

FlexPDE software is adopted to solve the Eqs. (2.3) to (2.18), to verify the accuracy of calculation, because FlexPDE is a flexible solver of partial differential equations by using the finite element algorithm.

Figure 2.4 depicts the temperature distribution of the cell calculated both numerically method and using FlexPDE software at a cell voltage of 0.8V. In this numerical method, the grid dimension depends on the mole flow rates of the anode gas and the cathode gas, and must increase as the mole flow rate falls to avoid the negative values in the finite difference equations [47]. In this comparison case, the numerical program sets the grid dimensions to be 400×400 with a convergence criterion of 1×10^{-5}, and FlexPDE uses 1972 elements with a convergence criteria of

0.002. The continuous lines clearly match the dashed lines in this figure. Therefore, the numerical method for calculating the temperature field is reliable. In the electrical performance calculation, Fig. 2.5 shows the current density distributions calculated by the numerical method herein this study and using FlexPDE software. Similarly, the continuous lines coincide with the dashed lines over the whole x-y plane. Consequently, the numerical calculation of electrical performance is also reliable. Table 2.2 lists all parameters and conditions in the comparison case and references relevant literature. Meanwhile, the effective contact thickness between the cell and the separator is the average thickness of the cell and the separator. Furthermore, the $Nu = 3.35$ [48] is adopted to estimate the convection heat transfer coefficient in this study, because the flows of anode gas and cathode gas are fully developed and laminar.

2.5. Results and Discussion

Figure 2.9 depicts the temperature distribution of the cell when the inlet flows are uniform. The isotherm increases from under 600°C close to both the inlets of the anode gas and the cathode gas to 638°C near the corner of both gases outlets . When the anode gas and the cathode gas flow through the reaction area of the cell, they not only supply the reaction species but also carry away the reaction heat in the cell. Therefore, the anode gas and the cathode gas accumulate all of the reaction heat and reach their maximum temperatures when they flow to the outlets. The temperatures

of the gases also influence the temperature distribution of the cell and separator because coupled heat transfer occurs among them. In this figure, the isotherm in the y direction increases more uniform than that in the x direction. Hence, the cathode gas dominates the cell cooling because it has a higher flow rate than the anode gas.

Figure 2.10 displays the current density distribution on the cell plane under the same conditions as in Fig. 2.9. The minimum current density is $1316\,A\cdot m^{-2}$ in the corner of the cathode gas inlet and the anode gas outlet, and the maximum current density is $1846\,A\cdot m^{-2}$ in the middle-left outlet of the cathode gas. When the cell voltage is set to be a constant, the Nernst voltage and the internal resistance of the cell directly affect the current density according to the Ohmic law. With respect to the relationship between the Nernst voltage and the current density, examining the Eq. (2.15) indicates that the concentration of gas species influences the Nernst voltage, which declines as the concentrations of hydrogen and oxygen drop. Since the cathode gas is easily obtained from the environment and thus has a larger flow rate in order to cool the cell, the variation of the oxygen concentration is less than the hydrogen concentration. Consequently, the current density fell should decrease in the x direction of the anode gas flow, because the Nernst voltage fell with the drop in hydrogen concentration. With respect to the relationship between internal resistance and current density, Fig. 2.11 presents the total internal resistance distribution on the cell plane. The total internal resistance is defined in Eq. (2.18) which obtained from Bosio et al [30]. In this figure, the continuous line and dashed line are represented

the results of FORTRAN program and FlexPDE, respectively. The results of FORTRAN program agree well with the results of FlexPDE. In Fig. 2.11, it shows that the distribution of total internal resistance is similar to the distribution of current density, but reaches a minimum in the middle-right outlet of cathode gas. The area of lower internal resistance represents it has higher current density when the cell voltage is set to be constant. When both the effect of the concentration of species and the total internal cell resistance are considered, it is reasonable that the contour with maximum current density moves left as determined by comparing Fig. 2.11 to Fig. 2.10 because of the effect of the concentration of hydrogen.

Figures 2.12(a) to 2.12(h) show the systematic cell temperature distribution of eight patterns with a deviation of 0.5. Meanwhile, $\overline{T}$ and ΔT represent the average and variation of cell temperature, respectively. In these figures, it shows that the dominated factor on cell temperature distribution is the cathode gas, because the main trend of isotherm is increasing along the y direction of cathode gas flowing. In Fig. 2.2, Patterns A to B, C to E, and F to H have the same inlet flow profile of the cathode gas in each group. In Figs. 2.12(a) and 2.12(b), the cell temperature distributions of Patterns A and B are similar, and the main trend of cell temperature increases from under 600°C in the inlet of cathode gas to 636-638°C in the outlet of the cathode gas along the y direction, which is close to that in Fig. 2.9 with uniform inlet flow of the anode and the cathode gases. The cell temperature distribution of Patterns C, D, and E are similar to each other, and Figs. 2.12(c) to 2.12(e) show that

the isotherm range is from under 600°C to 638-640°C, and the highest temperature moves from the corner of the outlet of both cathode gas and anode gas to the middle of the cathode gas outlet. Examining the inlet flow profile of Patterns C to E indicates that the flow rate of cathode gas progressively increases in the x direction. Since the part that is close to the outlet of the anode gas has more cathode gas to cool the cell, the highest temperature in the corner moves to the left, as revealed by comparing Figs. 2.12(a) and 2.12(b), which have uniform cathode inlet flow. In Figs. 2.12(f) to 2.12(h), Pattern F, G, and H also have analogous temperature distribution of the cell, and these figures show that the temperature distribution of the cell is from under 600°C to 648-649°C, and the highest temperature occurs in the corner of the outlet of the cathode gas and the anode gas. Notably, the variation of cell temperature in Patterns F to H is about 58°C, and it is wider than that in Patterns A to E, so this is the worst temperature distribution. Patterns F to H have the same inlet flow profile of the cathode gas, which is progressively decreasing in the x direction. This non-uniform inlet flow causes less cathode gas to flow through the part with higher temperature on the cell, where is near the outlet of the anode gas. Therefore, the highest temperature in Figs. 2.12(f) to 2.12(h) rises more than those in Figs. 2.12(a) to 2.7(e). This study selects the cell temperature field of Pattern B and F, which has the least and most temperature variation, to subtract the cell temperature field in uniform pattern, and then show the results in Fig. 2.13. In this figure, the temperature difference of Pattern B related to uniform pattern is between -3 and 5°C,

as well as the largest temperature difference of Pattern F related to uniform pattern occurs at the corner of gas outlet and it is over 12°C.

Figure 2.14 plots the systematic cell current density distribution of eight inlet flow patterns with a deviation of 0.5. Meanwhile, $\bar{i}$ and Δi represent the average and the variation of current density, respectively. In this figure, the current density distribution of Pattern A is similar to those of Patterns D and G, and that of the current density distribution of Pattern B is analogous with those of Patterns E and H. Similarly, the current density distribution of Pattern C is similar to that of Pattern F. The inlet flow profile of each pattern in Fig. 2.2 indicates that Patterns A, D, and G, Patterns B, E, and H, and Patterns C and F represent three groups whose members have same profile of anode gas inlet flow in each group. Therefore, the inlet flow pattern of the anode gas dominates the current density distribution. As mentioned in the second paragraph of this section, the concentration of hydrogen and the total resistance of the cell influence the current density. An anode gas flows faster with a less varying hydrogen concentration, and with a more uniform current density distribution as the uniformity of the Nernst voltage increases. On the contrary, an anode gas flows more slowly and with a greater change in the hydrogen concentration because of the consumption of hydrogen in the chemical reaction, with a greater change of current density in the direction of flow of the anode gas. In Figs. 2.14(c) and 14(f), the current density distributions are similar to that in Fig. 2.10 because the inlet flows of anode gas have the same uniform profile. In Figs. 2.14(a), 2.14(d), and

2.14(g), it is clear that the current density distribution at the top half of the cell is clearly more uniform than that in the bottom half of the cell, because the inlet flow of anode gas in Patterns A, D, and G progressively increase in the y direction. Figures 2.14(b), 2.14(e), and 2.14(h) show that the distributions of current density in the bottom half are more uniformly than the distributions of current density in the top half of the cell, because Patterns B, E, and H have a progressively decreasing inlet flow rate of the anode gas in the y direction. Figure 2.14 shows that the current density difference of Pattern D and F related to the uniform pattern, because Pattern D and Pattern F have the most and least current density variation in Fig. 2.14. In Fig. 2.15(a), the current density difference of Pattern D is between –365 and 173 $A \cdot m^{-2}$, and the maximum difference occurs near the outlet of anode gas. The current density difference of Pattern F related to uniform pattern is between –30 and 53 $A \cdot m^{-2}$, so it seems flat in Fig. 2. 15 (b).

This study calculates all patterns in Fig. 2.2 with three deviations of 0.25, 0.5 and 0.75. Table 2.3 presents the results, and Fig. 2.16 presents them as histograms. The vertical axis represents the relative variation of temperature or current density in non-uniform patterns to uniform pattern. Meanwhile, ΔT and Δi represent the difference between the maximum and minimum temperature and current density on the cell. In Fig. 2.16(a), the relative variation between average cell temperature and that in the uniform inlet flow is always $\pm 0.4\%$ for all deviations. Consequently, the non-uniform inlet flow affects slightly the average cell temperature and this effect can

be ignored. In Fig. 2.16(b), the absolute relative variation between the average current density and that in uniform inlet flow is always lower than 5% for all deviations. The variations of average current density in Pattern C and Pattern F are very small and there are almost to be zero. That means the more uniform the inlet of the anode gas is, the smaller the average current density will be. Moreover, the inlet of the cathode gas is non-uniform. Additionally, the relative variations of average current density in Pattern B, Pattern E and Pattern H are much worse than in the other patterns, and are close to –5% at a deviation of 0.75. Examining the patterns in Fig. 2.2 shows that all of them have progressively decreasing inlet flow in anode gas. Based on the Eq. (2.15) and Eq. (2.18), increasing the cell temperature increases the Nernst voltage and reduces the total cell resistance. Therefore, the current density increases with the cell temperature as the Nernst voltage gets increases and total cell resistance in Eq. (2.17) declines. According to the results in Fig. 2.12 and Fig. 2.14, the temperature and the current density in the top part of the cell plane are higher than those in the bottom part. The higher current density causes more hydrogen to be consumed in this area. Therefore, the consumption of hydrogen in this area is more than that in other area due to the higher current density. In Pattern B, E, and H, since the mole flow rate in the top part is less than that in the bottom part due to the progressively decreasing inlet profile of anode gas, the average current density will drop due to the lack of hydrogen. Therefore, the progressively decreasing inlet flow profile in anode gas is the worst for average current density.

Figures 2.16(c) and 2.16(d) represent the relative variation of cell temperature and current density distribution related to those in uniform inlet flow. The distribution of temperature is worst in Pattern F with a deviation of 0.75, for which the relative variation is 37%. The distribution of current density is worst in Pattern D with deviation of 0.75, for which the relative variation is 179%. Furthermore, authors find that some relative variations are negative in Figs. 2.16(c) and 2.16(d), indicating that the variation of temperature or current density in the non-uniform inlet flow is less than that in uniform flow. In Fig. 2.16(c), Pattern B exhibits a better distribution of temperature because the temperature difference decreases as the deviation of non-uniform profile increases. Moreover, Pattern F has a more intensive current density distribution than that in uniform in Fig. 2.16(d), because the values of relative variations are –3%, -6%, and –10% with deviations of 0.25, 0.5, and 0.75, respectively. Although the uniformity of temperature distribution in Pattern B is better than others flow patterns, the uniformity of current density distribution is the worthiest than others flow patterns. The uniformity of current density distribution in Pattern B is the worthiest, because there is a non-uniform inlet flow of the anode gas channel. The uniformity of current density distribution in Pattern F is better than other flow patterns, but the uniformity of temperature distribution is the worthiest than others flow patterns. The uniformity of temperature distribution in Pattern F is the worthiest, because its inlet flow pattern of the cathode gas channel is non-uniform. In Figs. 2.16(c) and 2.16(d), note that both Patterns A and B have better temperature

distribution than the other non-uniform patterns, and both Patterns C and F have a better current density distribution than the other non-uniform patterns. Examining the inlet flow profile in Fig. 2.2 indicates that Pattern A and B have uniform inlet flow of cathode gas, and Pattern C and F have uniform inlet flow of anode gas. Therefore, the uniform inlet flow in both the anode side and the cathode side is the best profile from the perspective cell temperature and current density distribution. In industrial applications, the position of the inlet manifold affects primarily the inlet flow distribution and the uniform inlet profile is difficult to obtain. Therefore, the uniform inlet flow is the goal of the design of an MCFC with a cross-flow configuration, and designers must avoid putting the inlet manifolds of the anode gas and the cathode gas too close to the side of another gas inlet, which would produce non-uniform inlet flow with a progressively decreasing profile. Such poor positions of manifolds would further reduce average current density, as shown in Pattern B and Pattern E in Fig. 2.16(b), and widen the cell's temperature distribution, as shown in Patterns F to H in Fig. 2.16(c).

2.6. Concluding Remarks

Non-uniform inlet flow rates of anode gas and cathode gas are practical because of the position of the manifold and the distributor geometry in a molten carbonate fuel cell. This study considered uniform, progressively increasing, and progressively decreasing profiles in the anode gas and the cathode gas, as well as combinations of

these profiles in the form of eight patterns of non-uniform inlet flow. Mass conservation, energy conservation and electrochemistry equations were considered, and the variation in the z direction ignored. Through the accuracy comparison in cell temperature and current density distribution, this study established the reliable numerical method by FORTRAN program. This study plots the temperature distribution and current density distribution on the cell plane in different patterns and draws the following conclusions. The cathode gas dominates the temperature distribution of the cell because of its flow rate exceeds that of the anode gas. The cell temperature is the highest in the corner of the outlet of the anode gas and the cathode gas in a uniform inlet flow pattern. The progressively increasing profile of the cathode gas moves the hot spot in the corner to the middle of cathode gas outlet. The progressively decreasing profile of the cathode gas increases the temperature of the hot spot in the corner, and degrades the temperature distribution. Therefore, the position of the inlet manifold of the cathode gas must not be near the corner of the cathode gas inlet and the anode gas inlet, because it would then cause the progressively decreasing profile of inlet flow, and widen the cell temperature distribution. The anode gas dominates the current density of the cell because of the hydrogen concentration. The progressively increasing profile of the anode gas leads to the largest variation of the current density, and the progressively decreasing profile of the anode gas leads to the lowest average current density. This result implies that the uniformity of the anode gas in the inlet is important to the design of distributors.

Moreover, the non-uniform inlet flow only slightly affects the average temperature and the current density of cell, but it influences more strongly the range and contour outlines of cell temperature and current density. For example, the temperature variation on the cell plane in Pattern G and the current density variation on the cell plane in Pattern D are 12% and 37% higher than those of the uniform pattern, respectively, when the deviation of the non-uniform profile is 0.25. Therefore, the effect of the inlet flow maldistribution on the temperature and current density distribution on the cell plane is apparent, and cannot be neglected as the deviation of the profile increases.

Table 2.1 Expressions of energy source terms in Eq.(2.5) to Eq.(2.11)

Symbols	Description	Expression
$\dot{q}_{conv,s-ag}$	Heat transfer rate from separator to anode gas by convection	$(ha)_{s-ag}\left(T_s - T_{ag}\right)$
$\dot{q}_{conv,s-cg}$	Heat transfer rate from separator to cathode gas by convection	$(ha)_{s-cg}\left(T_s - T_{cg}\right)$
$\dot{q}_{conv,c-ag}$	Heat transfer rate from cell to anode gas by convection	$(ha)_{c-ag}\left(T_c - T_{ag}\right)$
$\dot{q}_{conv,c-cg}$	Heat transfer rate from cell to cathode gas by convection	$(ha)_{c-cg}\left(T_c - T_{cg}\right)$
$\dot{q}_{mass,c-ag}$	Heat transfer rate due to ion immigration from cell to anode gas	$\frac{i}{2F} c_{p,CO_3^{2-}} T_c$
$\dot{q}_{mass,cg-c}$	Heat transfer rate due to ion immigration from cathode gas to cell	$\frac{i}{2F} c_{p,CO_3^{2-}} T_{cg}$
$\dot{q}_{cont}$	Heat transfer rate from cell to separator by contact conduction	$(ka)_{c-s} \frac{(T_c - T_s)}{\delta_{c-s}}$
$\dot{q}_{reac}$ [49]	Heat generation rate due to chemical reaction	$-\Delta H \times \frac{i}{2F} - V \cdot i$ $\Delta H = -240506 - 7.3835 T_c$

Table 2.2 Parameters and conditions in this study

Mole flow rate and molar fraction of species in anode inlet	
N_{ag}	0.0621 mol/s
X_{H_2}	0.203
X_{CO_2}	0.064
X_{H_2O}	0.15
X_{N_2}	0.583
Mole flow rate and molar fraction of species in cathode inlet	
N_{cg}	0.1841 mol/s
X_{O_2}	0.167
X_{N_2}	0.698
X_{CO_2}	0.135
Inlet temperature	
T_{ag}	858 K
T_{cg}	867 K
Operation Pressure	
P	3.5×10^5 Pa
Heat transfer area per unit area	
$a_{ag\text{-}s} = a_{cg\text{-}s}$	1.26 $m^2\ m^{-2}$
$a_{ag\text{-}c} = a_{cg\text{-}c}$	0.53 $m^2\ m^{-2}$
$a_{c\text{-}s}$	0.47 $m^2\ m^{-2}$
Conductivity	
k_c	9 $W\ m^{-1}K^{-1}$
k_s	25 $W\ m^{-1}K^{-1}$
k_{c-s}	1.0 $W\ m^{-1}K^{-1}$
Thickness	
δ_c	0.0023 m
δ_s	0.002 m
δ_{c-s}	0.00215 m

Table 2.3 Relative variation of cell temperature and current density at different non-uniform inlet flow patterns related to at uniform inlet flow pattern

	$\frac{\overline{T}_c - \overline{T}_{c,uniform}}{\overline{T}_{c,uniform}}$ (%)			$\frac{\bar{i}_c - \bar{i}_{c,uniform}}{\bar{i}_{c,uniform}}$ (%)			$\frac{\Delta T_c - \Delta T_{c,uniform}}{\Delta T_{c,uniform}}$ (%)			$\frac{\Delta i_c - \Delta i_{c,uniform}}{\Delta i_{c,uniform}}$ (%)		
	d=0.25	d=0.50	d=0.75	d=0.25	d=0.50	d=0.75	d=0.25	d=0.50	d=0.75	d=0.25	d=0.50	d=0.75
A	-0.0160	-0.0676	-0.1907	-0.1833	-1.1626	-3.5033	2.4545	3.2414	2.0600	33.0081	81.0958	164.6495
B	-0.0121	-0.0499	-0.0814	-0.4891	-1.8122	-4.5346	-0.0149	-2.0771	-7.2740	-15.302	35.2631	131.6049
C	0.0143	0.0582	0.1193	-0.0026	-0.0055	-0.1369	0.8594	4.5487	10.3150	3.6401	7.1689	12.0035
D	0.0063	0.0328	0.0607	-0.1659	-1.0670	-3.3795	3.3161	7.7346	9.5686	36.9351	90.1642	179.2814
E	-0.0026	0.0005	0.0095	-0.5184	-1.8799	-4.7295	1.1046	3.5997	5.9902	-8.5275	46.5420	141.3524
F	0.0330	0.0992	0.2094	0.0403	0.0949	-0.0313	9.4151	23.5280	37.2358	-2.8645	-5.8102	-9.9523
G	0.0089	0.0040	-0.0438	-0.1568	-1.1202	-3.5865	11.5262	23.4491	28.7527	29.5586	73.8560	154.2792
H	0.0350	0.0888	0.1626	-0.4400	-1.6696	-4.4963	9.2487	22.6260	33.8558	-21.0292	29.8983	147.1528

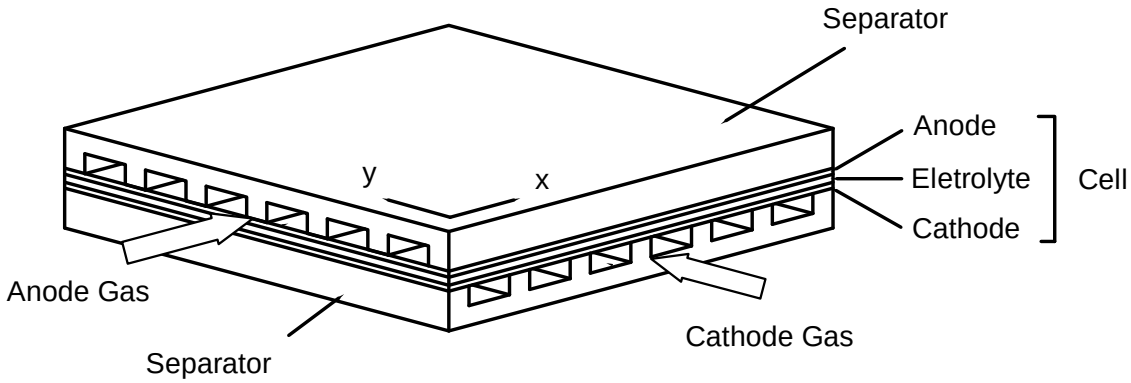

Fig 2.1. Schematic diagram of a molten carbonate fuel cell unit in crossflow

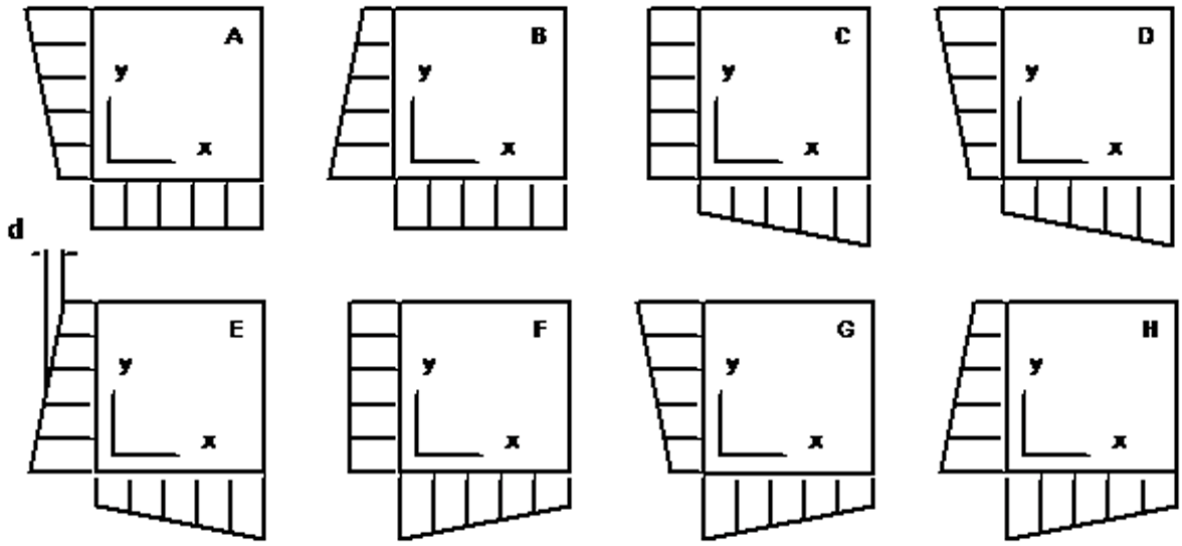

Fig 2.2. Patterns of non-uniform inlet flow profile in Chapter 2

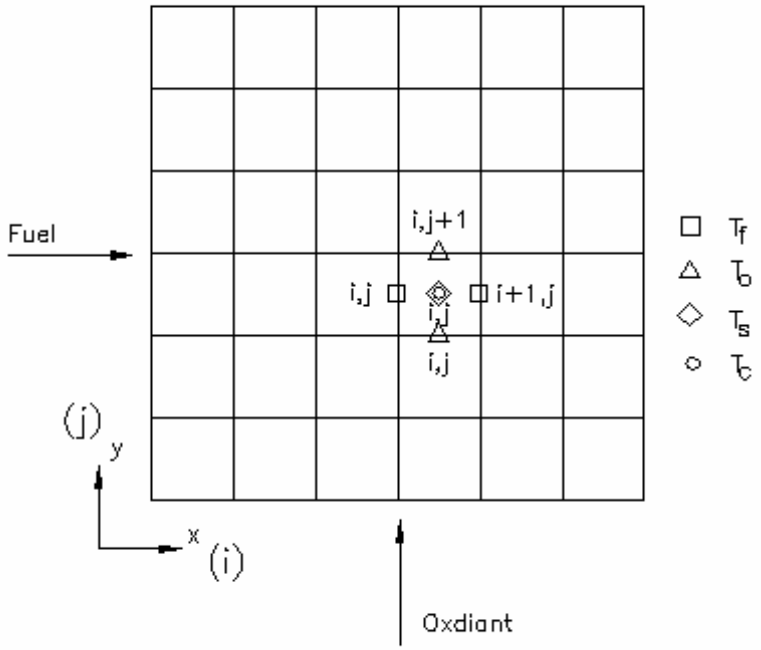

Fig 2.3. Calculated node arrangement in this study

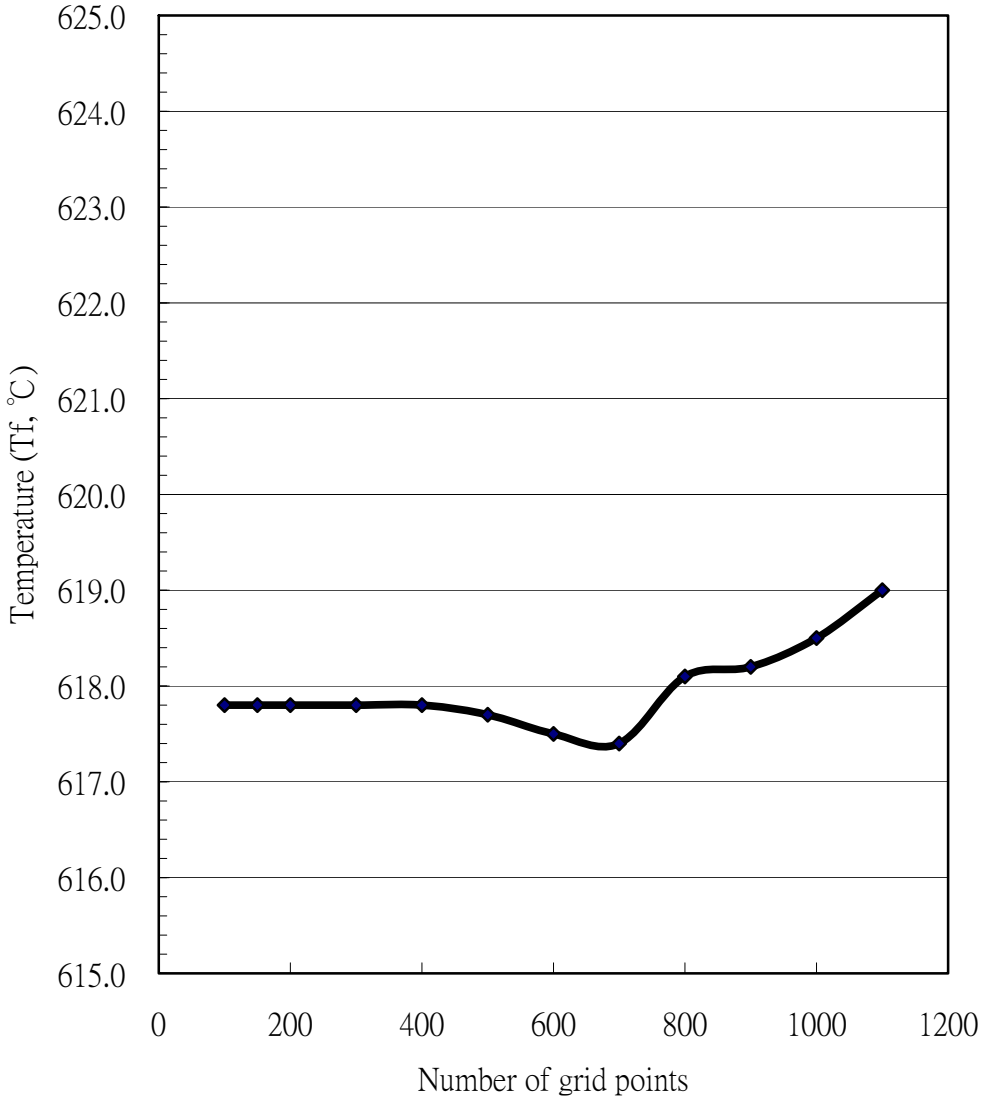

Fig 2.4. Anode gas temperature at the central point versus grid numbers in numerical program.

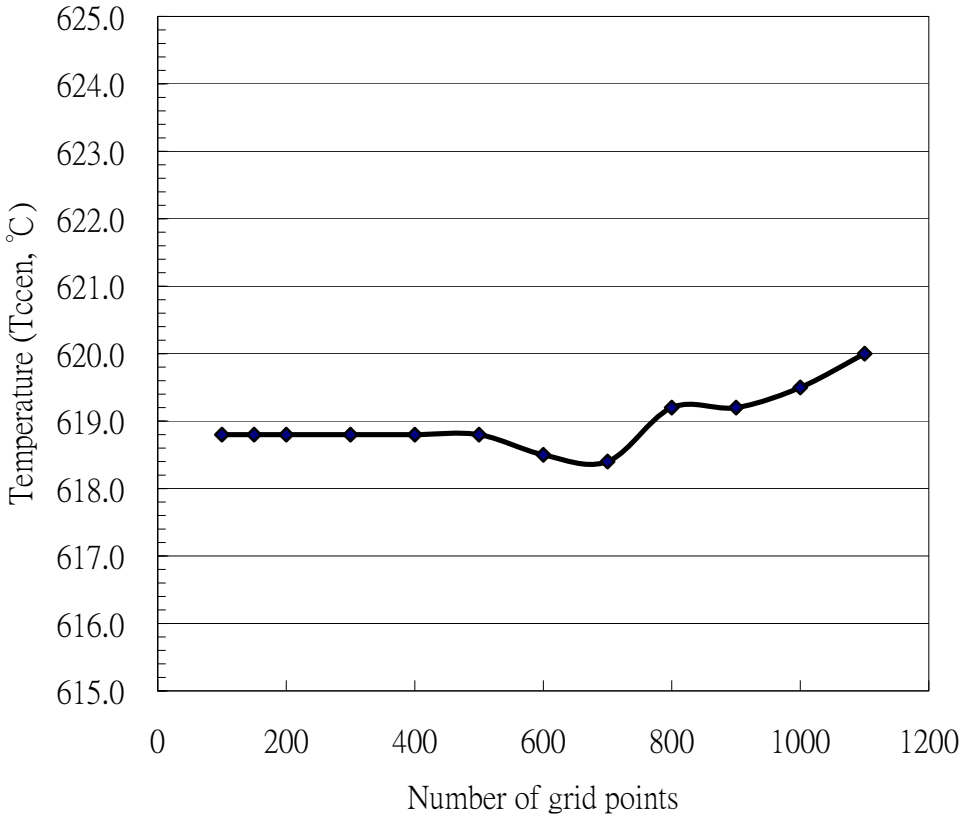

Fig 2.5. Cell temperature at the central point versus grid numbers in numerical program.

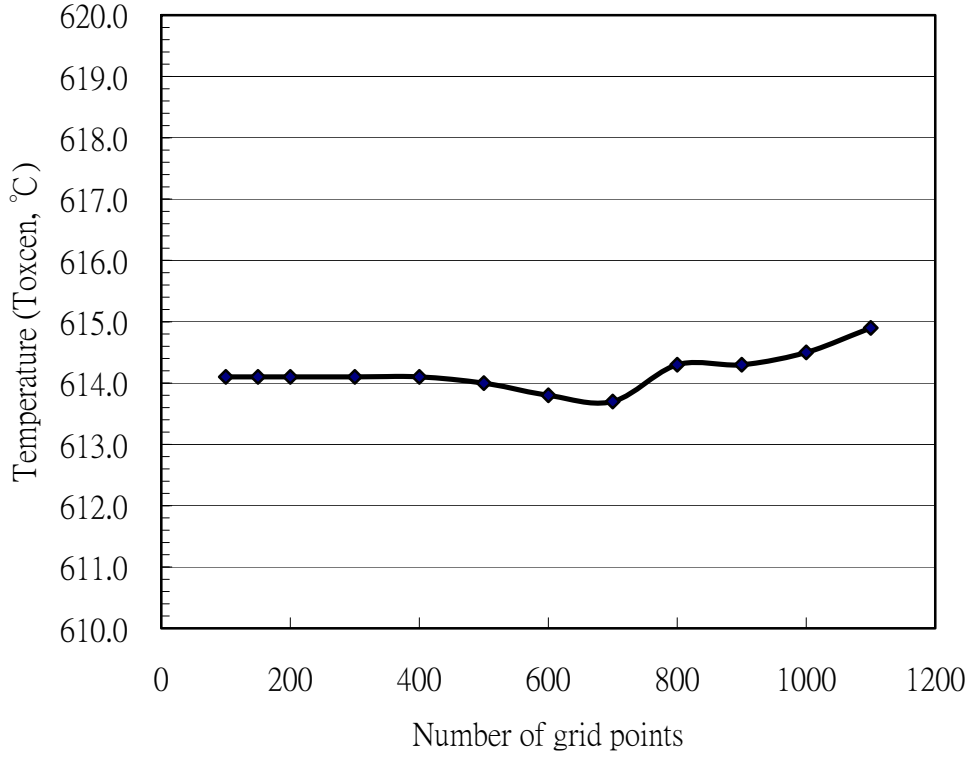

Fig 2.6. Cathode gas temperature at the central point versus grid numbers in numerical program.

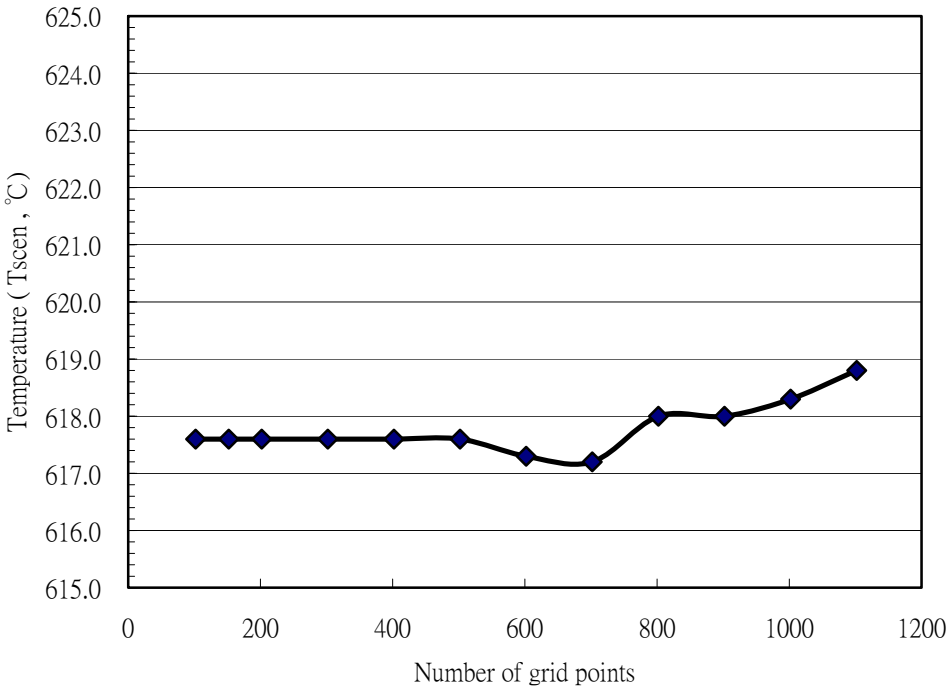

Fig 2.7. Separator temperature at the central point versus grid numbers in numerical program.

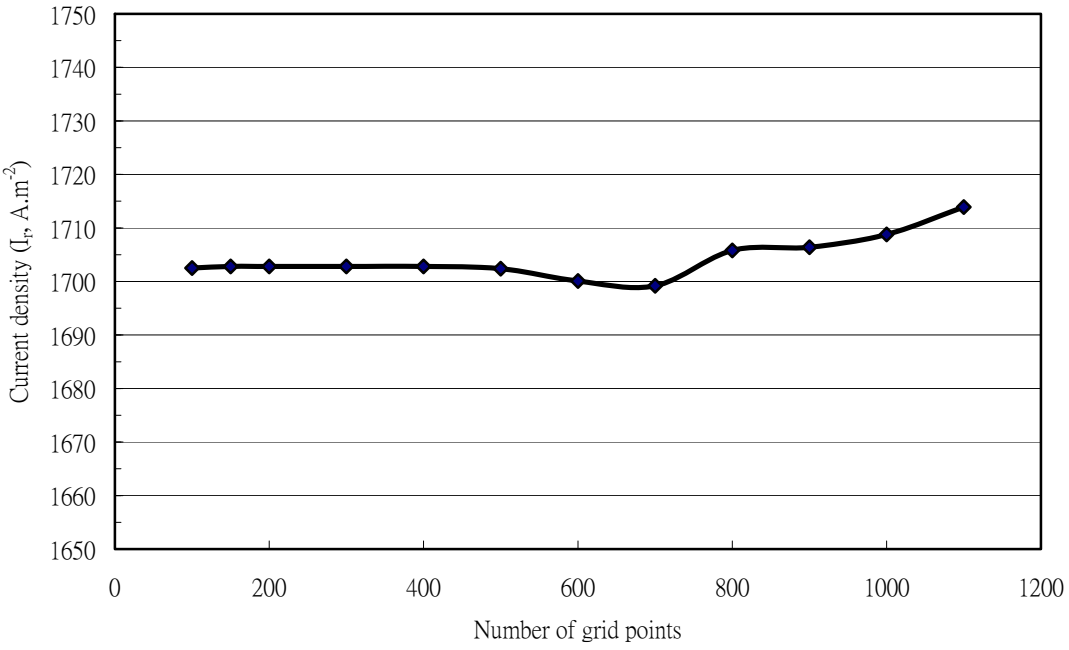

Fig 2.8. Current density at the central point versus grid numbers in numerical program.

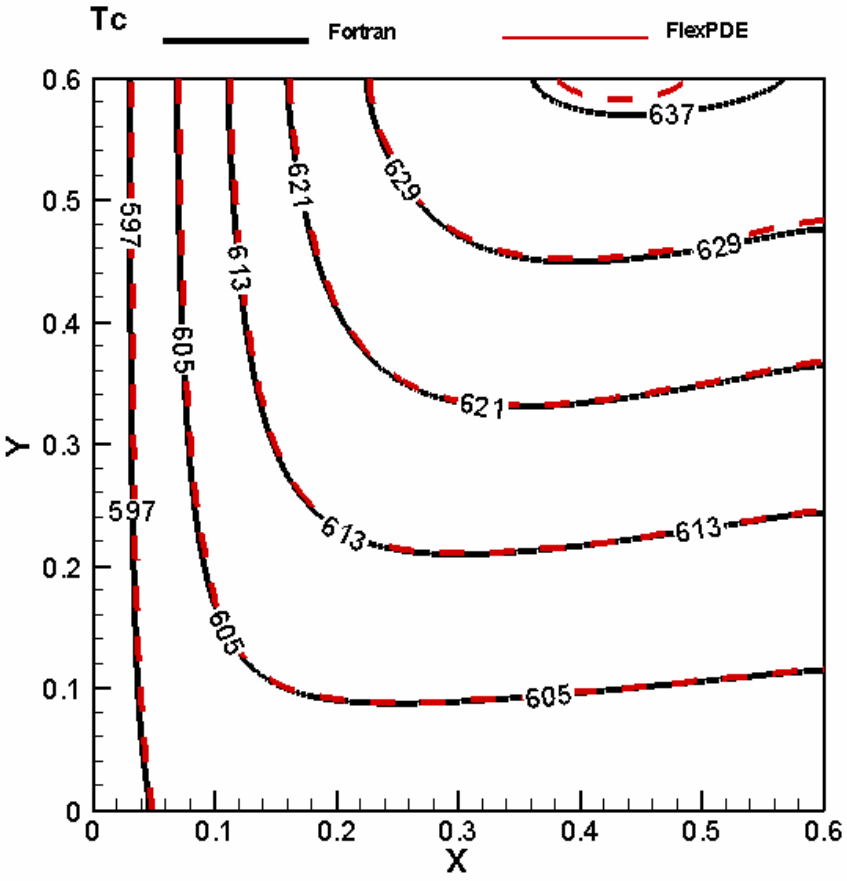

Fig 2.9. Cell temperature distribution calculated by the numerical method in Chapter 2 and FlexPDE software with uniform inlet flow rate

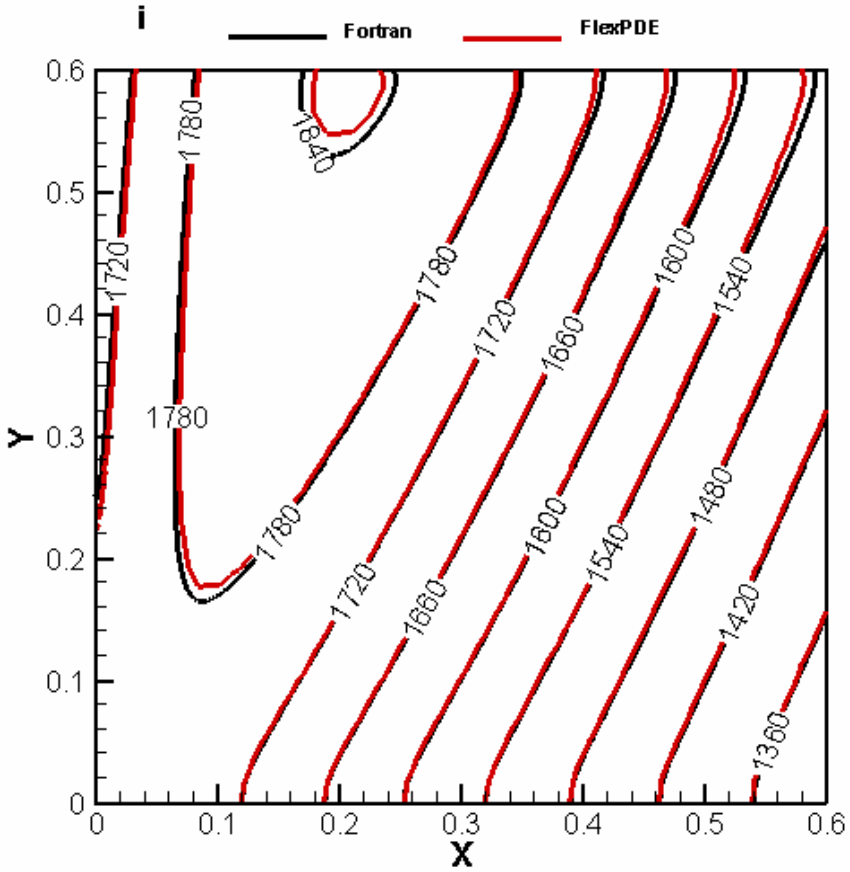

Fig 2.10. Current density distribution calculated by the numerical method in Chapter 2 and FlexPDE software with uniform inlet flow rate

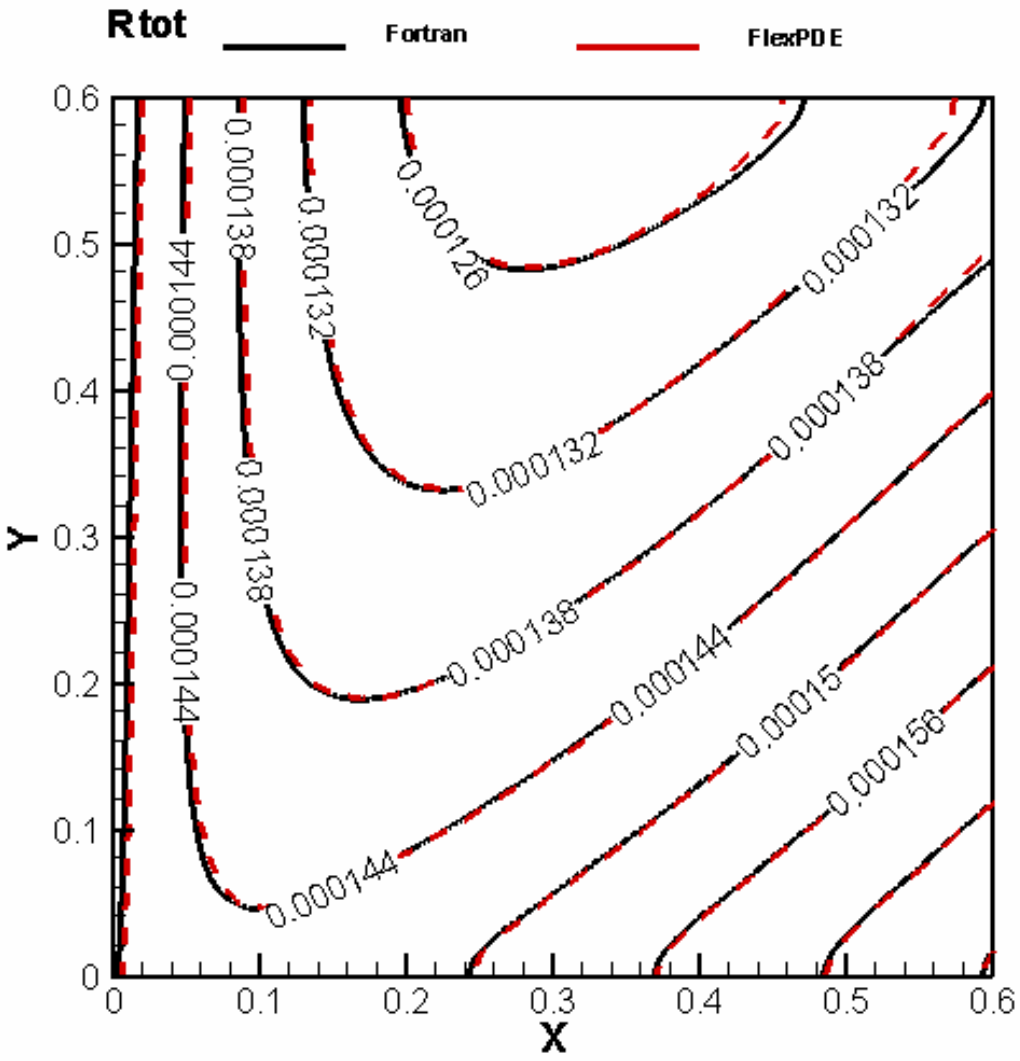

Fig 2.11. Total Resistance distribution on the cell plane with uniform inlet flow

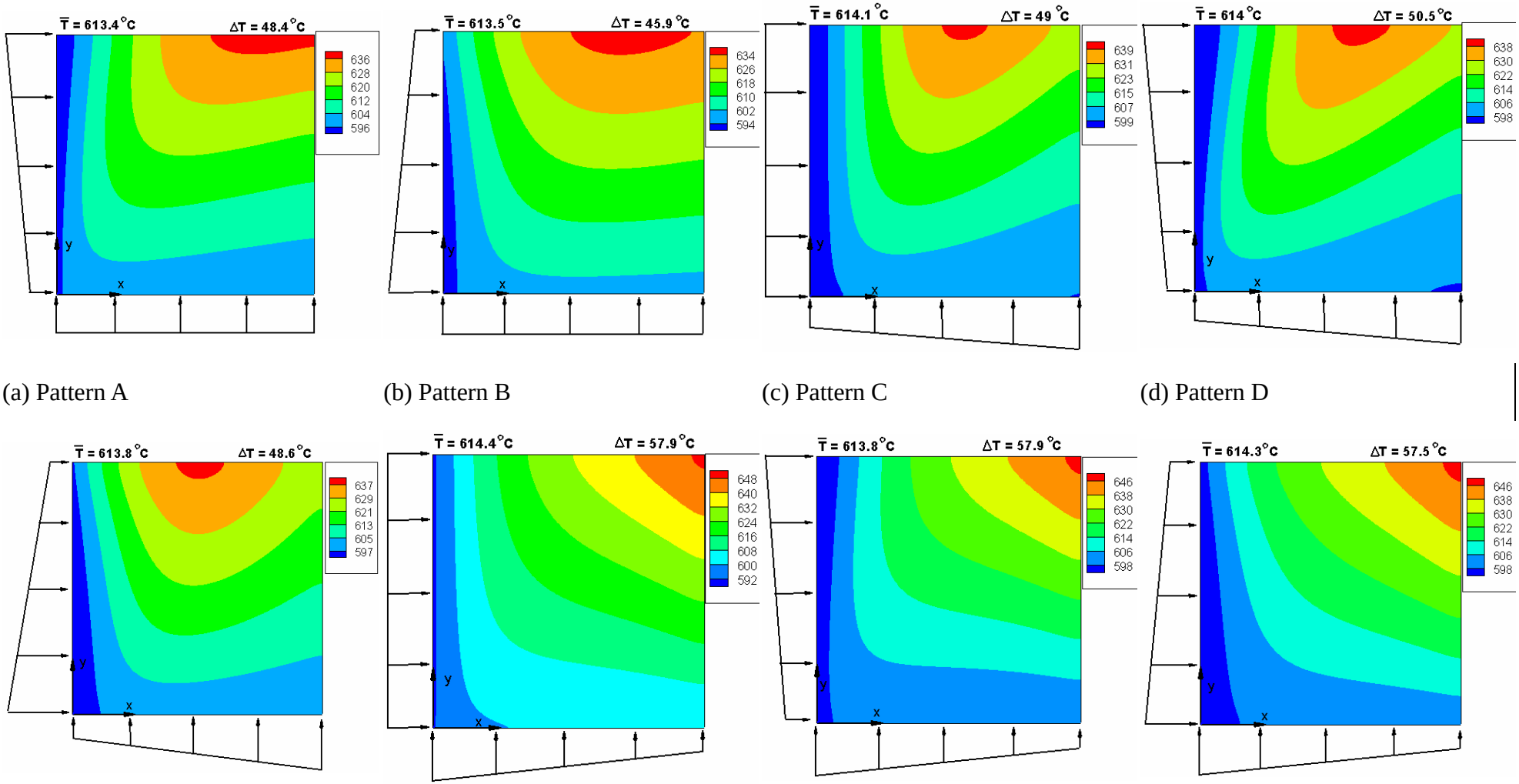

(a) Pattern A (b) Pattern B (c) Pattern C (d) Pattern D

(e) Pattern E (f) Pattern F (g) Pattern G (h) Pattern H

Fig 2.12. Cell temperature distribution of eight non-uniform patterns with deviation of 0.5

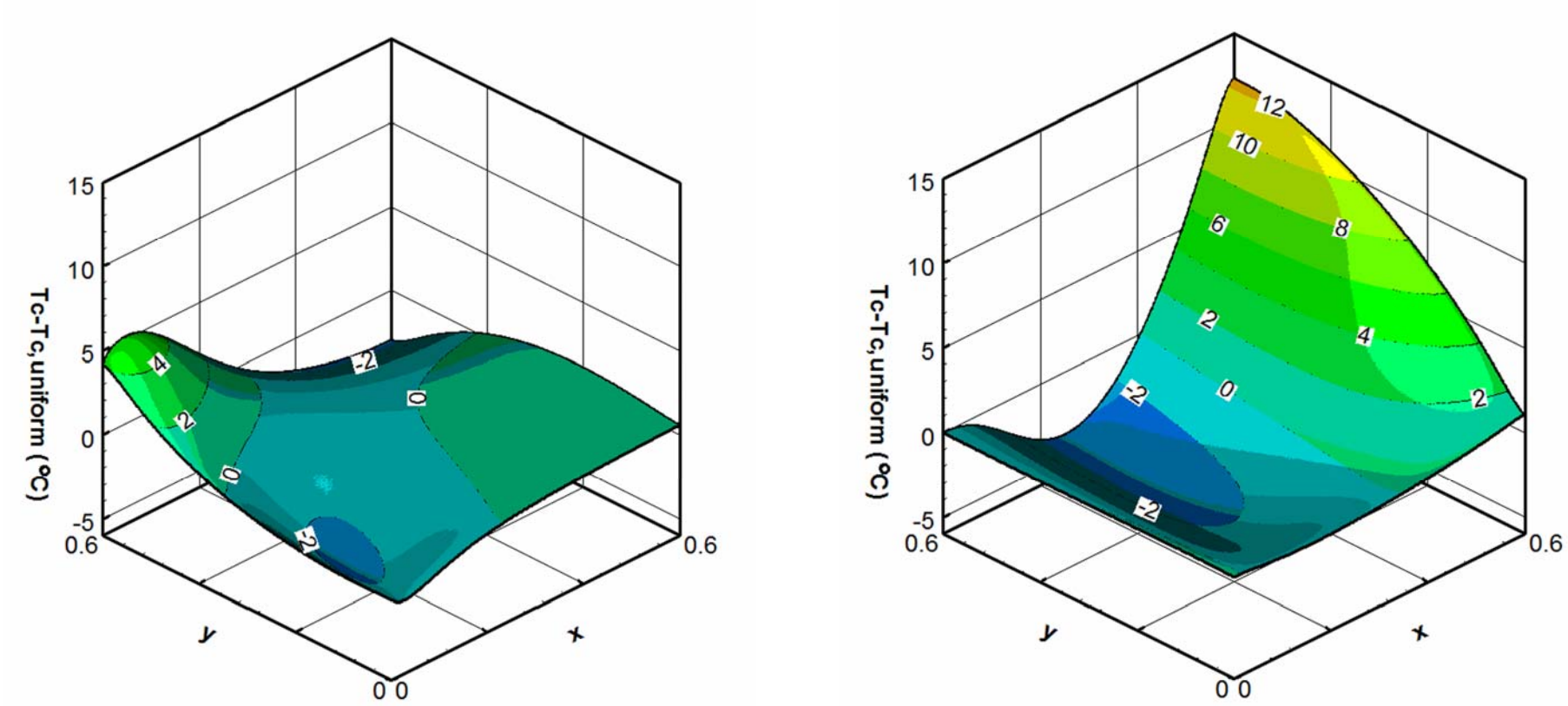

(a) Pattern B

(b) Pattern F

Fig 2.13. Temperature difference related to uniform pattern on the cell plane

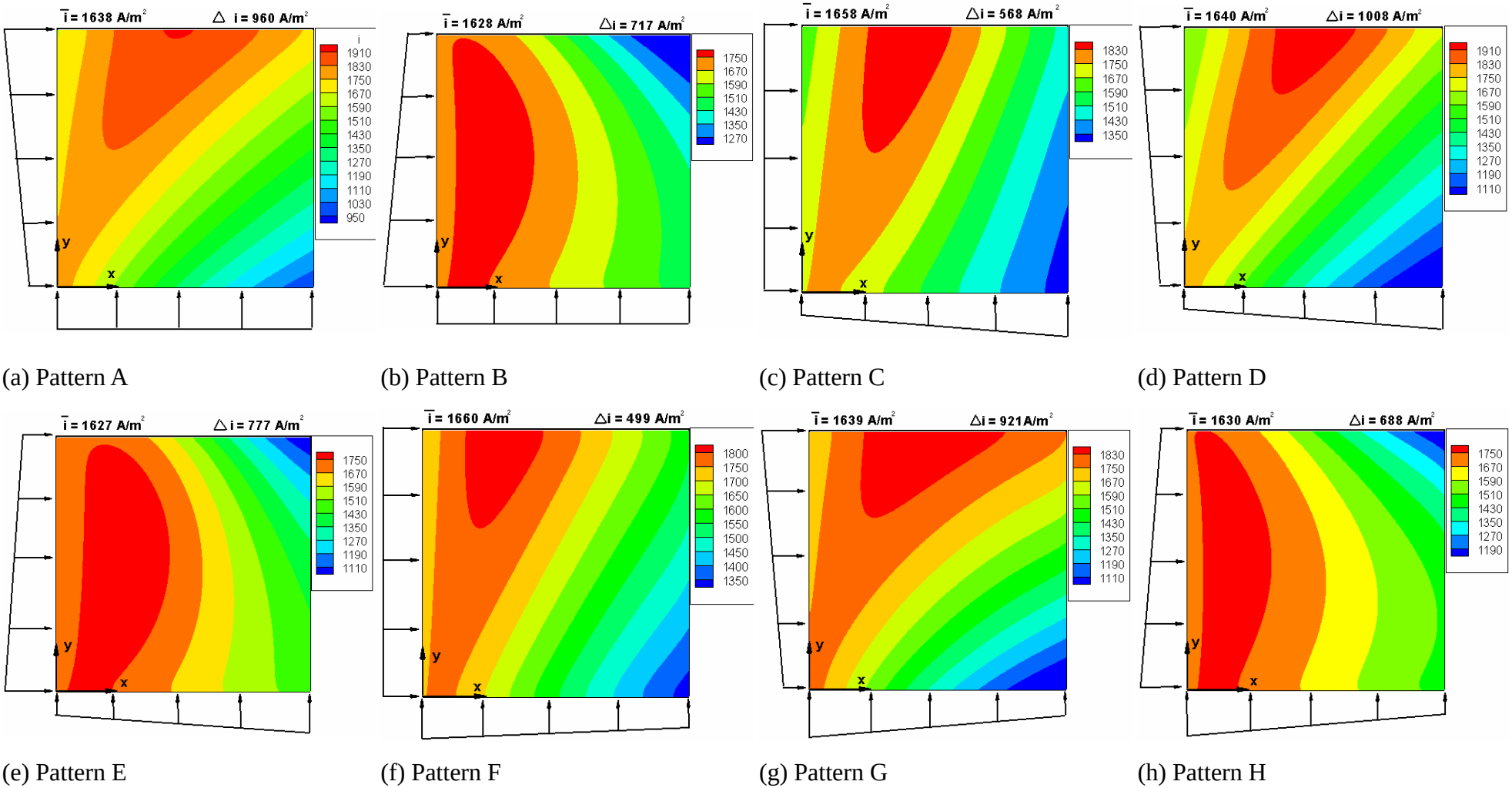

Fig 2.14. Current density distribution of eight non-uniform patterns with deviation of 0.5

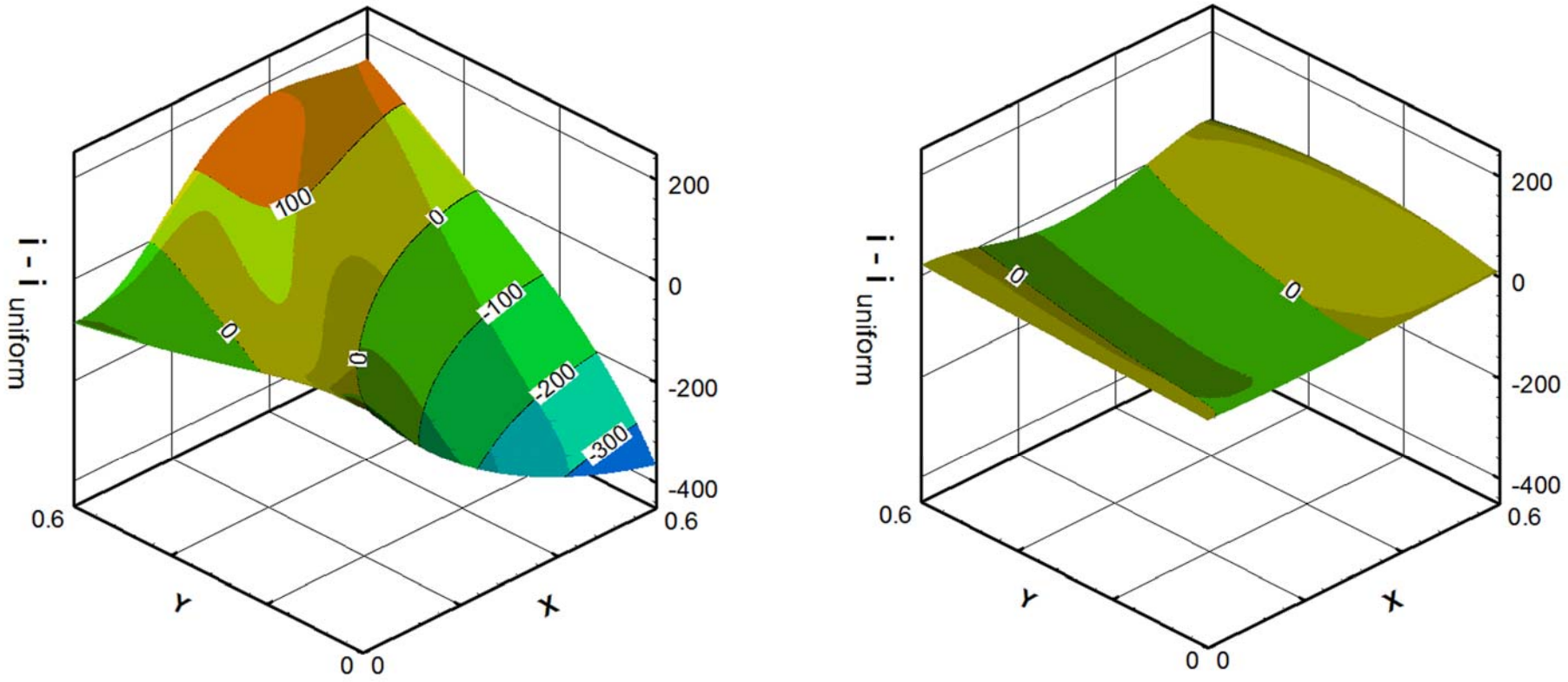

(a) Pattern D

(b) Pattern F

Fig 2.15. Current density difference related to uniform pattern on the cell plane

$\frac{\overline{T}_c - \overline{T}_{c,uniform}}{\overline{T}_{c,uniform}}$

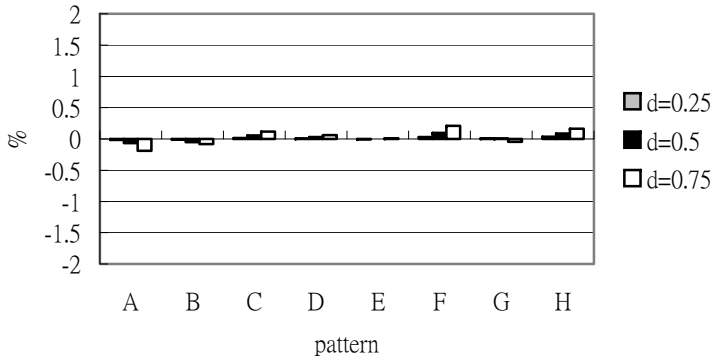

(a) average cell temperature

$\frac{\overline{i}_c - \overline{i}_{c,uniform}}{\overline{i}_{c,uniform}}$

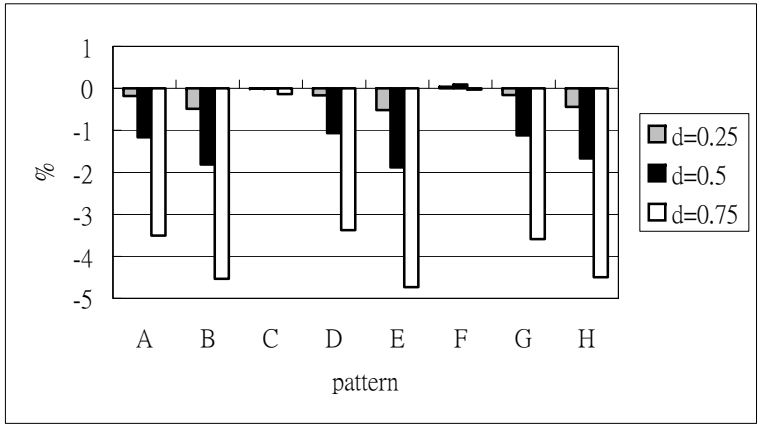

(b) average current density

$\frac{\Delta T_c - \Delta T_{c,uniform}}{\Delta T_{c,uniform}}$

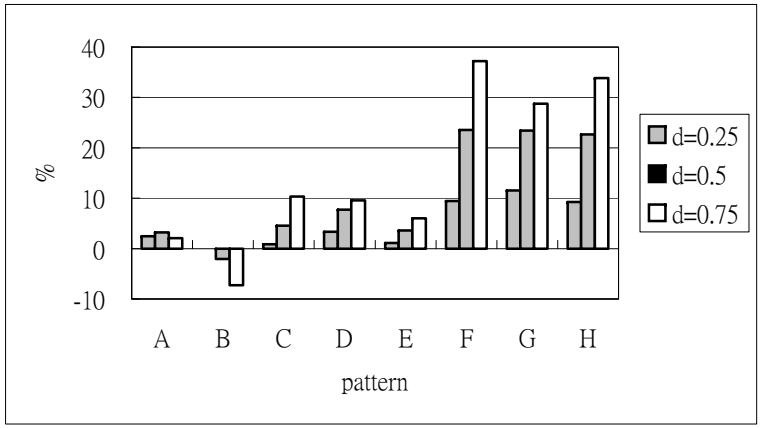

(c) cell temperature difference

$\frac{\Delta i_c - \Delta i_{c,uniform}}{\Delta i_{c,uniform}}$

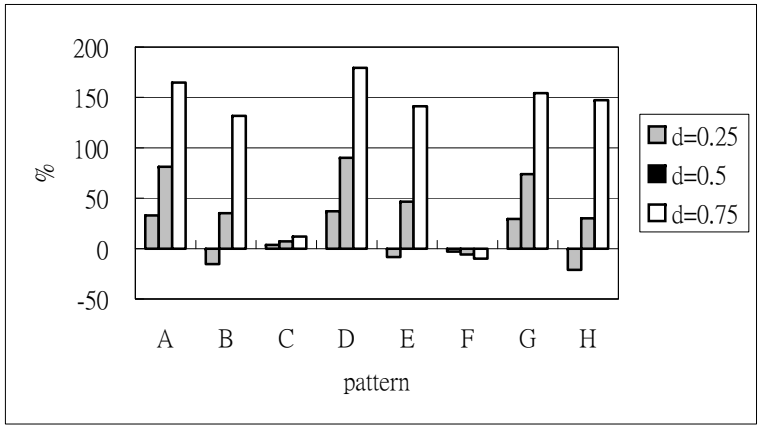

(d) current density difference

Fig 2.16. Relative variation of T_c and I_r at different non-uniform inlet flow patterns related to at uniform inlet flow patter

3. Current Density Analysis in a MCFC Unit with Non-uniform Inlet Flow and High Anode Gas Utilization

In the previous chapters, the cell performance of a MCFC subjected to a non-uniform inlet flow conditions in a cell unit and a stack is explored. It is clear that the distributions of current density and temperature are all influenced by the existence of the un-even reactant supply. However, the electrochemical reaction in the catalyst layer is also affected by the utilization of the reactant. That is, when discussing the effect of non-uniform inlet flow, the gas utilization is an important factor, because it represents an economical operation of a fuel cell when the anode gas utilization is higher. Examining the previous literature indicates that the anode gas utilization is over 70%, and in Chapter 2, we considered the anode gas utilization only up to 25%. Therefore, this chapter plans to extend previous research to the current density distribution analysis of a molten carbonate fuel cell when both the anode gas inlet flow is non-uniform and the anode gas utilization gets higher. Because the anode gas molar flow rate dominantly affects the current density of a fuel cell, the non-uniform inlet flow effect must induce an appearance of non-reaction on the cell plane when the anode gas utilization gets higher. This non-reaction area will also decrease the overall current density of a cell and deteriorate the electrical performance of a molten carbonate fuel cell.

3.1. Physical Model Description

This study investigates a 0.6m×0.6m molten carbonate anode gas cell unit with anode gas and cathode gas cross-flow, as shown in Figure 3-1. The anode gas flows in the x direction, and the cathode gas flows in the y direction. Additionally, this study combines the anode, electrolyte, and cathode to form a unit cell for simple analysis. Due to separator ribs, both flows are considered to unmixed flow, i.e., each flow is composed of many flow tubes parallel to each other. Manifold position will induce different mal-distribution profiles in the inlet section, as mentioned above. According to the results in Chapter 2, the anode gas and cathode gas molar flow rate dominantly affects the current density and the cell temperature, respectively. For simplifying the current density analysis, this chapter considers the cathode gas inlet is uniform and the anode gas inlet has three profiles, as shown in Figure 3-2. Before formulating the governing equations, this study assumes:

18. Steady state.

19. The gas flow in the anode channel and the cathode channel are treated as a plug-flow.

20. Inlet temperature and mole fractions of species in anode gas and cathode gas are constant and uniform.

21. Thermal properties of anode gas, cathode gas, cell, and separator are constant except for anode gas and cathode gas specific heat capacities.

22. Cell and separator boundary are adiabatic.

23. Neglect z direction change.

24. Separator cross-section geometry is unchanged throughout the x-y plane.

25. Cell voltage is uniform over the x-y plane.

26. Neglect the anode gas water-shift reaction.

This study considers the reformed methane or ethanol in the external reformer and the reforming gases are fed into the MCFC. The anode oxidation reactions are as follows.

$$H_2 + CO_3^{2-} \rightarrow H_2O + CO_2 + 2e^- \tag{3.1}$$

The reaction in cathode is

$$O_2 + 2CO_2 + 4e^- \rightarrow 2CO_3^{2-} \tag{3.2}$$

Mass balances are formulated for each species molar flow rate change in anode gas and cathode gas with species consumption linking the local current density.

$$\frac{1}{L_y}\frac{dn_{ag,k}}{dx} = \pm\frac{i}{n_e F} \tag{3.3}$$

$$\frac{1}{L_x}\frac{dn_{cg,k}}{dy} = \pm\frac{i}{n_e F} \tag{3.4}$$

Meanwhile, n is the molar flow rate of the k-component, n_e is the number of electrons transferred in the reactions of the anode and the cathode, and the plus/minus

symbol represents molar flow rate increase or decrease dependent on reactant or product species. In Eq. (3.3), anode gas reactants and products include hydrogen, carbon dioxide, and water. The reactant and product in cathode gas include oxygen and carbon dioxide in Eq. (3.4).

This research conserves energy for anode gas, cathode gas, cell, and separator, respectively.

For the gas in the anode flow channel,

$$\frac{\partial}{\partial x}\left(\sum n_{ag,k}c_{p,k}T_{ag}\right)=(ha)_{s-ag}\left(T_s-T_{ag}\right)+(ha)_{c-ag}\left(T_c-T_{ag}\right)+\frac{i}{2F}c_{p,CO_3^{2-}}T_c \tag{3.5}$$

For the gas in the cathode flow channel,

$$\frac{\partial}{\partial y}\left(\sum n_{cg,k}c_{p,k}T_{cg}\right)=(ha)_{s-cg}\left(T_s-T_{cg}\right)+(ha)_{c-cg}\left(T_c-T_{cg}\right)-\frac{i}{2F}c_{p,CO_3^{2-}}T_{cg} \tag{3.6}$$

For cell,

$$\begin{aligned}&(k\delta)_c\frac{\partial^2T_c}{\partial x^2}+(k\delta)_c\frac{\partial^2T_c}{\partial y^2}+(ka)_{c-s}\frac{\left(T_s-T_c\right)}{\delta_{c-s}}+(ha)_{c-ag}\left(T_{ag}-T_c\right)\\&+(ha)_{c-cg}\left(T_{cg}-T_c\right)+\frac{i}{2F}c_{p,CO_3^{2-}}\left(T_{cg}-T_c\right)+q_o=0\end{aligned} \tag{3.7}$$

For separator,

$$\begin{aligned}&(k\delta)_s\frac{\partial^2T_s}{\partial x^2}+(k\delta)_s\frac{\partial^2T_s}{\partial y^2}+(ka)_{c-s}\frac{\left(T_c-T_s\right)}{\delta_{c-s}}\\&+(ha)_{s-ag}\left(T_{ag}-T_s\right)+(ha)_{s-cg}\left(T_{cg}-T_s\right)=0\end{aligned} \tag{3.8}$$

Each gas species specific heat capacities in anode gas and cathode gas are a function of temperature based on the results of Koh et al [16], and this study adds one

carbon and one and half of oxygen specific heat capacity as carbonate ion specific heat capacity. In Eq. (3.7), q_0 is heat generation occurring in the cell unit due to electrochemical reactions and cell internal losses, and this heat generation occurs over the x-y plane as follows.

$$q_0 = -\Delta H \times \frac{i}{2F} - V \cdot i \tag{3.9}$$

$$\Delta H = -240506 - 7.3835 T_c \tag{3.10}$$

Meanwhile, ΔH is enthalpy change per mole of chemical reaction, calculated as a temperature function. In Eq. (3.7) and (3.8), k is thermal conductivity due to contact resistance between cell and separator in the z direction, and its value is set to 1.0 W/m K. In Eqs. (3.3)-(3.6), this chapter considers the non-uniform profile of the molar flow rate of the anode gas as follows.

$$n_{ag}(0, y) = \frac{N_{ag}}{L_y}\left(\frac{2d}{L_y} y + 1 - d\right) \tag{3.11}$$

Based on the Nernst equation, this study calculates the Nernst voltage as follows.

$$E = E_0 + \frac{RT}{2F} \ln\left(\frac{P_{H_2} P_{O_2}^{0.5} P_{CO_2,cg}}{P_{H_2O} P_{CO_2,ag}}\right) \tag{3.12}$$

$$E_0 = 1.2723 - 2.7654 \times 10^{-4} T \tag{3.13}$$

Meanwhile, E_0 is the reversible voltage under standard conditions, according to Koh et al. [15]. According to the results in Bosio et al.[30] , this study uses the total cell resistance, including that due to cathode polarization, the electrolyte tile

contribution, and the Ohmic resistance of the contacts. Note that this total cell resistance did not include the concentration polarization, because Bosio et al. [30] assumed the diffusion is non-limiting in the electrode. The cell voltage is the Nernst voltage minus the over-potentials, as follows.

$$V = E - iR_{tot} \tag{3.14}$$

$$R_{tot} = \frac{Ae^{B/T}}{\prod_i p_i^{\beta_i}} + c_{ir} + D \cdot e^{F/T} \tag{3.15}$$

where the parameters are $\beta^{O_2} = 0.67$, $A = 1.38 \times 10^{-7} \Omega m^2 Pa^{0.67}$, B=11400K, $c_{ir} = 0.348 \times 10^{-4} \Omega m^2$, $D = 4.8 \times 10^{-8} \Omega m^2$ and F=6596K [30].

The above simultaneous equations of the MCFC contain seven unknown variables, which are mole flow rate of each species ($n_{ag,k}$ and $n_{cg,k}$), anode gas temperature (T_{ag}), cathode gas temperature (T_{cg}), cell temperature (T_c), separator temperature (T_s), current density (i), and cell voltage (V). The mass equations are used to determine mole flow rate of each species, and energy equations are used to determine the temperatures. Nevertheless, in Eq. (3.14), both current density and cell voltage variables must be evaluated. Therefore, this study assumes that the cell voltage is uniform over the reaction area of the cell and then calculates the current density using Eq.(3.14). This chapter employs a software package, FlexPDE, to solve the governing equations, because it flexibly solves partial differential equations by a finite element method. The validation of this software package had done in

previous chapter.

3.2. Method of Solution

The above simultaneous equations of the MCFC contain seven unknown variables, which are mole flow rate of each species ($n_{ag,k}$ and $n_{cg,k}$), anode gas temperature (T_{ag}), cathode gas temperature (T_{cg}), cell temperature (T_c), separator temperature (T_s), current density (i), and cell voltage (V). The mass equations are used to determine mole flow rate of each species, and energy equations are used to determine the temperatures. Nevertheless, in Eq. (3.14), both current density and cell voltage variables must be evaluated. Therefore, this study assumes that the cell voltage is uniform over the reaction area of the cell and then calculates the current density using Eq.(3.14). This dissertation employs a software package, FlexPDE, to solve the governing equations, because it flexibly solves partial differential equations by a finite element method. The validation of this software package had done in Chapter 2, and the code of FlexPDE is listed in Appendix A.

In Appendix A, the SELECT section is the definitions about convergent criteria and grid generation function. The VARIABLES section sets the unknown variable in this study, which includes the mole flow rate of each species in anode and cathode gas, and the temperature of anode gas, cathode gas, cell, and separator. The DEFINITIONS section sets all parameters in this study, which are geometry parameter, thermal properties of each species, the Nernst equation, the total resistance

in the cell, reaction heat, and current density. The INITIAL VALUES section is the setting of initial conditions of each variable, and the EQUATIONS section describes the differential equations from Eq. (3.3) to (3.8) in this study. The BOUNDARIES section lists all boundary conditions in four sides of the calculation domain. The MONITORS and PLOTS section can show out the calculating results with color diagram in calculating process and ending, respectively.

3.3. Results and Discussion

This study considers the anode gas flow rate is 0.00621-0.0621 mol/s, the cathode gas flow rate is 0.0263-0.1841 mol/s, the inlet temperature of anode gas and cathode gas are 858K and 867 K, the operation pressure is 3.5 atm, the operation voltage is 0.8 V, and the deviation of the non-uniform profile is 0.5. Figure 3-3 shows that the current density distribution in pattern A and pattern B when the anode gas and cathode gas flow rate is $0.0621\,mol/s$ and 0.1841 mol/s, respectively. In this figure, the profile with bold line is the current density distribution in uniform pattern, and the profile with color represents current density distribution in pattern A or pattern B. Examining the current density distribution in uniform pattern indicates that the current density mainly decreases along the anode gas flow direction from $1842\,A\cdot m^{-2}$ to 1315 $A\cdot m^{-2}$. In the cathode gas flow direction, the current density slightly rises because of the decrease of total resistance in Eq.(3.15). In Fig. 3-3(a), the current density has more severe reduction in the corner of the anode gas exit and

the cathode gas inlet. In this corner, the hydrogen concentration becomes lower because the progressively increasing anode gas profile induces less anode gas flowing through this area. Oppositely, the area with apparent current drop happens in the corner of the anode gas exit and the cathode gas exit, because the anode gas non-uniform profile is progressively decreasing. Comparing the Fig. 3-3(a) and 3-3(b) indicates that the current density drop in the corner of Fig. 3-3(b) is slightly larger than that of Fig. 3-3(a).

Figure 3-4 shows that the current density distribution in pattern A and pattern B when the anode gas and cathode gas flow rate is $0.01242\,mol/s$ and $0.0526\ mol/s$, respectively. In this figure, the profile with bold line is the current density distribution in uniform pattern, and the profile with color represents current density distribution in pattern A or pattern B. Examining the current density distribution in uniform pattern indicates that the current density mainly decreases along the anode gas flow direction from $1846\,A\cdot m^{-2}$ to $347\ A\cdot m^{-2}$. This current density range is clearly lower than that in Fig. 3-3. Because both the anode gas and cathode gas molar flow rate reduces in Fig. 3-4, the current density becomes lower due to the less hydrogen and oxygen concentration. In Fig. 3-4(a), the current density has a reduction in the corner of the anode gas exit and the cathode gas inlet. In this corner, the current density rapidly decreases from $1848\,A\cdot m^{-2}$ to $138\ A\cdot m^{-2}$. This means the region is close to a non-reaction area. The less anode gas flow rate and non-uniform inlet flow induces the anode gas molar flow rate is fewer in this area, so

the hydrogen is almost used up and the current density becomes near zero. Similarly, the current density severely drops in the corner of the anode gas exit and the cathode gas exit in Fig. 3-4(b), and this corner occur the non-reaction situation.

Figure 3-5 shows that the current density distribution in pattern A and pattern B when the anode gas and cathode gas flow rate is $0.00621\,mol/s$ and $0.0263\ mol/s$, respectively. The non-reaction area of Fig. 3-5(a) is apparently larger than the same area of Fig. 3-4(a), because the anode gas molar flow rate is the least in this study. Even in uniform pattern, the current density distribution happen a severe drop in the anode gas exit, as shown in the bold line. This means the anode gas is almost used up when the anode gas flows out the cell reaction in uniform pattern. Examining the average current density over the reaction area shows that it is the lowest one in Figs. 3-3 to 3-5. When the inlet flow is non-uniform, the current density in the corner of the anode gas exit of Fig. 3-5(a) and 3-5(b) drops to zero because of the progressively increasing and decreasing profile of the anode gas inlet molar flow rate.

Promoting the anode gas utilization in an anode gas cell is more economical, but the global current density will drop with an increase in anode gas consumption and decrease the power of a anode gas cell. Moreover, the non-reaction area will happen and more deteriorate the global current density when the anode gas inlet molar flow rate becomes less and the non-uniform inlet profile is considered. Table 3-1 lists the average current density and anode gas utilization in all cases of this study. In this

table, it is clear that the average current density and anode gas utilization decreases and increases with a decrease in the molar flow rate, respectively. Furthermore, Pattern B has the lowest average current density and anode gas utilization when the molar flow rate is unchanged, because the happening of non-reaction area in the corner of the anode gas exit and the cathode gas exit. Figure 3-6 depict the histogram of relative change of average current density in non-uniform pattern related to that in uniform pattern. In this figure, the relative change is below –2% when the anode gas molar flow rate is 0.0621 and 0.00621 mol/s, and the anode gas utilization is near 30% and 90%, respectively. The minus represents the average current density becomes lower when the inlet profile is non-uniform. Once the anode gas molar flow rate decreases, the anode gas utilization will increase accompanying the flow rate decrease. The effect of non-uniform inlet flow on the average current density becomes more apparent when the anode gas utilization is close to 73%, and then becomes slighter along the increase of gas utilization. In this figure, the relative change of average current density raise to –4% in Pattern B.

3.4. Conclusions

This study investigates the effect of non-uniform inlet flow on the electrical performance of a MCFC unit. This work employed a software package to solve the simultaneous mass, energy, and electrochemistry equations. With considering three flow patterns and three molar flow rates, this research analyzed the current density

distributions at different conditions. The results show that the anode gas utilization increases with a decrease in the molar flow rate, and the average current density decreases with the decrease in the molar flow rate. In addition, non-uniform Pattern A and B will induce a happening of non-reaction area in the corner of the anode gas exit. This non-reaction area deteriorates the average current density and deteriorates the electrical performance to –4% when the anode gas molar flow rate is $0.01242\,mol/s$ and anode gas utilization is 73%.

Table 3.1 Average current density and anode gas utilization at different inlet molar flow rate and patterns

	Uniform		PatternA		PatternB	
	i $\left(\frac{A}{m^2}\right)$	U_f (%)	i $\left(\frac{A}{m^2}\right)$	U_f (%)	i $\left(\frac{A}{m^2}\right)$	U_f (%)
n_f=0.0621 n_a=0.1841	1655	25	1636	25	1626	23
n_f=0.01242 n_a=0.0526	998	73	981	72	963	71
n_f=0.00621 n_a=0.0263	606	90	601	88	595	90

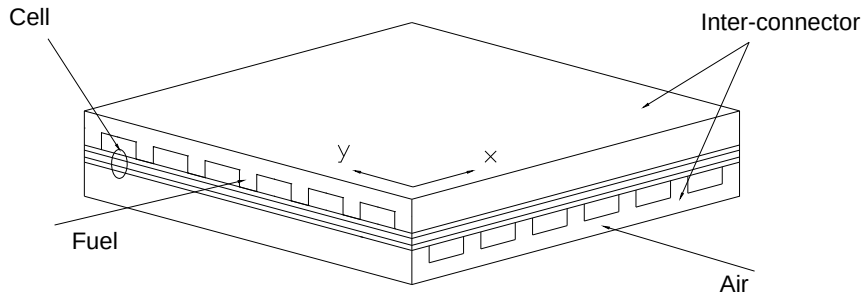

Fig 3.1. Schematic diagram of a unit of molten carbonate anode gas cell in cross-flow.

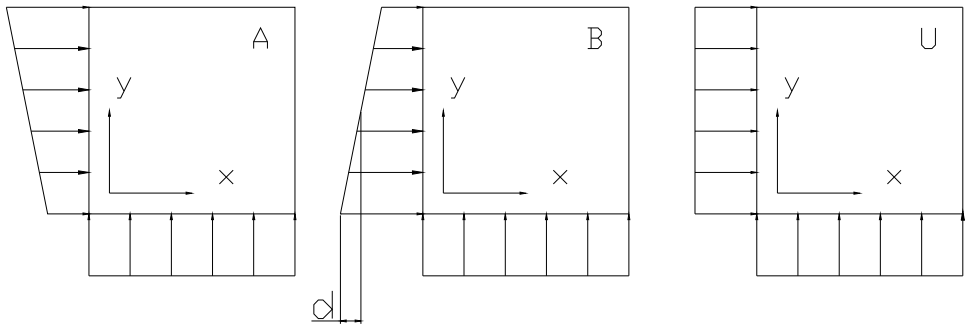

Fig 3.2. Arrangements of non-uniform inlet flow patterns in this chapter.

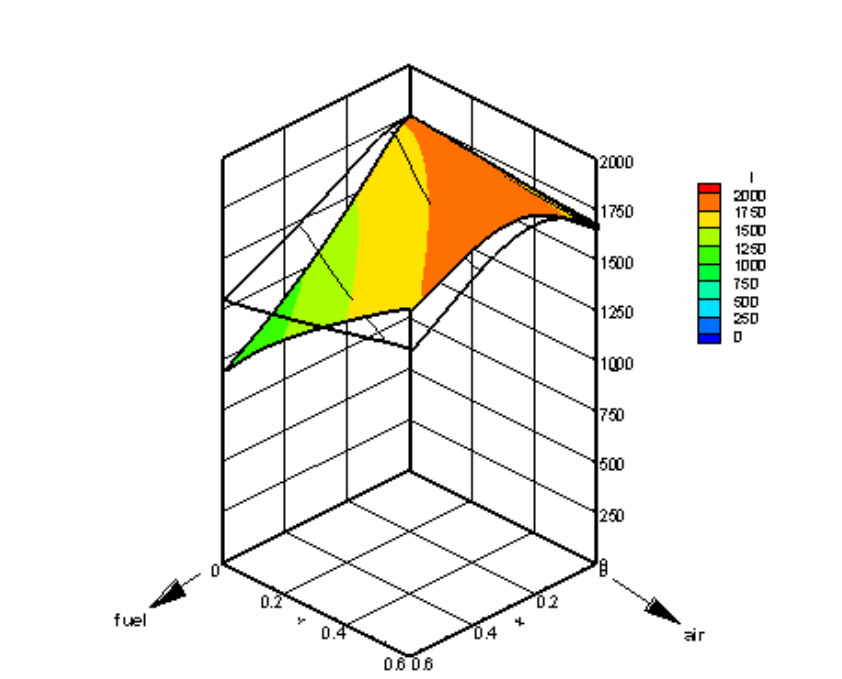

(a) Pattern A

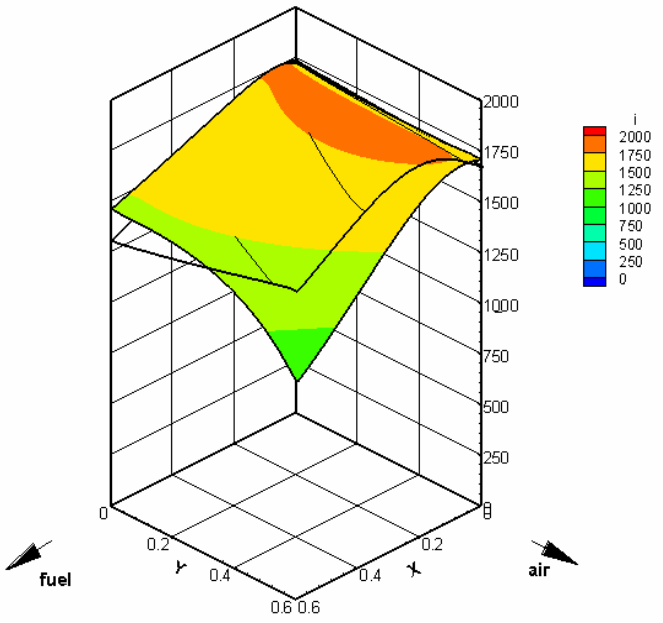

(b) Pattern B

Fig 3.3. Current density distribution in Pattern A and B when n_f =0.0621 and n_a =0.1841 mol/s.

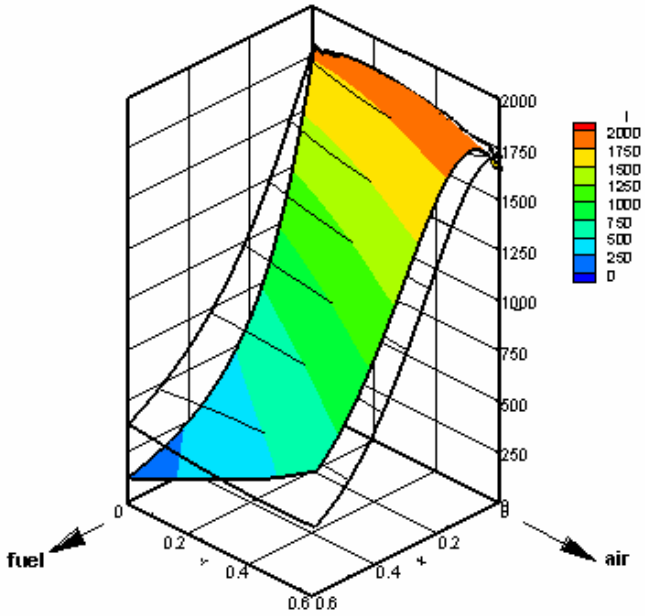

(a) Pattern A

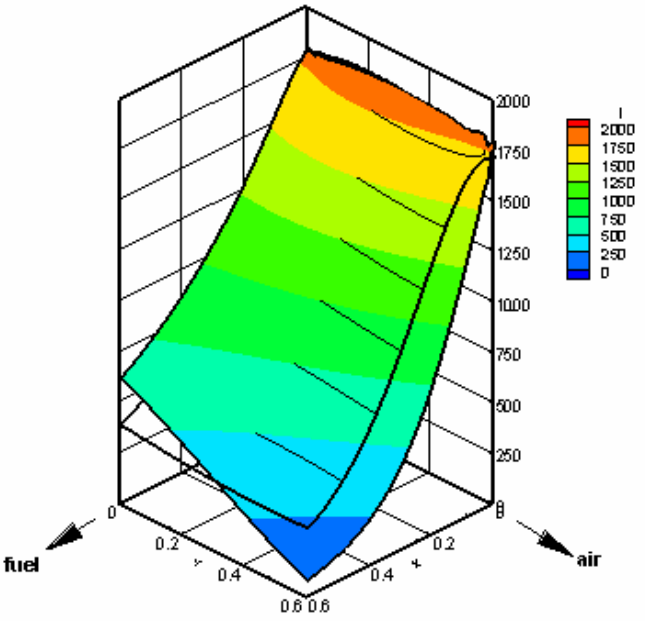

(b) Pattern B

Fig 3.4. Current density distribution in Pattern A and B when n_f =0.01242 and n_a =0.0526 mol/s

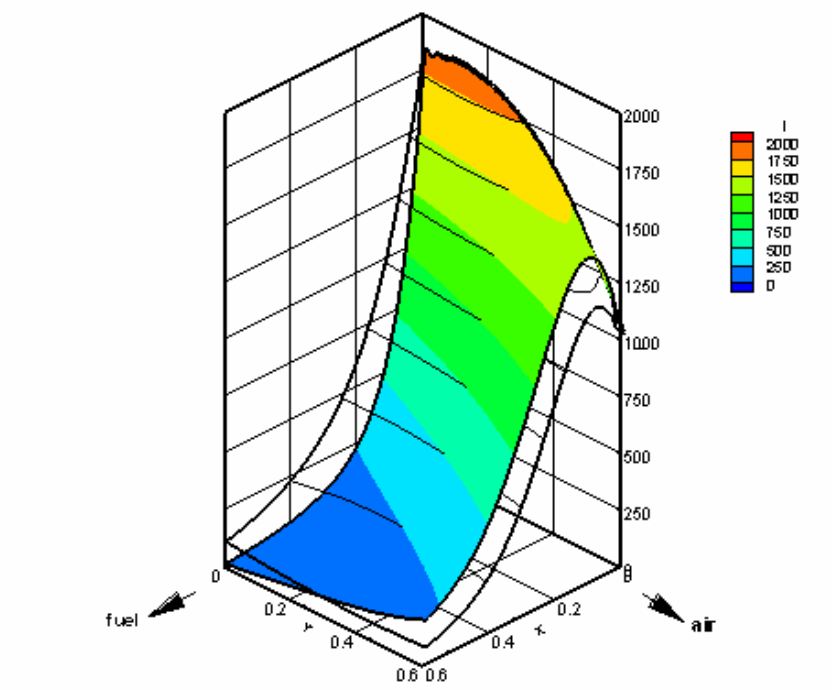

(a) Pattern A

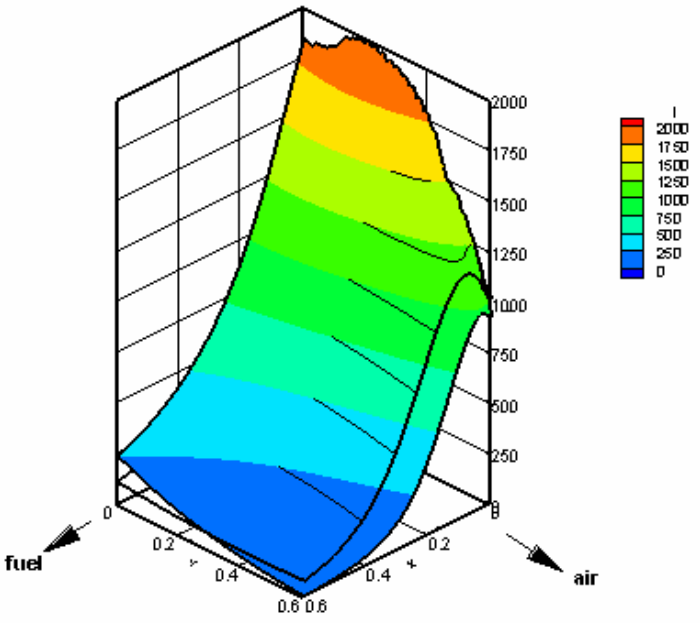

(b) Pattern B

Fig 3.5. Current density distribution in Pattern A and B when n_f =0.00621 and n_a =0.0263 mol/s.

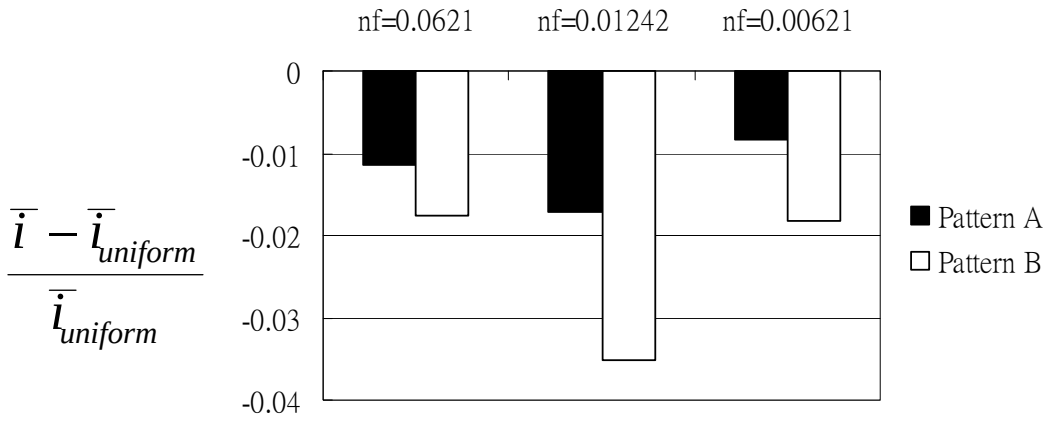

Fig 3.6. Relative change of average current density in non-uniform pattern.

4. Effect of Inlet Flow Maldistribution on the Thermal and Electrical Performance of an MCFC Stack

4.1. Physical Model Description

This chapter considers a MCFC stack with a stacking of ten cells. Because the features of a MCFC are strongly affected by the temperature, the temperature control for a MCFC stack is a necessary condition. Moreover, the performance promotion methods of a MCFC stack includes that increase of the reaction area and concentration of reactant, such that the transfer rate of the reactions to the reaction area and the exhaust rate of products are enhanced. This study simplifies the analysis of a MCFC stack to be a quasi-three dimensional physical model, because a three dimensional model wastes lots of calculation time and computer memory. In the arrangement of mal-distributed inlet flow in the stacking direction, this chapter considers four cases with different non-uniform inlet flow patterns. Figure 4.1 to Figure 4.4 shows the schematic diagrams of these four cases. Figure 3.1 depicts the case with uniform inlet flow rate of both anode gas and cathode in the stacking direction. Figure 4.2 shows that the inlet flow rate of anode gas is uniform, and the inlet flow rate of cathode gas is decreasing profile with a decrease in the layer number. Similarly, the inlet flow rate of anode gas is decreasing profile with a decrease in the layer number, and the inlet flow rate of cathode gas is uniform in Figure 4.3. Furthermore, Figure 4 shows that both the inlet flow rate of anode gas and cathode

gas are decreasing profile with a decrease in the layer number. Note that all these non-uniform profile has same deviation of 0.5 in these figures.

4.2. Basic Assumptions

The formulations of the governing equations are based on the following assumptions:

27. Steady state.
28. The gas flow in the anode channel and the cathode channel are treated as a plug-flow.
29. The inlet temperature and molar fractions of species in the anode gas and the cathode gas are constant and uniform.
30. The thermal properties of the anode gas, the cathode gas, the cell and the separator are constant, except for the specific heat capacities of the anode gas and the cathode gas.
31. The boundaries of the cell and separator are adiabatic.
32. The properties variations of each layer in the z direction are negligible.
33. The cross-sectional geometry of separator is unchanged throughout the x-y plane.
34. The water-shift reaction in the anode gas is negligible.

35. The cell voltage is uniform over the cell plane.

36. The top and bottom plate of the MCFC stack is adiabatic.

4.3. Governing Equations

4.3.1. Reaction Equations

This chapter considers a molten carbonate fuel cell unit with external reforming and the reforming reaction in the anode gas is neglected. The cathode gas is atmospheric air, and electricity is generated in the cell, including the anode, electrolyte, and cathode. Meanwhile, the porous matrix electrolyte contains migrating molten carbonate ions. Reactions in the anode and cathode are as follows.

$$H_2 + CO_3^{2-} \rightarrow H_2O + CO_2 + 2e^- \tag{4.1}$$

$$O_2 + 2CO_2 + 4e^- \rightarrow 2CO_3^{2-} \tag{4.2}$$

4.3.2. Mass Conservation Equations

Faraday's law describes the current density and gas molar flux relationship for species at the electrode surface. Therefore, mass balances of anode and cathode gases are as follows.

$$\left(\frac{1}{L_y} \frac{dn_{ag,k}}{dx} \right)^k = \left(\pm \frac{i}{n_e F} \right)^k \tag{4.3}$$

$$\left(\frac{1}{L_x} \frac{dn_{cg,k}}{dy} \right)^k = \left(\pm \frac{i}{n_e F} \right)^k \tag{4.4}$$

Here, n is the molar flow rate of the k-component, and n_e is the number of electrons transferred in anode and cathode reactions. The plus/minus symbol represents an increase/decrease in each species' molar flow rate caused by the anode and cathode chemical reaction. The symbol is positive for reactants, negative for anode and cathode products. The superscript k stands for the layer number.

4.3.3. Energy Conservation Equations

This work applies energy conservation for anode gas, cathode gas, the cell and separator for each layer, and uses heat transfer rate terms between adjacent layers to couple temperature interaction in the whole stack.

For the gas in the anode flow channel,

$$\frac{d}{dx}\left(\sum n_{ag,k} c_{p,k} T_{ag}\right)^k = \dot{q}_{conv,s^k-ag^k} + \dot{q}_{conv,c^k-ag^k} + \dot{q}_{mass,c^k-ag^k} \tag{4.5}$$

For the gas in the cathode flow channel,

$$\frac{d}{dy}\left(\sum n_{cg,k} c_{p,k} T_{cg}\right)^k = \dot{q}_{conv,s^{k-1}-cg^k} + \dot{q}_{conv,c^k-cg^k} - \dot{q}_{mass,cg^k-c^k} \tag{4.6}$$

For the cell,

$$\begin{aligned}(k\delta)_c \frac{\partial^2 T_c^k}{\partial x^2} + (k\delta)_c \frac{\partial^2 T_c^k}{\partial y^2} - \dot{q}_{cont,c^k-s^k} - \dot{q}_{cont,c^k-s^{k-1}} - \dot{q}_{conv,c^k-ag^k} \\ -\dot{q}_{conv,c^k-cg^k} + \dot{q}_{mass,cg^k-c^k} - \dot{q}_{mass,c^k-ag^k} + \dot{q}_{reac}^k = 0\end{aligned} \tag{4.7}$$

For the separator,

$$(k\delta)_s \frac{\partial^2 T_s^k}{\partial x^2} + (k\delta)_s \frac{\partial^2 T_s^k}{\partial y^2} + \dot{q}_{cont,c^k-s^k} + \dot{q}_{cont,c^{k+1}-s^k} - \dot{q}_{conv,s^k-ag^k} - \dot{q}_{conv,s^k-cg^{k+1}} = 0 \tag{4.8}$$

Meanwhile, heat transfer rate terms in Equations (4.5) to (4.8)are described in Table 4-1. Moreover, the $N_{ag}^{k}(=n_{ag}^{k}L_{y})$ and $N_{cg}^{k}(=n_{cg}^{k}L_{x})$ in each layer differ due to the mal-distributed molar flow rate in the stacking direction. This study considers the non-uniform molar flow rate as a stack number function as follows.

$$N_{ag}^{k}=\overline{N}_{ag}\left(\frac{2d_{stack,ag}^{k}}{\left(n_{stack}-1\right)}\left(k-1\right)+\left(1-d_{stack,ag}^{k}\right)\right) \tag{4.9}$$

$$N_{cg}^{k}=\overline{N}_{cg}\left(\frac{2d_{stack,cg}^{k}}{\left(n_{stack}-1\right)}\left(k-1\right)+\left(1-d_{stack,cg}^{k}\right)\right) \tag{4.10}$$

Here, $\overline{N}_{ag}$ and $\overline{N}_{cg}$ are the mean molar flow rate of the MCFC stack, n_{stack} is the amount of stacks, and stack deviation $d_{stack,ag}^{k}$ and $d_{stack,cg}^{k}$ represent the unilateral deviation of the non-uniform profile. This deviation is the flow rate variation ratio to the mean flow rate and its value may be positive and zero representing the progressively increasing profile and uniform profile, respectively.

4.3.4. Nernst Voltage and Polarizations

The Nernst voltage is calculated using the Nernst equation, as follows.

$$E=E_{0}+\frac{RT}{2F}\ln\left(\frac{P_{H_2}P_{O_2}^{0.5}P_{CO_2,cg}}{P_{H_2O}P_{CO_2,ag}}\right) \tag{4.11}$$

$$E_{0}=1.2723-2.7654\times10^{-4}T \tag{4.12}$$

Meanwhile, E_0 is the reversible voltage under standard conditions. The current work uses total cell resistance according to the results from Bosio et al. [30],

including cathode polarization, electrolyte tile contribution, and Ohmic resistance of contacts. This total cell resistance notably does not include polarization concentration, because Bosio et al. [30]assumes a non-limiting electrode diffusion. Cell voltage is the Nernst voltage minus the over-potentials, as follows.

$$V = E - iR_{tot} \tag{4.13}$$

$$R_{tot} = \frac{Ae^{B/T}}{\prod_i p_i^{\beta_i}} + c_{ir} + D \cdot e^{F/T} \tag{4.14}$$

where the parameters can be found in Bosio et al. [30]

The above simultaneous MCFC equations contain seven unknown variables, including molar flow rate of each species ($n_{ag,k}^k$ and $n_{cg,k}^k$), anode gas temperature (T_{ag}^k), cathode gas temperature (T_{cg}^k), cell temperature (T_c^k), separator temperature (T_s^k), current density (i^k), and cell voltage (V^k). The mass equations determine molar flow rate of each species, and energy equations determine temperatures. Both current density and cell voltage variables in Equation (4.13) must nevertheless be evaluated. Because most fuel cell stacks are in series connection between layers, this study assumes a constant current over the whole cell stack and then calculates cell voltage by the following equation integrating from Eq. (4.13).

$$V = \frac{\int_0^{L_x}\int_0^{L_y} \frac{E(x,y)}{R_{tot}(x,y)} dx \cdot dy - \mathrm{I}}{\int_0^{L_x}\int_0^{L_y} \frac{1}{R_{tot}(x,y)} dx \cdot dy} \tag{4.15}$$

4.4. Method of Solution

This study divides the calculation domain of the x-y plane into $N \times N$ subdivisions as shown in Fig. 2-3, and assigns the calculation nodes $n_{ag,k}^{k}$ and T_{ag}^{k} at the inlet and outlet of each subdivision in the x direction of anode gas flow. Similarly, the calculating nodes $n_{cg,k}^{k}$ and T_{cg}^{k} are assigned to the inlet and outlet of each subdivision in the y direction of the cathode gas flow. Furthermore, the calculation nodes i^{k}, T_{c}^{k}, and T_{s}^{k} are assigned to the center of the subdivision. Grid generation and the implicit scheme are adopted to discretize Equations (4.3) to (4.8) to finite difference equations, employing the TDMA (Tri-Diagonal Matrix Algorithm) to solve simultaneous algebraic equations.

The Eqs. (4.3) and (4.4) can be discretized to the following based on different species in anode and cathode side, respectively.

For the gas in the anode flow channel,

$$\left(n_{H_{2(i+1,j)}} = n_{H_{2(i,j)}} - \frac{i_{(i,j)} \cdot \Delta x}{2F} \right)^{k} \tag{4.16}$$

$$\left(n_{H_2O_{(i+1,j)}} = n_{H_2O_{(i,j)}} + \frac{i_{(i,j)} \cdot \Delta x}{2F} \right)^{k} \tag{4.17}$$

$$\left(n_{CO_{2(i+1,j)}} = n_{CO_{2(i,j)}} + \frac{i_{(i,j)} \cdot \Delta x}{2F} \right)^{k} \tag{4.18}$$

For the gas in the cathode flow channel,

$$\left(n_{CO_{2(i,j+1)}} = n_{CO_{2(i,j)}} - \frac{i_{(i,j)} \cdot \Delta y}{2F} \right)^k \tag{4.19}$$

$$\left(n_{O_{2(i+1,j)}} = n_{O_{2(i,j)}} - \frac{i_{(i,j)} \cdot \Delta y}{4F} \right)^k \tag{4.20}$$

The Eqn. (4.5) to (4.8) for energy conservation of anode gas, cathode gas, cell, and separator can be discretized to the following finite difference equations

For the gas in the anode flow channel,

$$\begin{aligned} &\left(\left(\frac{\sum \left(n \cdot c_p \right)_f}{\Delta x} \right) + \frac{h_f a_{cf}}{2} + \frac{h_f a_{sf}}{2} \right)^k_{(i+1,j)} T^k_{f(i+1,j)} = \\ &\left(\left(\frac{\sum \left(n \cdot c_p \right)_f}{\Delta x} \right) - \frac{h_f a_{cf}}{2} - \frac{h_f a_{sf}}{2} \right)^k_{(i,j)} T^k_{f(i,j)} \\ &+ \left(\frac{i_{(i,j)}}{2F} \left(- c_{p_{H_2}(i,j)} + c_{p_{H_2O}(i,j)} + c_{p_{CO_2}(i,j)} \right) \right)^k T^k_{c(i,j)} + h_f a_{cf} T^k_{c(i,j)} + h_f a_{sf} T^k_{s(i,j)} \end{aligned} \tag{4.21}$$

For the gas in the cathode flow channel,

$$\begin{aligned} &\left(\left(\frac{\sum \left(n \cdot c_p \right)_o}{\Delta y} \right) + \frac{h_o a_{co}}{2} + \frac{h_o a_{so}}{2} \right)^k_{(i,j+1)} T^k_{o(i,j+1)} = \\ &\left(\left(\frac{\sum \left(n \cdot c_p \right)_o}{\Delta y} \right) - \frac{h_o a_{co}}{2} - \frac{h_o a_{so}}{2} \right)^k_{(i,j)} T^k_{o(i,j)} \\ &- \left(\frac{i_{(i,j)}}{4F} \left(c_{p_{O_2}(i,j)} + 2 c_{p_{CO_2}(i,j)} \right) \right)^k T^k_{c(i,j)} + h_f a_{cf} T^k_{c(i,j)} + h_f a_{sf} T^{k-1}_{s(i,j)} \end{aligned} \tag{4.22}$$

For cell,

$$\left(\frac{2(k\delta)_c}{\Delta x^2}+\frac{2(k\delta)_c}{\Delta y^2}+h_f a_{cf}+h_o a_{co}\right)^k T^k_{c(i,j)}=\left(\frac{(k\delta)_c}{\Delta y^2}\right)^k T^k_{c(i,j+1)}$$
$$+\left(\frac{(k\delta)_c}{\Delta y^2}\right)^k T^k_{c(i,j-1)}+\left(\frac{(k\delta)_c}{\Delta x^2}\right)^k T^k_{c(i+1,j)}+\left(\frac{(k\delta)_c}{\Delta x^2}\right)^k T^k_{c(i-1,j)} \quad (4.23)$$
$$+\left(\frac{h_f a_{cf}}{2}\left(T_{f(i+1,j)}+T_{f(i,j)}\right)\right)^k+\left(\frac{h_o a_{co}}{2}\left(T_{o(i+1,j)}+T_{o(i,j)}\right)\right)^k-q^k$$

For separator,

$$\left(\frac{2(k\delta)_s}{\Delta x^2}+\frac{2(k\delta)_s}{\Delta y^2}+h_f a_{sf}+h_o a_{co}\right)^k T^k_{s(i,j)}=\left(\frac{(k\delta)_s}{\Delta y^2}\right)^k T^k_{s(i,j+1)}$$
$$+\left(\frac{(k\delta)_s}{\Delta y^2}\right)^k T^k_{s(i,j-1)}+\left(\frac{(k\delta)_s}{\Delta x^2}\right)^k T^k_{s(i+1,j)}+\left(\frac{(k\delta)_s}{\Delta x^2}\right)^k T^k_{s(i-1,j)} \quad (4.24)$$
$$+\left(\frac{h_f a_{sf}}{2}\left(T_{f(i+1,j)}+T_{f(i,j)}\right)\right)^k+\left(\frac{h_o a_{so}}{2}\left(T_{o(i+1,j)}+T_{o(i,j)}\right)\right)^{k+1}$$

The calculation proceeds as follows

37. The program guesses a uniform current density distribution and solves the molar flow rate of each species in the anode and cathode gas using Equations (4.16) and (4.20).

38. The program solves temperature fields of the anode gas, the cathode gas, the cell, and the separator using Equations (4.21) to (4.24), respectively.

39. The Nernst voltage and internal total resistance are calculated using Equations (4.11) and(4.14), and cell voltage is obtained from Equation (4.15) by setting a constant current. Then, the current density can be got

from Equation(4.13).

40. The current density is updated to Step 1, and iterates the loop from Step 1 to Step 3 until all relative errors of molar flow rates, temperature, and current density satisfy the converge criterion.

41. Step 1 to Step 4 are repeated for calculating the next layer k+1 up to the top layer and then calculating back to the bottom layer.

42. Separator temperature relative errors are checked in all layers between the adjacent calculating loops in Step 5, and the whole calculation stops when relative error satisfies the convergence criteria.

In Chapter 2, validates the numerical method for calculating an MCFC unit and Step 1 to Step 4 for calculating temperature and current density field is reliable. Table 4-2 lists all parameters and conditions in this study. Meanwhile, effective contact thickness between the cell and separator is average cell and separator thickness. Furthermore, this study uses $Nu = 3.15$ to estimate the convection heat transfer coefficient because anode and cathode gas flows are fully developed and laminar.

4.5. Results and Discussion

This study considers four inlet flow patterns, including uniform anode and cathode gas (Pattern I), uniform anode and non-uniform cathode gas (Pattern II),

non-uniform anode and uniform cathode gas (Pattern III), and both non-uniform anode and cathode gas (Pattern IV), shown in Figure 4-2. Non-uniform deviation is 0.5 for all cases, and all non-uniform profiles in the stacking direction progressively increase as calculated by Equations (4.9) and(4.10). Figure 4-3 depicts cell temperature distribution on the bottom, middle, and top layer in different patterns. Each layer in Figure 4-3(a) has a similar temperature contour outline, which increases along the y direction cathode gas flow. Meanwhile, temperature on the top layer is slightly higher than on the bottom layer, because the anode gas flows next to the top end plate, and the cathode gas flows next to the bottom end plate. The end plate is adiabatic with the surrounding as well as the molar flow rate of anode gas is smaller than that of cathode gas. Therefore, the top cell has less cooling due to the anode gas flow between the top cell and the top end plate. The bottom cell has more cooling due to the cathode gas flow between the bottom cell and the bottom end plate. The boundary effect on cell temperature can be neglected because temperature difference between the top and bottom layer is below $10\,°C$. Figure 4-3(b) shows cell temperature distribution on the top, middle, and bottom layer in a ten-layer MCFC with a Pattern II inlet flow configuration. Temperature difference in the same position of different layers in this figure is clearly varied, over $30\,°C$. A cathode gas not only supports oxygen reaction, but also cools the cell because of its flow rate larger than the anode gas. Cathode gas molar flow rate in Pattern II increases with an increase in the stacking direction, so top layer cell temperature is lowest because

most cathode gas flow rate is in this stack. Oppositely, the bottom layer cell has highest temperature due to lacking cathode gas in this layer. Figure 4-3(c) shows cell temperature distribution on the top, middle, and bottom layer in a ten-layer MCFC when the inlet flow configuration is Pattern III, or a non-uniform inlet anode gas. Anode gas on the top layer has more molar flow rate than the other layers, but cell temperature is highest in the ten-layer MCFC stack. Anode gas in the fuel cell provides reactant hydrogen and its flow rate is always restricted for promoting higher fuel utilization. Therefore, anode gas slightly affects the temperature field. Highest temperature on the top layer results from more reaction heat generation, induced by larger molar flow rate of anode gas. The cooling role in this situation is weaker than the anode gas-heating role when the molar flow rate of anode gas increases. Figure 4-3(d) depicts Pattern IV cell temperature in different layers, with both non-uniform inlet anode and cathode gas. Cell temperature distributions in this figure are similar to those in Figure 4-3(b), with only non-uniform inlet cathode gas. Increasing heat generation and cooling ability effect of anode gas with more molar flow rate are both nearly equivalent, therefore non-uniform anode gas slightly induces higher cell temperature on the top layer and lower cell temperature on the bottom layer, compared to those in Figure 4-3(b). Non-uniform molar flow rate of cathode gas consequently dominates the temperature field change in an MCFC stack. Highest cell temperature occurs at the cathode gas exit on the bottom layer, which has the lowest molar flow rate.

Figure 4-4 shows the cell temperature isotherm on the top layer and exit face of anode and cathode gas. Cell temperature in Figure 4-4(a) increases in the cathode gas flow direction, attaining highest temperature at the top middle part of the exit face. Temperature difference between the top middle and bottom middle exit face of cathode gas is close to 10 $°C$ because of end plate boundary effect mentioned in Figure 4-3(a). Figure 4-4(b) depicts the cell temperature isotherm on the top layer and exit face of anode and cathode gas. Cathode gas molar flow rate in the stacking direction progressively increases in Pattern II. Considerable change results in the cell temperature isotherm on exit faces compared to those in Figure 4-4(a) due to higher molar flow rate near the top layers. The non-uniform cathode gas changes the hot spot from the top middle to the bottom middle on the cathode gas exit face. Figure 4-3 illustrates a smaller non-uniform anode gas effect on temperature distribution than that of non-uniform cathode gas, so the isotherm in Figure 4-4(a) and the isotherm in Figure 4-4(c) are similar. The non-uniform anode gas moves the isotherm near the top half layers toward the exit corner because of more anode gas molar flow rate in these layers. Pattern IV isotherms in Figure 4-4(d) are similar to those in Figure 4-4(b) because of the same non-uniform cathode gas inlet flow in the stacking direction. Non-uniform anode gas effect on temperature distribution is observable as indicated by Figure 4-4(d) to 4-4(b) comparison.

Figure 4-5 depicts average cell temperature in different layers with I, II, III, and IV flow- patterns. Temperature profile along the cell number in Pattern I is the most

uniform as expected, because Pattern I has uniform inlet anode and cathode gas. Temperature profile in Pattern II is the most non-uniform due to non-uniform inlet cathode gas, and variation of average cell temperature is close to 2%. Pattern IV has more uniform average cell temperature along the stacking direction than Pattern II, although Pattern IV has both non-uniform anode and cathode gas. Non-uniform inlet anode gas profile induces less molar flow rate in the bottom layer, dropping current density, while simultaneously decreasing chemical reaction heat. Average cell temperature in the Pattern IV bottom layer is therefore lower than that in Pattern II. Pattern III slightly changes average cell temperature in each layer compared to Pattern I, showing non-uniform anode gas effect on cell temperature, as illustrated in Figure 4-3(c).

Figure 4-6 depicts cell voltage of each layer in Pattern I, II, III, and IV flow configuration. Meanwhile, the continuous, dashed, dash-dotted, and dash-double-dotted lines represent the cell voltage distribution in Pattern I, II, III, and IV, respectively. In this figure, continuous and dashed lines are close to straight lines, and their cell voltages in each layer are near 0.8V. The Pattern II is different to the Pattern I in the inlet flow of cathode gas, but their cell voltage distributions in the stacking direction are similar. Therefore, the effect of non-uniform inlet flow of cathode gas on cell voltage distribution can be neglected. Oppositely, the cell voltage distributions in the Pattern III and Pattern IV show severe changes in Fig. 4-6. The dash-dotted and dash-double-dotted lines increase from 0.6V on the bottom layer

to over 0.9V on the top layer. Pattern III and Pattern IV have same non-uniform inlet flow of anode gas in the stacking direction, and their cell voltage distributions are similar to each other. Consequently, the non-uniform inlet flow of anode gas dominates the cell voltage of each layer. When the molar flow rate of anode gas increase, the fuel concentration will slowly drops along its flowing direction, and keep a higher electrical performance. Therefore, the cell voltage will increase in an increase of the molar flow rate. In Figure 4-6, the variation of the cell voltage in Pattern III and IV are over 40%, hence the non-uniform inlet flow effect of anode gas in the stacking direction on electrical performance is very apparent.

4.6. Concluding Remark

This study used a quasi-three dimensional numerical method to analyze the temperature and cell voltage distribution in a ten-layer MCFC with cross-flow configuration. This method is developed from the authors' previous research for analyzing MCFC unit performance. This work investigated four patterns with different arrangements of uniform and non-uniform profiles to study the progressively increasing profile of inlet flow along the stacking direction. The study is used a three-dimensional temperature and current density analysis, and concludes that cathode gas non-uniform molar flow rate dominates temperature field change of an MCFC stack, and that highest cell temperature occurs at the cathode gas exit in the layer with lowest molar flow rate. Non-uniform anode gas in the stacking direction

also strongly affects cell voltage distribution in the MCFC stack. Lower molar flow rate of anode gas induces lower cell voltage because of the concentration drop. Higher molar flow rate maintains higher electrical performance because of smoother fuel concentration along its flowing direction. Furthermore, the variation rate of average cell temperature and cell voltage is close to 2% and 40%, respectively. This non-uniform effect in the stacking direction is apparently larger than that in the transverse direction in Chapter 2.

Table 4.1 Expressions of energy source terms in energy conservation equations (4.5) to (4.8)

Symbols	Description	Expression
$\dot{q}_{conv,s-ag}$	Heat transfer rate from separator to anode gas by convection	$(ha)_{s-ag}\left(T_s - T_{ag}\right)$
$\dot{q}_{conv,s-cg}$	Heat transfer rate from separator to cathode gas by convection	$(ha)_{s-cg}\left(T_s - T_{cg}\right)$
$\dot{q}_{conv,c-ag}$	Heat transfer rate from cell to anode gas by convection	$(ha)_{c-ag}\left(T_c - T_{ag}\right)$
$\dot{q}_{conv,c-cg}$	Heat transfer rate from cell to cathode gas by convection	$(ha)_{c-cg}\left(T_c - T_{cg}\right)$
$\dot{q}_{mass,c-ag}$	Heat transfer rate due to ion immigration from cell to anode gas	$\frac{i}{2F} c_{p,CO_3^{2-}} T_c$
$\dot{q}_{mass,cg-c}$	Heat transfer rate due to ion immigration from cathode gas to cell	$\frac{i}{2F} c_{p,CO_3^{2-}} T_{cg}$
$\dot{q}_{cont}$	Heat transfer rate from cell to separator by contact conduction	$(ka)_{c-s} \frac{(T_c - T_s)}{\delta_{c-s}}$
$\dot{q}_{reac}$ [49]	Heat generation rate due to chemical reaction	$-\Delta H \times \frac{i}{2F} - V \cdot i$ $\Delta H = -240506 - 7.3835 T_c$

Table 4.2 Parameters and conditions in Chapter 4

Mole flow rate and molar fraction of species in anode inlet	
N_{ag}	0.02007 mol/s
X_{H_2}	0.203
X_{CO_2}	0.064
X_{H_2O}	0.15
X_{N_2}	0.583
Mole flow rate and molar fraction of species in cathode inlet	
N_{cg}	0.06136 mol/s
X_{O_2}	0.167
X_{N_2}	0.698
X_{CO_2}	0.135
Inlet temperature	
T_{ag}	858 K
T_{cg}	867 K
Operation Pressure	
P	3.5×10^5 Pa
Conductivity	
k_c	9 W $m^{-1}K^{-1}$
k_s	25 W $m^{-1}K^{-1}$
k_{c-s}	1.0 W $m^{-1}K^{-1}$
Thickness	
δ_c	0.0023 m
δ_s	0.002 m
δ_{c-s}	0.00215 m

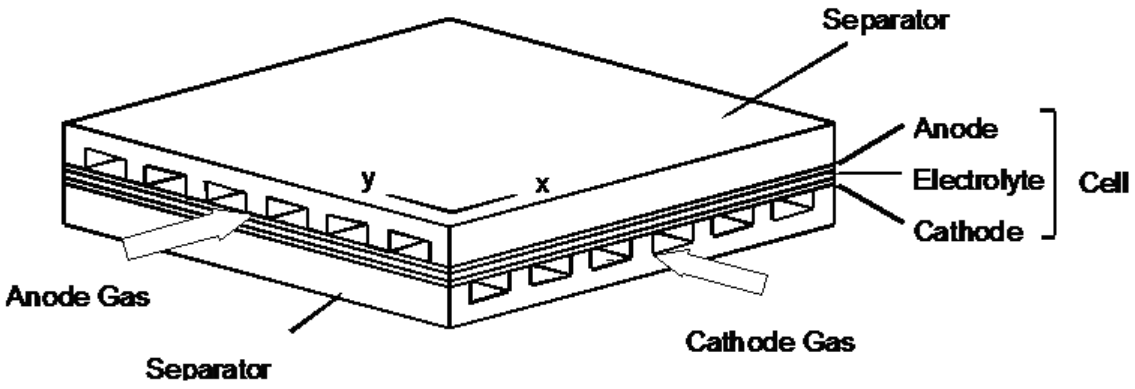

Fig 4.1. Schematic diagram of a molten carbonate fuel cell unit in crossflow.

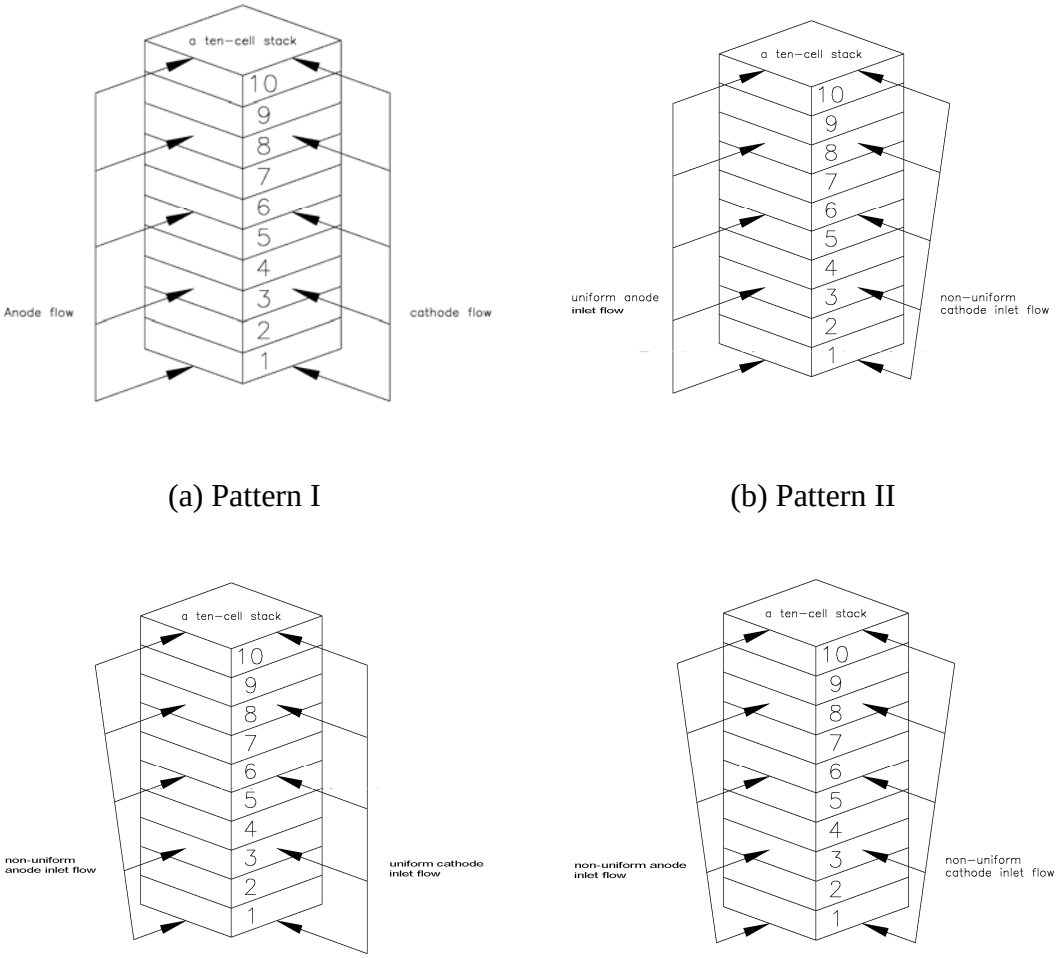

(a) Pattern I

(b) Pattern II

(c) Pattern III

(d) Pattern IV

Fig 4.2. Various inlet flow patterns in an MCFC stack.

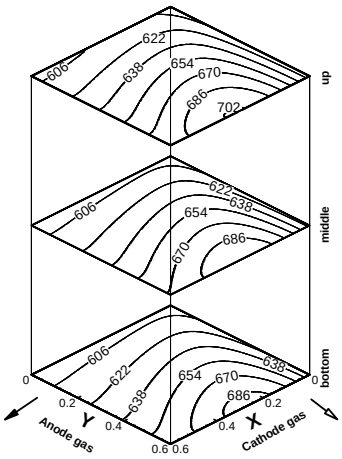

(a) Pattern I

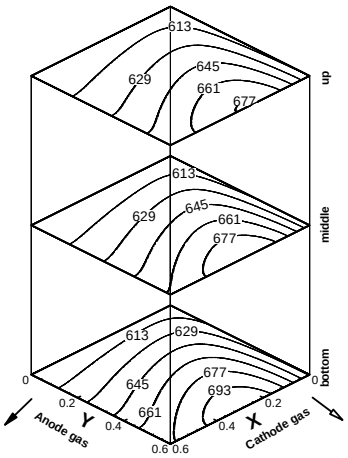

(b) Pattern II

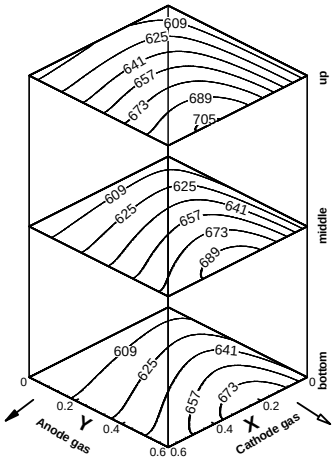

(c) Pattern III

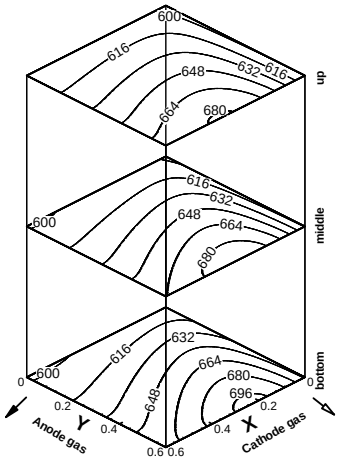

(d) Pattern IV

Fig 4.3. Temperature distribution in bottom, middle, and top layers of an MCFC stack.

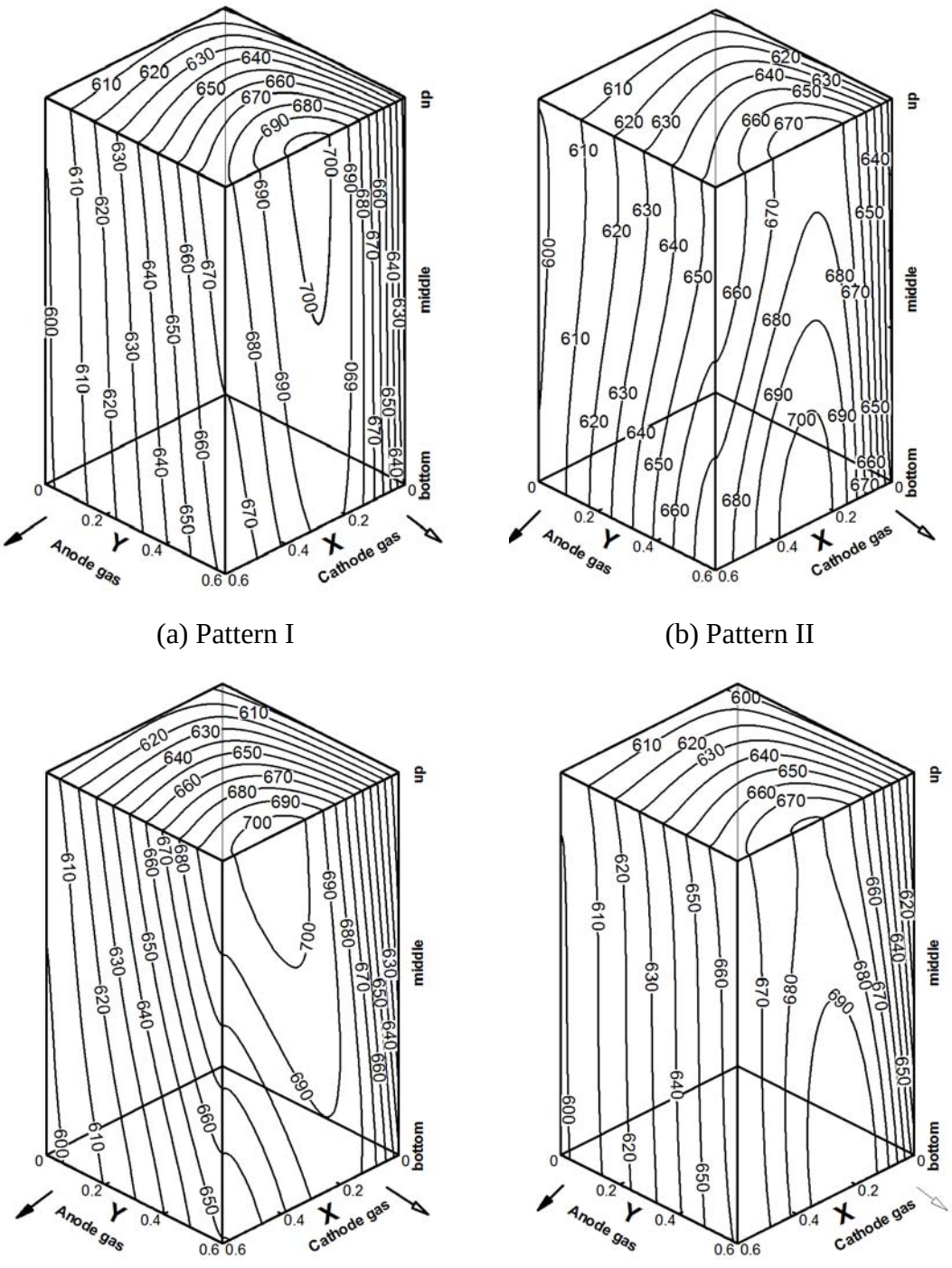

(a) Pattern I

(b) Pattern II

(c) Pattern III

(d) Pattern IV

Fig 4.4. Temperature distribution on exit face and top face of an MCFC stack.

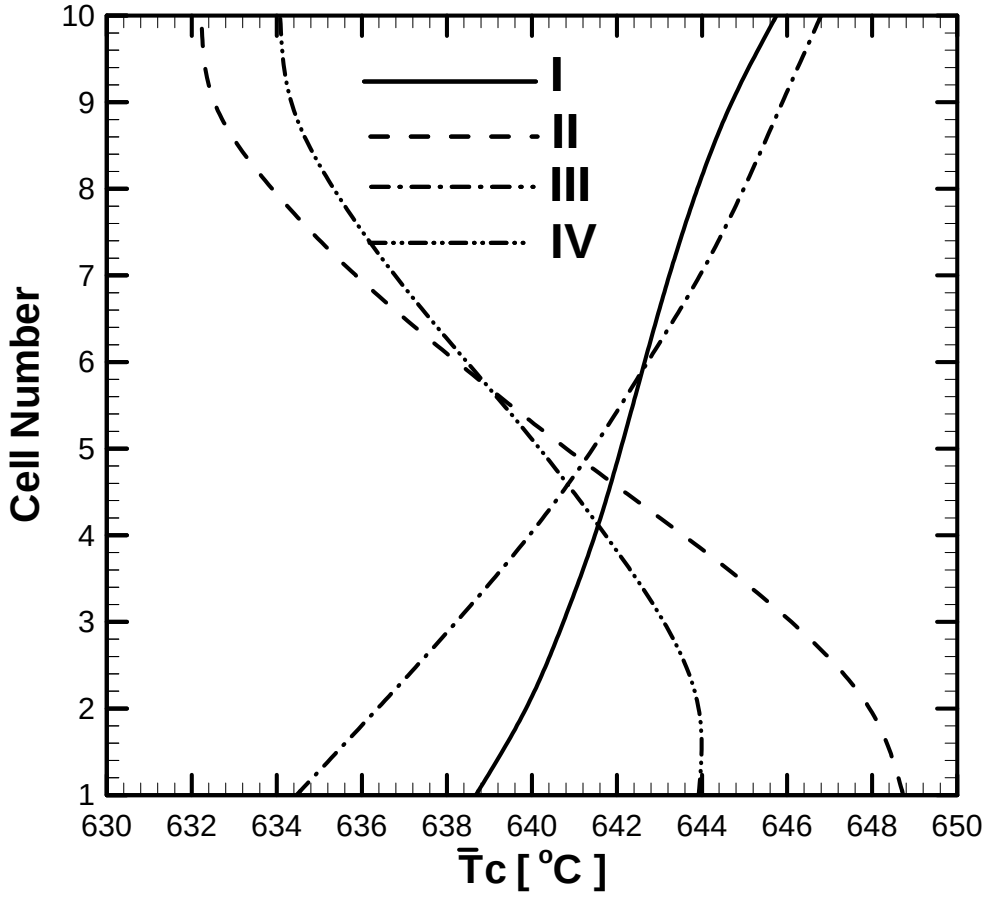

Fig 4.5. Average temperature of each layer in an MCFC stack .

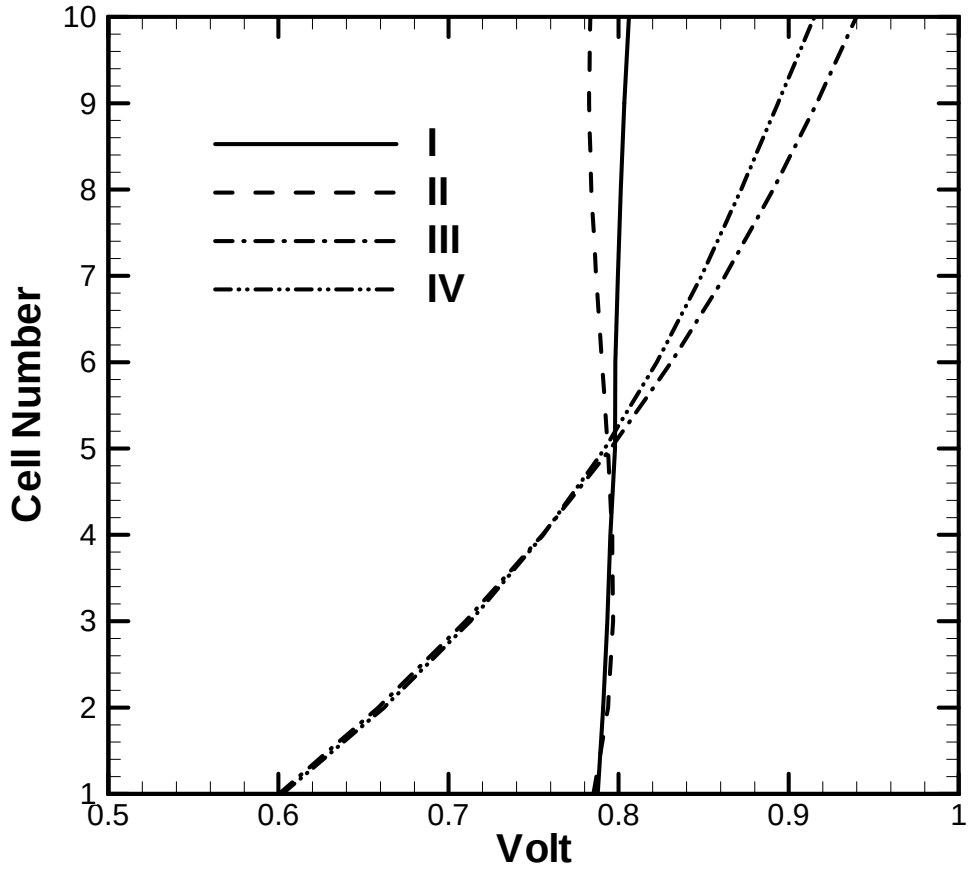

Fig 4.6. Cell voltage of each layer in an MCFC stack.

5. Conclusions and Future Perspectives

5.1. Concluding Remarks

In this dissertation, a two-dimensional model, considering the conservation equations of mass, energy and electro-chemistry is developed to investigate the thermal and electrical performances of a MCFC subjected to various conditions of inlet flow maldistribution. The discussions include a unit cell with eight different patterns of inlet flows as well as a cell stack with non-uniform inlet flow rate in stacking direction. Scenario of a unit MCFC operating at a high gas utilization is also investigated in detail.

For a unit of MCFC, the non-uniform inlet flow rate of cathode gas dominates the cell temperature distribution, which can be observed in other fuel cells with intermediate-high operating temperature. The cathode gas plays the role for cooling the cell plane to avoid the happening of hot spots, which will induce the corrosion of the electrolyte. On the other hand, the non-uniform inlet flow rate of anode gas strongly affects the current density distribution, and slightly affects the cell temperature distribution.

For a stack of MCFC, non-uniform anode gas in the stacking direction also strongly affects cell voltage distribution in the MCFC stack. Lower molar flow rate of anode gas induces lower cell voltage because of the concentration drop. Higher molar flow rate maintains higher electrical performance because of smoother fuel

concentration along its flowing direction. Furthermore, the variation rate of average cell temperature and cell voltage is close to 2% and 40%, respectively. This non-uniform effect in the stacking direction is apparently larger than that in the transverse direction in a unit of MCFC.

The calculation results of the high gas utilization in a MCFC unit show that the anode gas utilization increases with a decrease in the molar flow rate, and the average current density decreases when the molar flow rate drops. In addition, non-uniform inlet profile of the anode gas will induce a happening of non-reaction area in the corner of the anode gas exit and the cathode gas inlet. This non-reaction area deteriorates the average current density and then reduces the electrical performance up to 8%..

5.2. Future Perspectives

With the knowledge and findings obtained from the preceding investigations, there are several possible research directions which are worthy of further exploration in the future. At first, the temperature and current density distributions on the x-z plane and y-z plane are required to be quested for discussing the details of the effects of non-uniform inlet flow in the stacking direction on the stack performance. Moreover, it is necessary to extend the analysis with various utilizations of anode gas and cathode gas in order to investigate the area of non-reaction on the cell plane in a unit of MCFC and a stack of MCFC. According to the results of non-reaction area,

this study can optimize the non-uniform profile of inlet flow in anode gas and cathode gas. Furthermore, the extension of the steady analysis to the transient analysis of a unit of MCFC for providing some information in a real time control system is another crucial topics of research.

References

1. Divisek, J., *Handbook of fuel cells : fundamentals, technology, and applications*. Fundamentals and Survey of Systems, ed. W. Vielstich, A. Lamm, and H.A. Gasteiger. Vol. 1. 2003, Chichester, England ; Hoboken, N.J.: Wiley. 115-133.

2. Oshima, R., Ohtsuka, K., Kahara, T., Kurita, K.t., Takeuchi, M., and Kobayashi, N., *Development of molten carbonate fuel cell.* Nippon Kikai Gakkai Ronbunshu, B Hen/Transactions of the Japan Society of Mechanical Engineers, Part B, 1988. **54**(507): p. 3259-3264.

3. Li, X., *Principles of fuel cells*. 2006, New York: Taylor & Francis. 431-476.

4. Bergman, B., Lagergren, C., Lindbergh, G., Schwartz, S., and Zhu, B.H., *Contact corrosion resistance between the cathode and current collector plate in the molten carbonate fuel cell.* Journal of the Electrochemical Society, 2001. **148**(1): p. A38-A43.

5. Kimijima, S. and Kasagi, N., *Cycle analysis of micro gas turbine-molten carbonate fuel cell hybrid system.* Nippon Kikai Gakkai Ronbunshu, B Hen/Transactions of the Japan Society of Mechanical Engineers, Part B, 2003. **69**(680): p. 1001-1008.

6. Wilemski, G. and Wolf, T.L. *Role of heat transfer in molten carbonate fuel cell*

performance. 1986. San Diego, CA, USA: Electrochemical Soc, Pennington, NJ, USA.

7. Kobayashi, N., Fujimura, H., and Ohtsuka, K., *Heat and mass transfer in a molten carbonate fuel cell. (Experimental and analytical investigation of fuel cell temperature distribution).* JSME International Journal, Series 2: Fluids Engineering, Heat Transfer, Power, Combustion, Thermophysical Properties, 1989. **32**(3): p. 420-427.

8. Lee, Y.R., Yoo, M.J., Chung, G.Y., Lim, H.C., Lim, T.H., Nam, S.W., and Hong, S.A., *Studies on the modeling calculations of the unit molten carbonate fuel cell.* Korean Journal of Chemical Engineering, 2005. **22**(2): p. 219-227.

9. Yoshiba, F., Ono, N., Izaki, Y., Watanabe, T., and Abe, T., *Numerical analyses of the internal conditions of a molten carbonate fuel cell stack: comparison of stack performances for various gas flow types.* Journal of Power Sources, 1998. **71**(1-2): p. 328-336.

10. Yoshiba, F., Abe, T., and Watanabe, T., *Numerical analysis of molten carbonate fuel cell stack performance: diagnosis of internal conditions using cell voltage profiles.* Journal of Power Sources, 2000. **87**(1-2): p. 21-27.

11. He, W. and Chen, Q., *3-Dimensional Simulation of a Molten-Carbonate Fuel-Cell Stack Using Computational Fluid-Dynamics Technique.* Journal of

Power Sources, 1995. **55**(1): p. 25-32.

12. Ma, Z., Blanchet, S., Venkataraman, R., Iaccarino, G., and Moin, P., *Mathematical modeling of an internal-reforming, carbonate fuel cell stack*, in *The 2nd International Conference on FUEL CELL SCIENCE, ENGINEERING and TECHNOLOGY*. 2004: Rochester, NY.

13. Mugikura, Y., *Handbook of fuel cells : fundamentals, technology, and applications*. Fuel Cell Technology and Applications: Part 2, ed. W. Vielstich, A. Lamm, and H.A. Gasteiger. Vol. 4. 2003, Chichester, England ; Hoboken, N.J.: Wiley. 907-920.

14. Lukas, M.D., Lee, K.Y., and Ghezel-Ayagh, H., *Development of a stack simulation model for control study on direct reforming molten carbonate fuel cell power plant.* Ieee Transactions on Energy Conversion, 1999. **14**(4): p. 1651-1657.

15. Koh, J.H., Kang, B.S., and Lim, H.C., *Analysis of temperature and pressure fields in molten carbonate fuel cell stacks.* Aiche Journal, 2001. **47**(9): p. 1941-1956.

16. Koh, J.-H., Seo, H.-K., Yoo, Y.-S., and Lim, H.C., *Consideration of numerical simulation parameters and heat transfer models for a molten carbonate fuel cell stack.* Chemical Engineering Journal, 2002. **87**(3): p. 367-379.

17. He, W. and Chen, Q., *Three-dimensional simulation of a molten carbonate fuel cell stack under transient conditions.* Journal of Power Sources, 1998. **73**(2): p. 182-192.

18. Xu, X.Z., Tanimoto, K., and Kimihiko, S., *Analysis of transient voltage response on a 4 x 4 cm molten carbonate fuel cell by a current pulse method.* Journal of the Electrochemical Society, 2002. **149**(8): p. A1025-A1029.

19. Heidebrecht, P. and Sundmacher, K., *Molten carbonate fuel cell (MCFC) with internal reforming: model-based analysis of cell dynamics.* Chemical Engineering Science, 2003. **58**(3-6): p. 1029-1036.

20. Lee, Y.R., Kim, I.G., Chung, G.Y., Lee, C.G., Lim, H.C., Lim, T.H., Nam, S.W., and Hong, S.A., *Studies on the initial behaviours of the molten carbonate fuel cell.* Journal of Power Sources, 2004. **137**(1): p. 9-16.

21. Vallet, C.E. and Braunstein, J., *Steady-State Composition Profiles in Mixed Molten-Salt Electrochemical Devices .2. Molten Carbonate Fuel-Cell Analogs.* Journal of the Electrochemical Society, 1979. **126**(4): p. 527-534.

22. Wilemski, G., *Simple Porous-Electrode Models for Molten Carbonate Fuel-Cells.* Journal of the Electrochemical Society, 1983. **130**(1): p. 117-121.

23. Kunz, H.R., Bregoli, L.J., and Szymanski, S.T., *A Homogeneous Agglomerate Model for Molten Carbonate Fuel-Cell Cathodes.* Journal of the

Electrochemical Society, 1984. **131**(12): p. 2815-2821.

24. Lee, C.G., Nakano, H., Nishina, T., Uchida, I., Izaki, Y., and Kuroe, S., *Transient response analysis on an 100cm(2) class molten carbonate fuel cell.* Denki Kagaku, 1996. **64**(6): p. 486-490.

25. PrinsJansen, J.A., Hemmes, K., and deWit, J.H.W., *An extensive treatment of the agglomerate model for porous electrodes in molten carbonate fuel cells .1. Qualitative analysis of the steady-state model.* Electrochimica Acta, 1997. **42**(23-24): p. 3585-3600.

26. PrinsJansen, J.A., Hemmes, K., and deWit, J.H.W., *An extensive treatment of the agglomerate model for porous electrodes in molten carbonate fuel cells .2. Quantitative analysis of time-dependent and steady-state model.* Electrochimica Acta, 1997. **42**(23-24): p. 3601-3618.

27. Fehribach, J.D., Prins-Jansen, J.A., Hemmes, K., De Wit, J.H.W., and Call, F.W., *On modelling molten carbonate fuel-cell cathodes by electrochemical potentials.* Journal of Applied Electrochemistry, 2000. **30**(9): p. 1015-1021.

28. Morita, H., Komoda, M., Mugikura, Y., Izaki, Y., Watanabe, T., Masuda, Y., and Matsuyama, T., *Performance analysis of molten carbonate fuel cell using a Li/Na electrolyte.* Journal of Power Sources, 2002. **112**(2): p. 509-518.

29. Arato, E., Bosio, B., Coste, P., and Parodi, F., *Preliminary experimental and*

theoretical analysis of limit performance of molten carbonate fuel cells. Journal of Power Sources, 2001. **102**(1-2): p. 74-81.

30. Bosio, B., Costamagna, P., and Parodi, F., *Modeling and experimentation of molten carbonate fuel cell reactors in a scale-up process.* Chemical Engineering Science, 1999. **54**(13-14): p. 2907-2916.

31. Mangold, M. and Sheng, M., *Nonlinear model reduction of a two-dimensional MCFC model with internal reforming.* Fuel Cells, 2004. **4**(1-2): p. 68-77.

32. He, W., *Dynamic model for molten carbonate fuel-cell power-generation systems.* Energy Conversion and Management, 1998. **39**(8): p. 775-783.

33. He, W., *An investigation on the dynamic performance of molten carbonate fuel-cell power-generation systems.* International Journal of Energy Research, 1998. **22**(4): p. 355-362.

34. De Simon, G., Parodi, F., Fermeglia, M., and Taccani, R., *Simulation of process for electrical energy production based on molten carbonate fuel cells.* Journal of Power Sources, 2003. **115**(2): p. 210-218.

35. Yoshiba, F., Izaki, Y., and Watanabe, T., *System calculation of integrated coal gasification/molten carbonate fuel cell combined cycle: Reflection of electricity generating performances of practical cell.* Journal of Power Sources, 2004. **132**(1-2): p. 52-58.

36. Baranak, M., Atakul, H., Sener, T., Akgun, F., and Tiris, M., *A model for molten carbonate fuel cells*, in *International Hydrogen Energy Congress and Exhibition IHEC 2005*. 2005: Istanbul, Turkey.

37. Park, N.K., Lee, Y.R., Kim, M.H., Chung, G.Y., Nam, S.W., Hong, S.A., Lim, T.H., and Lim, H.C., *Studies of the effects of the reformer in an internal-reforming molten carbonate fuel cell by mathematical modeling.* Journal of Power Sources, 2002. **104**(1): p. 140-147.

38. Seo, H.-K., Eom, Y.-C., Kim, Y.-C., Lee, S.-D., and Gu, J.-H., *Operation results of a 100 kW class reformer for molten carbonate fuel cell.* Journal of Power Sources, 2007. **166**(1): p. 165-171.

39. Kim, M.-H., Park, H.-K., Chung, G.-Y., Lim, H.-C., Nam, S.-W., Lim, T.-H., and Hong, S.-A., *Effects of water-gas shift reaction on simulated performance of a molten carbonate fuel cell.* Journal of Power Sources, 2002. **103**(2): p. 245-252.

40. Bosio, B., Costamagna, P., Parodi, F., and Passalacqua, B., *Industrial experience on the development of the molten carbonate fuel cell technology.* Journal of Power Sources, 1998. **74**(2): p. 175-187.

41. Chiou, J.P., *Thermal Performance Deterioration in Cross-Flow Heat-Exchanger Due to Flow Nonuniformity.* Journal of Heat

Transfer-Transactions of the Asme, 1978. **100**(4): p. 580-587.

42. Yuan, P. and Kou, H.S., *Entropy generation on a crossflow heat exchanger including three gas streams with different arrangements and the effect of longitudinal wall conduction.* Numerical Heat Transfer Part a-Applications, 2003. **43**(6): p. 619-638.

43. Yuan, P., *Exergy analysis on a three-gas crossflow heat exchanger with nonuniform inlet flow.* International Journal of Heat Exchangers, 2005. **6**(1): p. 55-72.

44. Hirata, H. and Hori, M., *Gas-flow uniformity and cell performance in a molten carbonate fuel cell stack.* Journal of Power Sources, 1996. **63**(1): p. 115-120.

45. Hirata, H., Nakagaki, T., and Hori, M., *Effect of gas channel height on gas flow and gas diffusion in a molten carbonate fuel cell stack.* Journal of Power Sources, 1999. **83**(1-2): p. 41-49.

46. Okada, T., Matsumoto, S., Matsumura, M., Miyazaki, M., and Umeda, M., *Gas distribution in molten-carbonate fuel cells.* Journal of Power Sources, 2006. **162**(2): p. 1029-1035.

47. Patankar, S.V., *Numerical heat transfer and fluid flow*. 1980, New York: Hemisphere Publ. Corp. xiii, 197.

48. Rohsenow, W.M., Cho, Y.I., and Hartnett, J.P., *Handbook of heat transfer*. 3rd ed. 1998, New York: McGraw-Hill. 1 v. (various pagings).

49. Blomen, L.J.M.J. and Mugerwa, M.N., *Fuel cell systems*. 1993, New York: Plenum Press. xix, 614.

Appendix A

```
TITLE 'Single    MCFC Fuel Cell'
SELECT
ERRLIM=0.001
ngrid= on
Regrid=on
VARIABLES
   Tga Tgc Ts Te
   Gh2f Gh2of Gco2f Gco2ox Go2ox
 DEFINITIONS
   F=96485    R=8314.4
   Landas=22    Landae=16.2        Landase=1.0
   Lx=0.6             Ly=0.6
   AAs=1.0             AAe=1.0              AAse=0.47 AAeg=0.53         AAsg=1.26
   tte=0.00035       tts=0.001    ttse=0.001075

Gf0=0.0621/Ly                    Gox0=0.1841/Lx
  Xh2f0=0.203      Xco2f0=0.064    Xh2of0=0.150      Xn2f0=0.583
     Xo2ox0=0.167
     Xn2ox0=0.698
     Xco2ox0=0.135
   E0=1.040      P=3.5E5
  Kshift=157.02-0.4447*Tga+4.2777E-4*Tga^2-1.3871E-7*Tga^3

     Xh2f=Gh2f/(Gh2f+Gco2f+Gh2of+Gcof+Gn2f)
Xco2f=Gco2f/(Gh2f+Gco2f+Gh2of+Gcof +Gn2f )
   Xh2of=Gh2of/(Gh2f+Gco2f+Gh2of+Gcof+Gn2f)
Xcof=Gcof/(Gh2f+Gco2f+Gh2of+Gcof+Gn2f    )
     Xn2f=Gn2f/(Gh2f+Gco2f+Gh2of+Gcof+Gn2f)
   Xo2ox=Go2ox/(Go2ox+Gco2ox+Gn2ox)
Xco2ox=Gco2ox/(Go2ox+Gco2ox+Gn2ox)
   Xn2ox=Gn2ox/(Go2ox+Gco2ox+Gn2ox)

   Kega=593.1
   Ksga=593.1
   Kegc=91.1
   Ksgc=91.1

        Cpco2=25.977+4.36E-2*Te+(-1.494E-5)*Te^2
        Cpn2 =27.313+5.190E-3*Te+(-7.212E-10)*Te^2
```

```
      Cph2 =28.949+(-5.855E-4)*Te+(1.890E-6)*Te^2
      Cph2o=30.407+9.54E-3*Te+(1.183E-6)*Te^2
      Cpo2 =25.749+1.294E-2*Te+(-3.853E-6)*Te^2
    Cpco2f=25.977+4.36E-2*Tga+(-1.494E-5)*Tga^2
    Cpn2f =27.313+5.190E-3*Tga+(-7.212E-10)*Tga^2
    Cph2f =28.949+(-5.855E-4)*Tga+(1.890E-6)*Tga^2
    Cph2of=30.407+9.54E-3*Tga+(1.183E-6)*Tga^2
    Cpo2f =25.749+1.294E-2*Tga+(-3.853E-6)*Tga^2
   Cpco2ox=25.977+4.36E-2*Tgc+(-1.494E-5)*Tgc^2
   Cpn2ox =27.313+5.190E-3*Tgc+(-7.212E-10)*Tgc^2
   Cph2ox =28.949+(-5.855E-4)*Tgc+(1.890E-6)*Tgc^2
   Cph2oox=30.407+9.54E-3*Tgc+(1.183E-6)*Tgc^2
   Cpo2ox =25.749+1.294E-2*Tgc+(-3.853E-6)*Tgc^2
 E=E0+R*Te/(2*F)*ln(Xo2ox^0.5*Xco2ox*Xh2f/Xh2of/Xco2f*P^0.5)

Reff=1.38E-7*Exp(11400/Te)/(P^0.67*Xo2ox^0.67*Xco2ox*Xh2f/(Xco2f*Xh2of))
                                          +0.348E-4+4.8E-8*Exp(6596/Te)
   i=(E - Voltage)/(Reff)
q=i*((-240506-7.3835*Te)/(2*F)-Voltage)
Qs=0
INITIAL VALUES
  Tga=858 Tgc=867 Ts=800 Te=800
EQUATIONS

Tga: (Gh2f*Cph2f+Gh2of*Cph2of+Gco2f*Cpco2f)*dx(Tga)=
        AAeg*Kega*(Te-Tga)+AAsg*Ksga*(Ts-Tga)+i/(2*F)*Cpco3*Te+Qs
Tgc:(Gco2ox*Cpco2ox+Go2ox*Cpo2ox+Gn2ox*Cpn2ox)*dy(Tgc)=
        AAeg*Kegc*(Te-Tgc)+AAsg*Ksgc*(Ts-Tgc)-i/(2*F)*Cpco3ox*Tgc
Ts:
AAs*Landas*tts*(dxx(Ts)+dyy(Ts))=AAse*Landase/ttse*(Ts-Te)+AAsg*Ksga*(Ts-Tga)
                                    +AAsg*Ksgc*(Ts-Tgc)
Te:
AAe*Landae*tte*(dxx(Te)+dyy(Te))+q=AAse*Landase/ttse*(Te-Ts)+AAeg*Kega*(Te-Tga)

+AAeg*Kegc*(Te-Tgc)+i/(2*F)*Cpco3*Te-i/(2*F)*Cpco3ox*Tgc

  Gh2f: dx(Gh2f)=eps*del2(Gh2f)-i/(2*F)+delta*(Gh2f+Gco2f+Gh2of+Gcof)
  Gh2of: dx(Gh2of)=eps*del2(Gh2of)+i/(2*F)-delta*(Gh2f+Gco2f+Gh2of+Gcof)
  Gco2f: dx(Gco2f)=eps*del2(Gco2f)+i/(2*F)+delta*(Gh2f+Gco2f+Gh2of+Gcof)
  Gcof: dx(Gcof)=eps*del2(Gcof)-delta*(Gh2f+Gco2f+Gh2of+Gcof)
```

```
   Gco2ox: dy(Gco2ox)=eps*del2(Gco2ox)+i/(2*F)
   Go2ox: dy(Go2ox)=eps*del2(Go2ox)-i/(4*F)
BOUNDARIES
REGION 1
START(0,0)
      nobc(Tga) value(Tgc)=867 value(Gco2ox)=Gox0*Xco2ox0
value(Go2ox)=Gox0*Xo2ox0
      natural(Te)=0 natural(Ts)=0
        line to (Lx,0)
      nobc(Tga)    nobc(Tgc)    nobc(Gco2ox) nobc(Go2ox) natural(Te)=0
natural(Ts)=0
   line to (Lx,Ly)
      nobc(Tga)    nobc(Tgc)      nobc(Gco2ox) nobc(Go2ox) natural(Te)=0
natural(Ts)=0
   line to (0,Ly)
      value(Tga)=858    value(Gh2f)=Gf0*Xh2f0    value(Gh2of)=Gf0*Xh2of0
      value(Gco2f)=Gf0*Xco2f0      nobc(Tgc)    natural(Te)=0    natural(Ts)=0

MONITORS
      contour(Tga-273) contour(Tgc-273) contour(Te-273) contour(Ts-273) contour(i)
contour(Gh2f)
      contour(Gh2of) contour(Gco2f) contour(Go2ox) contour(Gco2ox)    contour(E)
contour(Reff)
      elevation(Tga-273) from (0,Ly/2) to (Lx,Ly/2)    elevation(Tgc-273) from
(Lx/2,0) to (Lx/2,Ly)
      summary
        report((integral(E,1))/Lx/Ly) report((integral(Reff,1))/Lx/Ly)    report(Voltage)
        report((integral(i,1))/Lx/Ly)       report((integral(Tga,1))/Lx/Ly-273)
report((integral(Tgc-273,1))/Lx/Ly)
PLOTS
     contour(Tga-273) contour(Tgc-273) contour(Te-273) contour(Ts-273) contour(i)
contour(Gh2f)
      contour(Gh2of) contour(Gco2f) contour(Go2ox) contour(Gco2ox)    contour(E)
contour(Reff)
      elevation(Tga-273) from (0,Ly/2) to (Lx,Ly/2)    elevation(Tgc-273) from
(Lx/2,0) to (Lx/2,Ly)
      summary
        report((integral(E,1))/Lx/Ly) report((integral(Reff,1))/Lx/Ly)    report(Voltage)
        report((integral(i,1))/Lx/Ly)       report((integral(Tga,1))/Lx/Ly-273)
report((integral(Tgc-273,1))/Lx/Ly)
  HISTORIES
END
```

Publication List

Journal Paper

1. Liu, S.-F., Chu, H.-S., and Yuan, P., *Effect of inlet flow maldistribution on the thermal and electrical performance of a molten carbonate fuel cell unit.* Journal of Power Sources, 2006. **161**(2): p. 1030-1040.

2. Liu, S.-F. and Chu, H.-S., *Effects of non-uniform inlet flow on the performance of a molten carbonate fuel cell stack.* Journal of the Chinese Society of Mechanical Engineers, 2007. **28**(3): p. 265-274.

3. Liu, S.-F. and Chu, H.-S., *Current density analysis in a molten carbonate fuel cell unit with non-uniform inlet flow and high anode gas utilization.* Journal of the Chinese Society of Mechanical Engineers, 2007 (In press).

Conference Paper

1. Liu, S.-F., Chu, H.-S., and Yuan, P., *Effect of Inlet Flow Maldistribution in the Stacking Direction on the Thermal and Electrical Performance of a Molten Carbonate Fuel Cell*, in *2006 International Fuel Cell Symposium*. 2006, Yuan Ze Fuel Cell Center: Taiwan, Taoyuan.

Author

姓名　劉旭昉

地址　台北市大安區瑞安街 162 號

學歷

國立交通大學機械系博士班	86/9~
國立成功大學機械所碩士班	74/9~76/6
國立成功大學造船暨船舶機械系學士班	70/9~74/6

Publication List

Journal Paper

1. Liu, S.-F., Chu, H.-S., and Yuan, P., *Effect of inlet flow maldistribution on the thermal and electrical performance of a molten carbonate fuel cell unit.* Journal of Power Sources, 2006. **161**(2): p. 1030-1040.

2. Liu, S.-F. and Chu, H.-S., *Effects of non-uniform inlet flow on the performance of a molten carbonate fuel cell stack.* Journal of the Chinese Society of Mechanical Engineers, 2007. **28**(3): p. 265-274.

3. Liu, S.-F. and Chu, H.-S., *Current density analysis in a molten carbonate fuel cell unit with non-uniform inlet flow and high anode gas utilization.* Journal of the Chinese Society of Mechanical Engineers, 2007 (In press).

Conference Paper

1. Liu, S.-F., Chu, H.-S., and Yuan, P., *Effect of Inlet Flow Maldistribution in the Stacking Direction on the Thermal and Electrical Performance of a Molten Carbonate Fuel Cell*, in *2006 International Fuel Cell Symposium*. 2006, Yuan Ze Fuel Cell Center: Taiwan, Taoyuan.